Inorganica Chimica Acta 519 (2021) 120264

Contents lists available at ScienceDirect

Inorganica Chimica Acta

journal homepage: www.elsevier.com/locate/ica

Research paper

Crystal structure, spectroscopic, DFT calculations and antimicrobial study of the Cu(II) complex bearing second-generation quinolone ofloxacin and 2,2′-bipyridine

Joshua Ayoola Obaleye [a,*], Misitura Lawal [a,b,c], Rajendrasinh N. Jadeja [b,*], Vivek Kumar Gupta [d], Ginikachukwu Grace Nnabuike [a], Mercy Oluwaseyi Bamigboye [e], Hetal Roy [f], Olaniyi Kamil Yusuff [a], Poonam Bhagariya [f]

[a] Department of Chemistry, University of Ilorin, P.M.B 1515, Ilorin, Kwara State, Nigeria
[b] Department of Chemistry, The Maharaja Sayajirao University of Baroda, Vadodara 390002, India
[c] Department of Pure and Applied Chemistry, Kebbi State University of Science and Technology, P.M.B 1144 Aliero, Kebbi State, Nigeria
[d] Department of Physics, University of Jammu, Jammu Tawi 180006, India
[e] Department of Industrial Chemistry, University of Ilorin, P.M.B 1515, Ilorin, Kwara State, Nigeria
[f] Department of Zoology, The Maharaja Sayajirao University of Baroda, Vadodara 390002, India

ARTICLE INFO

Keywords:
Ofloxacin
2, 2′-bipyridine
Thermal analysis
Crystal structure
Antimicrobial activity
DFT

ABSTRACT

Cu(II) complex of second-generation quinolone ofloxacin with 2,2′-bipyridine formulated as [Cu(ofx)(2bpy)(H_2O)].ClO_4·$2H_2O$ (1) [ofx = ofloxacin, 2bpy = 2,2′-bipyridine] has been synthesized. The coordination possibility of the ofx and 2bpy towards metal ion was proposed using single-crystal X-ray diffraction analysis (SCXRD), IR, UV–Visible, EPR, thermal analysis, molar conductance, and elemental analysis. The interaction of Cu(II) with the deprotonated ofloxacin ligand resulted in the formation of the mononuclear complex of the type [Cu(ofx)(2bpy)(H_2O)].ClO_4·$2H_2O$. Single crystal X-ray crystallography data revealed a five-coordinate, distorted square-pyramidal arrangement in the complex. The complex crystallizes in the triclinic system with a = 10.2192 (13), b = 12.7080(19), c = 12.8156(16) Å, and space group P–1. The measurement of the complex molar conductance in DMSO (10^{-3} M solution at 25 °C) revealed the electrolytic nature of the complex and was of the 1:1 type. The presence of coordinated water molecules and the metal oxide in the final product was determined by thermal analysis studies. DFT calculations were carried out for the complex ion and the two ligands using the B3LYP/631-G(d) level of theory and the HOMO-LUMO energy gap was evaluated. The results showed that the complex with the lowest energy gap value (0.951 eV) is more reactive than the ligands. The ligand and its copper (II) complex were screened in order to evaluate the antimicrobial activity by measuring the inhibition zone (mm). The results showed that the metal complex was observed to be more active than the parent ligand.

1. Introduction

The biological and pharmaceutical studies of the coordination chemistry of different metal ions with fluoroquinolone drugs are of great importance and considerable interest. Metal complexes containing *N*-donor ligands e.g. phen, 2bpy (Fig. 1b), and other similar ligands have been intensively investigated because of their numerous biological activities such as antitumor, and antimicrobial [1–3]. Copper (II) complexes with drugs as ligands have very high activity in the presence of a nitrogen donor heterocyclic compounds, such as 2,2′-bipyridine (2bpy), 1,10-phenanthroline (phen), and 2,2′-Dipyridylamine (bipym) [4–7]. The interaction of transition metal ions with various first and second-generation deprotonated quinolones drugs as ligands in the presence or absence of a nitrogen donor heterocyclic ligand has always been of great interest [8].Some of these are Cu(II) complexes of ciprofloxacin [9,10], ofloxacin [11],levofloxacin [12], ciprofloxacin [13], flumequine [14],ofloxacin [15,16], norfloxacin, [17]oxolinic acid [18], and enrofloxacin[19]. One of the main objectives when studying the interactions

Abbreviations: Ofx, ofloxacin; 2bpy, 2, 2′-bipyridine; LMCT, ligand-to-metal charge-transfer; EPR, electron paramagnetic resonance; TG, thermal analysis; Exptal, experimental.

* Corresponding authors.
E-mail addresses: jobaleye@yahoo.com, jobaleye@unilorin.edu.ng (J.A. Obaleye), rjadeja-chem@msubaroda.ac.in (R.N. Jadeja).

https://doi.org/10.1016/j.ica.2021.120264
Received 2 December 2020; Received in revised form 15 January 2021; Accepted 15 January 2021
Available online 2 February 2021
0020-1693/

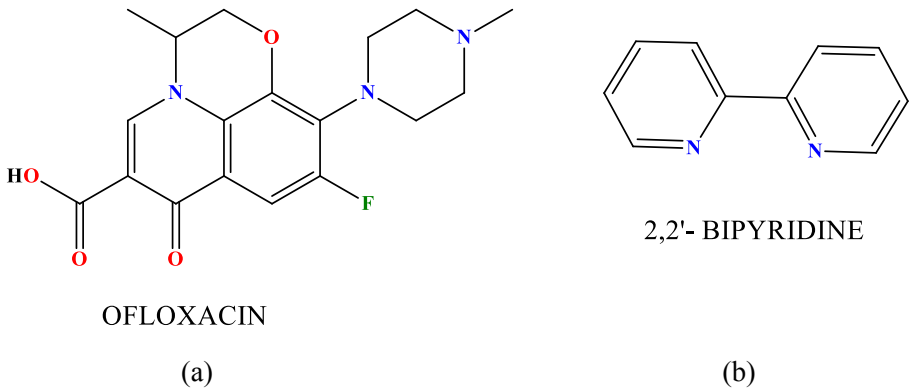

(a) (b)

Fig. 1. Ligands used in the synthesis of the complex (a) ofloxacin (ofx), and (b) 2,2′-bipyridine (2bpy).

between metal cations and antibiotics is to ascertain the nature of the functional groups responsible for the metal to ligand binding.

In general, quinolones can be used as antibacterial drugs that inhibit DNA synthesis effectively and are utilized widely to cure many infections [20,21]. Ofloxacin (Fig. 1a) is a second-generation quinolone antibacterial drug used for the treatment of both Gram-positive and Gram-negative pathogens; significantly, they are also active against *Mycobacterium tuberculosis,* the tuberculosis causative agent [22]. Ofloxacin is also utilized for the treatment of bacterial infections such as those of the sinuses, cellulitis, ears, skin, bones, and many others caused by susceptible bacteria, urinary tract infections, prostatitis [23,24].

As a result of their extensive use, there has been an increasing threat of bacterial resistance to quinolones [25], which led to the need to improve on the existing antimicrobial drugs and or develop new ones having more effective therapeutic values which could be an alternative to conventional drugs, as new derivatives of fluoroquinolones [26,27].

To date, few articles have been reported on the coordination properties and crystal structure of mixed ligand complex of ofloxacin with the hetero ligand like [Cu(ofx)(bipym)(CH_3OH)]ClO_4·2H_2O] [15], and [Cu(oflo)(phen)(H_2O)]NO_3·2H_2O] [16]. This has inspired us to obtain another novel ternary complex with its crystal structure including an evaluation of its biological activity.

In this paper, we have studied the coordination behavior, antimicrobial efficacy, and DFT calculations of novel Cu(II) complex with the second-generation quinolone drug ofloxacin and 2,2′-bipyridine. The structure of the synthesized complex [Cu(ofx)(2bpy)(H_2O)].ClO_4·2H_2O was established by X-ray crystallographic technique.

2. Experimental section

2.1. Materials and reagents

Ofloxacin, 2,2′-bipyridine were commercially obtained and used without further purification. Hydrated metal salt Cu(ClO_4)$_2$·6H_2O, was purchased from the British Drug House (BDH) Poole, England. Analytical grade solvents were employed during all synthesis and were distilled before use. All the microorganisms used for the antibacterial activity were received as gifts from The Maharaja Sayajirao University of Baroda, India.

Metal (II) perchlorate salts are very explosive and require handling with extreme care.

3. Synthesis of complex

3.1. Synthesis of [Cu(ofx)(2bpy)(H_2O)].ClO_4·2H_2O

To a 20 ml methanolic solution of 2bpy (1.562 g, 10 mmol),10 ml aqueous solution of Cu(ClO_4)$_2$·6H_2O (3.705 g, 10 mmol) was added, followed by the addition of a freshly prepared solution of ofx (3.613 g,10 mmol) already deprotonated with KOH (0.561 g, 10 mmol) in water. The solution pH was adjusted to 7.5 using a few drops of 1 M HCl solution. There was the instant formation of a microcrystalline green compound which was separated by filtration and washed with distilled water. Elemental analysis data was in agreement with the general formula [Cu(ofx)(2bpy)(H_2O)].ClO_4·H_2O Data obtained were as follows: Found (%): C = 47.23, H = 4.90, and N = 9.34; Calculated (%): C = 47.00, H = 4.37, and N = 9.79. The compound was recrystallized in acetonitrile solution, after standing at room temperature for 3 weeks, suitable single green crystals for X-ray determination were obtained and the formula was established as [Cu(ofx)(2bpy)(H_2O)].ClO_4·2H_2O.

The synthesized Cu(II) complex structure was further confirmed by a single-crystal X-ray diffraction after positive elemental analysis. The reaction pathway is shown below in Scheme 1:

Complex: Green; Yield: 82%; M. wt: 727.19 gmol^{-1}; M. pt: 204.50 °C; **Elemental analysis:** Calc. for [Cu($C_{28}H_{32.29}FClN_5O_{10.65}$)] (%):C, 45.84; H, 4.53; N, 9.55%. Found: C, 46.25; H, 4.47; N, 9.63%**IR (KBr pellet, cm^{-1})**υ(C═O)$_{py}$,1593;υ$_{asym}$(COO$^-$),1622; υ$_{sym}$(COO$^-$), 1367;υ(C═N), 1516 ;Δ = ν(COO$^-$)$_{asy}$ – ν(COO$^-$)$_{sy}$: 255 cm^{-1};**UV–Vis (in DMSO) nm(cm^{-1})**λ (nm):639(2500), 302(62,484), 260(28,687). The complex is soluble in methanol, acetonitrile, DMSO and DMF and is electrolyte (88.2 Ω^{-1}cm^{2}mol^{-1}).

3.2. Instrumentation

FTIR spectra of the parent ligand and the newly obtained Cu(II) complex were found in the range of 4,000 cm^{-1} – 400 cm^{-1} in the form of KBr pellets on an FTIR-8501 Shimadzu Spectrometer**.** Electronic absorption spectra (200–1000 nm) were recorded using JENWAY 6405 UV–Vis spectrophotometer. The absorption spectra were recorded as solutions in DMSO. Thermo-gravimetric analysis measurement (TGA) was performed under N_2 atmosphere within the temperature range from room temperature to 550 °C using TA instrument TAQ-500. A sample of 4 mg was heated at 10 °C min^{-1} using an aluminum pan. C, H, and N elemental analysis were performed on a Thermo Finnigan Italy, FLASH EA 1112 series. X –band electron spin resonance (ESR) spectra at liquid nitrogen temperature (LNT) and ambient/room temperature (RT) were recorded on a JES – FA200 ESR Spectrometer on X band, JEOL, Japan with 100 kHz modulation frequency. Single crystal X-ray diffraction data were collected on X'calibur, Eos, Gemini, CCD area-detector diffractometer. Melting point determination was carried out using the MPA100 Optimelt automated melting point system (SRS) and the molar conductance measurement (1x10^{-3}) in DMSO solution was measured on EQ 660B based conductivity meter with a cell constant of 1.00. All measurements were done at room temperature utilizing freshly prepared solutions. The DFT calculations were achieved using the Gaussian 09 suite program [28] on the Lengau cluster machine of the Centre for High Performance Computing (CHPC) South Africa.

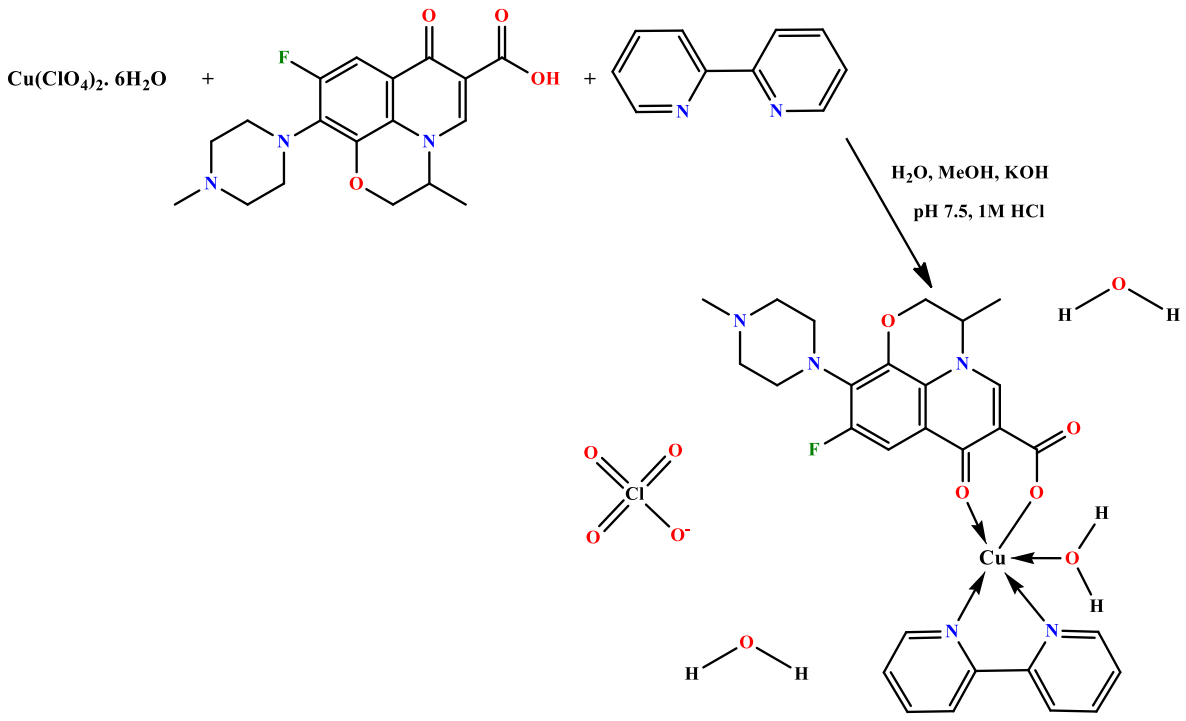

Scheme 1. Synthetic route of the complex.

3.3. X-ray crystal structure determination

Slow crystallization from acetonitrile solution yielded dark green crystals. A crystal of 0.25 × 0.20 × 0.20 mm dimension, suitable for single crystal X-ray diffraction was selected. X-ray intensity data of 33,271 reflections were collected on a X'calibur CCD area-detector diffractometer with graphite monochromated MoKα radiation (λ = 0.71073 Å). The single-crystal X-ray crystallographic data for the complex is summarized in Table 3. The structure was solved by SHELXS97, [29] and refined using SHELXL18 software refinement package [30]. Graphics were generated using MERCURY software 4.2 [31]. The structure was solved by direct methods and refined by the full-matrix least-squares based on F^2 technique using SHELXS97 program package [29]. All non-hydrogen atoms of the molecule were located in the best E-map. Full-matrix least-square refinement was determined using SHELXL97 [29]. An ORTEP [32] view of the complex with 50% ellipsoid probability is seen in Fig. 2a [33]. The molecule geometry was determined using the software PLATON [34] and PARST [35].The CCDC number for the complex is 2022672.

3.4. Antimicrobial activity – zone of inhibition study

To determine the antimicrobial potency of the compounds (ofx and complex), five different bacterial strains including Gram (+) *Bacillus subtilis, Staphylococcus aureus, Bacillus megaterium*, and Gram (−) *Salmonella typhi, Escherichia coli* were used. The result obtained was compared with the parent ligand ofx. The agar disk diffusion method was employed; 6.0 g of nutrient agar and 0.9 g of agar-agar were dissolved in 300 ml of autoclaved distilled water. The agar solution was heated for 15 min and then placed in an autoclave to sterilize at 121 °C. The heated nutrient agar was cooled and inoculated with standardized inoculums of the test microorganisms. The preparation of the stock solution was accomplished by dissolving the ligand and complex in DMSO solution to make the final concentration of 5 mg/mL. Filter paper disk of 6 mm in diameter was prepared and filled with 2 different volumes (2 µL and 4 µL) of the test compound to get 10 µg/ml and 20 µg/ml

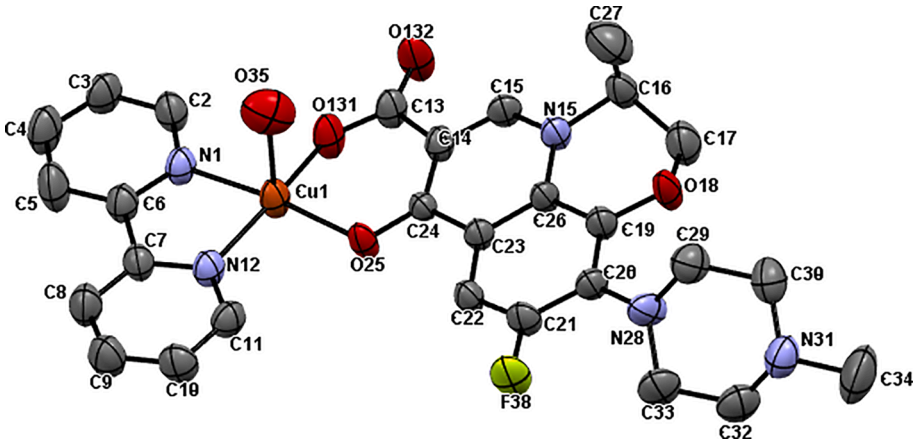

Fig. 2a. ORTEP view with 50% probability level of the complex. Hydrogen atoms and water solvate molecules are omitted for clarity. Perchlorate ion is disordered. For clarity, the disordered components have been excluded during plotting.

concentration on the disk surface [36]. The Petri dishes were incubated under reasonable conditions for 24 h. On the diffusion of the synthesized complex, an inhibition zone was formed via inhibiting the growth of bacteria in the presence of the compound. The diameters of inhibition zones were determined.

3.5. Computational details

The theoretical studies on the complex ion; $[Cu(ofx)(2bpy)(H_2O)]^+$, ofloxacin (ofx), and 2,2′-bipyridine (2bpy) were carried out using the density functional theory (DFT). The initial structures for the DFT calculations were taken from the experimental X-ray structure of the cationic unit of the complex after editing it appropriately to remove the counter ion (ClO_4^-) and lattice H_2O molecules. The optimization and vibrational frequency calculations on the structures were done using the B3LYP method [37,38] and the 6-31G(d) basis set. The polarizable continuum solvation model (PCM) was used with acetonitrile as the solvent. The time-dependent density functional theory (TD-DFT) [39] at B3LYP/631-G(d) level of theory was used to characterize the electronic transitions. The combination of B3LYP with 631-G(d) basis set is considered the most suitable general purpose choice for DFT studies and has been shown to give better results in the computation of thermochemical, electronic, and structural properties for many classes of compounds [40,41]. The DFT calculations were done in the gas phase and in acetonitrile which is the solvent employed for the recrystallization of the complex. The thermochemical properties, bond properties, and the global molecular reactivity descriptors such as energies of the highest occupied molecular orbital (E_{HOMO}), lowest unoccupied molecular orbital (E_{LUMO}), HOMO-LUMO energy gap (ΔE), ionization energy (I), electron affinity (A), chemical potential (μ), electronegativity (χ), electrophilicity index (ω), global hardness (η) and global softness (S) were evaluated from the DFT calculations in order to better characterize the $[Cu(ofx)(2bpy)(H_2O)]^+$ and the two ligands. The HOMO and LUMO are collectively referred to as frontier orbitals and are important parameters for describing chemical behavior [42].

The energy gap (ΔE) between the HOMO and LUMO was evaluated as:

$$\Delta E = E_{LUMO} - E_{HUMO} \quad (1)$$

The ionization energy and the electron affinity were determined according to the Koopman's theorem as [43]

$$I = -E_{HUMO} \quad (2)$$

$$A = -E_{LUMO} \quad (3)$$

Similarly, the electronegativity (χ) was determined as the average of the ionization energy and electron affinity [44]

$$\chi = \frac{I + A}{2} \quad (4)$$

The chemical potential (μ) was defined as the negative of the electronegativity (χ) [45]

$$\mu = -\chi \frac{-(1 + A)}{2} \quad (5)$$

The electrophilicity index (ω) was evaluated from the values of chemical potential (μ) and the global hardness (η) of the molecule as: [46]

$$\omega = \frac{\mu^2}{2\eta} \quad (6)$$

The global hardness (η) was evaluated as the finite difference between the ionization energy (I) and electron affinity (A) [47]

$$\eta = \frac{I - A}{2} \quad (7)$$

The global softness (S) was defined as the inverse of the global hardness (η): [48]

$$S = \frac{1}{\eta} \quad (8)$$

4. Results and discussion

The complex is air-stable, insoluble in water but soluble in methanol, acetonitrile, DMF, and DMSO. The metal to ligand ratio in the complex showed 1:1:1 stoichiometry of the type [M: ofx: 2bpy] as seen from the complex analytical data and elemental analysis. The conductance of the solution (1×10^{-3} M) was measured and the molar conductance was also determined. The complex molar conductance value at room temperature was 88.2 $\Omega^{-1}cm^2mol^{-1}$revealing 1:1 electrolytic nature of the complex which implies the presence of a counter anion (perchlorate) [49].

4.1. Synthesis of the complex

The complex was prepared in a general way by the reaction of an equimolar amount of ofloxacin with $Cu(ClO_4)_2$ and 2,2′-bipyridine in the mixture of water and methanol solution. The elemental analysis data is consistent with the proposed stoichiometry and also in agreement with the empirical formulae obtained by single-crystal X-ray diffraction.

4.2. IR spectroscopy

The IR spectrum (Fig. S1) of $[Cu(ofx)(2bpy)(H_2O)].ClO_4{\cdot}2H_2O$ was compared with that of free ofx and 2bpy in order to study the binding and deprotonation mode of the ligand to the copper metal in the complex. Some characteristic absorption bands and frequencies of the ligand and Cu(II) complex are provided in (Table 1). In the IR spectrum of free ofx, the vibration band stretch for $\nu(C{=}O)_{acid}$ and $\nu(C{=}O)_{pyr}$ groups were found at 1710 and 1618 cm^{-1}. Upon coordination with the metal ion, the $\nu(C{=}O)_{acid}$ band disappeared and two new bands corresponding to the asymmetric $\nu\ (COO^-)_{asy}$ and symmetric $\nu(COO^-)_{sym}$ stretches appeared in the regions 1622 and 1367 cm^{-1} [50]. The difference $\Delta COO^- = \nu(COO^-)_{asy} - \nu(COO^-)_{sym}$ is a useful characteristic tool for determining the coordination mode of the ligands [51]. The difference in values of band shift for the complex is 255 cm^{-1}which is>200 cm^{-1}, indicating that the carboxylate group in the ligand is coordinated to the metal ion in a monodentate manner with proton displacement [52]. The shift in the absorption band of $\nu(C{=}O)_{pyr}$, from 1618 $cm^{-1}$to 1593 cm^{-1} for the complex spectra indicated the coordination of oxygen atom of the pyridone group to the metal ion [53]. On the other hand, the ν(C═N) band of the aromatic rings of 2bpy ligand located at 1580 cm^{-1} [54] showed a shift in the complex indicating the bonding of 2bpy through the C═N nitrogen atom. The medium band found in ofx at 3428 cm^{-1} due to ν(O—H); completely disappeared in the spectra of the metal complex indicating deprotonation of the carboxylic proton [55]. Complex showed broad band in the region 3360 cm^{-1}, which was due to the presence of a coordinated water molecule, and a very strong absorption for the metal complex at 1088 cm^{-1} suggested the presence of the perchlorate counter-ion which was in agreement with the X-ray structure. The IR spectra of the complex showed the appearance of some new bands that were absent in the spectra of the free ligand in the region 512 and 437 cm^{-1} which confirmed the coordination of the metal ion via oxygen of its pyridone and carboxylate group of ofx(Cu–O) and pyridyl nitrogen of (Cu–N) [56,57]. From the overall changes in the IR spectra of the complex, it was concluded that ofx behaved as a bidentate ligand with O—O—donor atoms coordinated to the metal through the pyridone oxygen and deprotonated carboxylic oxygen. 2bpy also behaved as a bidentate ligand with N—N—donor atoms coordinated to the metal ion through the pyridyl nitrogen [58–60].

Table 1
Characteristic absorptions (cm^{-1}) in the IR spectra of the ligand and complex.

Ligand/complex	$\nu(C{=}O)_{acid}$	$\nu(COO^{-})_{asy}$	$\nu(C{=}O)_{pyr}$	$\nu(COO^{-})_{sym}$	Δ V	$\nu(C{=}N)$	ν(Cu–O)	ν(Cu–N)
Ofx	1710	–	1618	–	–	–	–	–
2,2′-bpy	–	–	–	–	–	1580	–	–
1	–	1622	1593	1367	255	1516	512	437

4.3. Electronic spectra studies

The electronic spectra of the Cu(II) complex were recorded in DMSO solution at room temperature. The spectra are shown in Figs. S2 and S3. The electronic spectrum of the complex showed a band at 260 nm which was attributable to $\pi \rightarrow \pi^*$ transition. Another absorption band at 302 nm could be assigned to charge transfers (LMCT). The low intensity and very broadband at 639 nm are attributed to $d \rightarrow d$ transition ($^2T_2 \rightarrow {}^2E$) for the Cu(II) atom which is a characteristic of a distorted square–pyramidal arrangement of the ligand donor atoms around the copper ion (Table 2) [61,62]. Thus, based on electronic spectral data, Cu(II) ion possessed square-pyramidal geometry by the addition of one water molecule and this was confirmed by the thermal studies.

4.4. Structure description of $[Cu(ofx)(2bpy)(H_2O)].ClO_4{\cdot}2H_2O$

Single crystal suitable for X-ray crystallographic analysis was obtained by the recrystallization of the precipitate understudied from acetonitrile solution resulting in the formation of dark green quality X-ray single crystal. The complex was mononuclear and crystallized in a triclinic system, P-1 space group with unit cell dimensions a = 10.2192 (13), b = 12.7080(19), and c = 12.8156(16). An ORTEP view of the complex with its atom numbering scheme is shown in Fig. 2(a). Single crystallographic data and molecular structure refinement data are presented in Table 3 as well as a comparison of some selected bond lengths and bond angles from x-ray and DFT studies are presented in Table 4.

Complex showed coordination scheme as CuN_2O_3 type comprising of one Cu(II) atom, one quinolone ligand in its anionic form (ofx^-), one bidentate (2bpy), and one water molecule which together formed cationic units $[Cu\text{-}(ofx)(2bpy)(H_2O)]^+$, as well as a disordered perchlorate counter anion which neutralized the charge and two lattice water molecules that provided crystalline stability through hydrogen-bond network interactions. Perchlorate is twofold disordered. The disorder components are in the ratio 64:36. In unit cells where minor component is absent, there exist water molecules (O36) with the occupancy of major component of ClO_4.

The crystal structure was stabilized by numerous hydrogen bonds of type O(water)–H … O, O(water)-H…N. Moreover, we had seen that the water molecule was not only playing as a solvent of crystallization but also as a ligand but the hydrogen atoms of partially occupied water molecules could not be located from the Fourier map; however, their contributions were involved in the empirical formulae. A packing diagram and table showing the intermolecular H-bond network are shown in Fig. 2(b) and Table 5.

The two nitrogen atoms [N(1) and N(12)] from a 2bpy molecule with distances of [Cu(1)-N(1)] 2.022(5)°Å, [Cu(1)-N(12)] 1.986(5)°Å and two oxygen atoms (i.e. pyridone oxygen and carboxylate oxygen atoms) [O(25) and O(1 3 1)] from its quinolone ligand with distances of [Cu(1)-O(1 3 1)] 1.902(4)°Å, [Cu(1)-O(25)] 1.967(4)°Å made up the equatorial plane of the coordination polyhedron, while the axial position was occupied by water molecule with a longer Cu–O(35) distance of [2.276 (6) Å]. The two Cu–N bonds gave the bond length of 1.986(5) Å and 2.022(5) Å which concurred favorably with the expected range usually observed for copper complexes [63]. An arrangement similar to that of the bipy ligand had been observed in a series of some neutral mononuclear Cu(L)(bipy)(H_2O)complexes [5] (L = a monodentate phenoxyalkanoato ligand), where O_{water} lies at the apical position [64]. The uncoordinated carboxylato oxygen atom O(1 3 2) [Cu(1)…O(1 3 2) = 3.994 Å] lied above the basal plane of the pyramid. The dihedral angle between the main skeleton of the two adjacent ligands is 78.35°.The angles in the coordination polyhedron Fig. S5 varied from 81.3(2) to 95.5(2) for the complex and these ranges were similar to those found in other mixed copper quinolone complexes [63,65].

Table 4 gives a comparative analysis of some selected experimental and calculated bond distances and bond angles. The significance of the differences between experimental and calculated values of the bond lengths and bond angles was determined by the root means square error (RMSE) which is expressed as:

$$RMSE = \sqrt{\frac{\sum (y_i - \widehat{y_i})^2}{n}}, \tag{9}$$

where y_i *and* $\widehat{y_i}$ are the experimental and calculated values respectively.

Alternatively,

$$RMSE = \sqrt{1 - r^2} x SD_y \tag{10}$$

where r is the residuals (experimental value – calculated value) and SD is the standard deviation.

The results of the bond properties revealed that the experimental and calculated values were approximately equivalent with the exception of

Table 2
UV–Vis data of complex.

Complex	λ_{max}, nm (ε, $10^3 M^{-1}\ cm^{-1}$) $\pi \rightarrow \pi^*$	d-d band	C-T band
1	260(28,687)	639(2,500)	302(62,484)

Table 3
Crystal data and structure refinement parameters for the complex.

Empirical formula	$C_{28}H_{32.29}ClCuFN_5O_{10.65}$
Formula weight	727.19
Temperature/K	298(2)
Crystal system	Triclinic
Space group	P-1
a/Å	10.2192(13)
b/Å	12.7080(19)
c/Å	12.8156(16)
α/°	78.772(12)
β/°	70.244(11)
γ/°	84.093(11)
Volume/$Å^3$	1535.1(4)
Z	2
$\rho_{calc}g/cm^3$	1.573
μ/mm^{-1}	0.872
F(0 0 0)	751.0
Crystal size/mm^3	0.250 × 0.200 × 0.200
Radiation	Mo Kα (λ = 0.71073)
2Θ range for data collection/°	5.992 to 52
Index ranges	$-12 \le h \le 12$, $-15 \le k \le 15$, $-15 \le l \le 15$
Reflections collected	33,271
Independent reflections	6034 [R_{int} = 0.1176, R_{sigma} = 0.0945]
Data/restraints/parameters	6034/378/483
Goodness-of-fit on F^2	1.084
Final R indexes [I>=2σ (I)]	R_1 = 0.0911, wR_2 = 0.2038
Final R indexes [all data]	R_1 = 0.1360, wR_2 = 0.2320
Largest diff. peak/hole / e $Å^{-3}$	0.81/−0.50
Color	Green
CCDC	2022672

Table 4
Selected bond lengths (Å) and angles (°) from X-ray and DFT studies (esd's are reported in parenthesis, esd = 0 where not reported).

Bond distance (Å)				Bond angles (°)			
Bond	Exptal	Calc.	RMSE	Bond	Exptal	Calc.	RMSE
Cu(1)-O(131)	1.902(4)	1.903	0.00399	O(131)-Cu(1)-O(25)	92.4(17)	93.3	0.00323
Cu(1)-O(25)	1.967(4)	1.952	0.00399	O(131)-Cu(1)-N(12)	169.2(19)	174.7	0.55575
Cu(1)-O(35)	2.276(6)	2.273	0.00599	O(25)-Cu(1)-N(12)	92.2(17)	91.9	0.01547
Cu(1)-N(1)	2.022(5)	1.993	0.00499	O(131)-Cu(1)-N(1)	91.3(19)	93.2	0.04959
Cu(1)-N(12)	1.986	1.969	0	O(25)-Cu(1)-N(1)	173.3(19)	147.2	12.92399
				N(12)-Cu(1)-N(1)	81.3(2)	81.9	0.00128
				O(131)-Cu(1)-O(35)	92.2(2)	84.8	0.10752
				O(25)-Cu(1)-O(35)	92.2(19)	107.4	4.37076
				N(12)-Cu(1)-O(35)	95.9(2)	94.6	0.00138
				N(1)-Cu(1)-O(35)	92.5(2)	105.2	0.32058
				C(11)-N(12)-Cu(1)	125.9(4)	124.6	0.00276
				C(7)-N(12)-Cu(1)	115.6(4)	115.7	0.00396
				C(6)-N(1)-Cu(1)	113.9(4)	115.0	0.00084
				C(2)-N(1)-Cu(1)	126.9(4)	125.5	0.00384
				C(24)-O(25)-Cu(1)	122.5(4)	126.2	0.05076
				C(13)-O(131)-Cu(1)	128.0(4)	130.8	0.02736

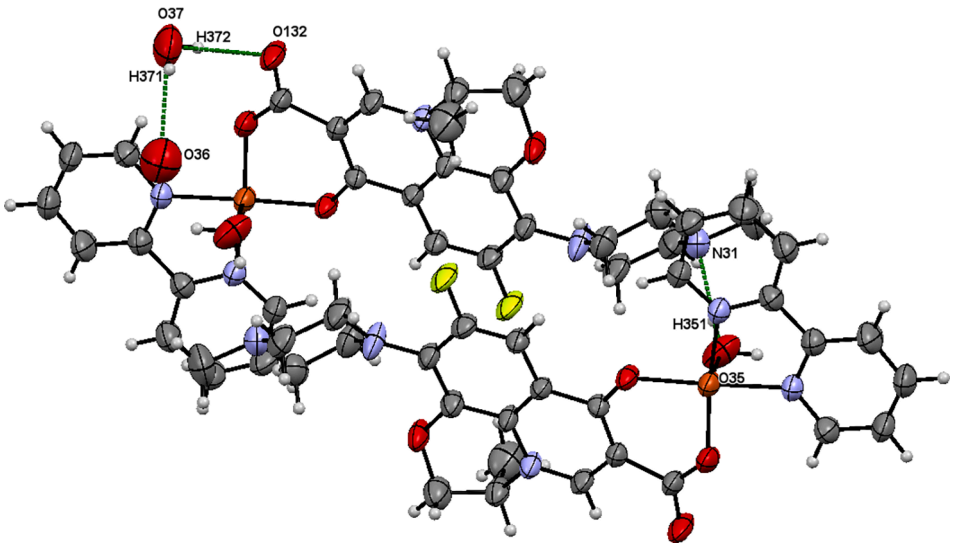

Fig. 2b. Intermolecular hydrogen bonding showing O—H…O, O—H…N interactions in the complex. Green lines indicating H-Bond. The water molecule and the disordered perchlorate ion are omitted for clarity. For clarity, the disordered component has been excluded during plotting.

Table 5
Hydrogen – bonding parameters for the complex (D, donor; A, acceptor).

Complex	D-H…A	D-H (Å)	H…A (Å)	D…A (Å)	D-H…A (°)
1	O(37)-H(372)-O (132)	0.850	1.915	2.749	166.50
	O(37)-H(371)-O(36)	0.850	2.224	2.755	120.50
	O(35)-H(351)-N(31)	0.860	1.962	2.807	166.81

two bond angles; O(25)-Cu(1)-N(1) and O(25)-Cu(1)-O(35) that have significant difference between the experimental and calculated values. Thus, the coordination polyhedron of the structure obtained experimentally was theoretically confirmed as the optimized structure for the $[Cu(ofx)(2bpy)(H_2O)]^+$ complex ion as evident from the bond distances and bond angles of the N and O atoms directly coordinating to the Cu^{2+} atom.

To determine whether this five-membered motif structure is either square-pyramidal (SP) or trigonalbipyramidal (TBP), the value of the Addison parameter tau descriptor (τ) [66] was considered. Tau (τ) parameter as a trigonality index measures the degree of distortion and was defined as ($\tau = (\alpha - \beta)/60$ (where α and β are the two largest angles around the central atom),[α = O(25)-Cu(1)-N(1) = 173.33(19)° and β = O(131)-Cu(1)-N(12) = 169.24(19)°] [66–68].Values of (τ) were between zero and unity (τ = 0 and unity for perfect square-pyramidal SP and trigonal–bipyramidal TBP geometries respectively). The τ, which had been calculated for Cu, was 0.068, indicating that distortion occurs in regular square-based pyramidal geometry. The tetragonality factor ($T^5 = R_S/R_L$) of the complex is 0.839 as calculated from the changes in the bond lengths which is similar to the calculated mean of ca. 0.84 for previously reported Cu(II) complexes [69]. These two parameters (T^5 and τ) confirmed that the distortion that occurred in the coordination geometry around the copper atom was best represented as a distorted square-based pyramidal geometry.

Crystal determination resolution further confirmed that coordination took place through the O_{acid} and O_{pyr} group, in a similar way to other complexes with quinolone derivatives cited above.

4.5. Thermal studies

For the investigation of the thermal properties, the thermogravimetric analysis (TGA) of Cu(II) mixed-ligand complex was carried out in the temperature range 30–550 °C under N_2 atmosphere at a rate of 10 °C min^{-1}. The Cu(II) thermo-gram (Fig. 3) decomposed in

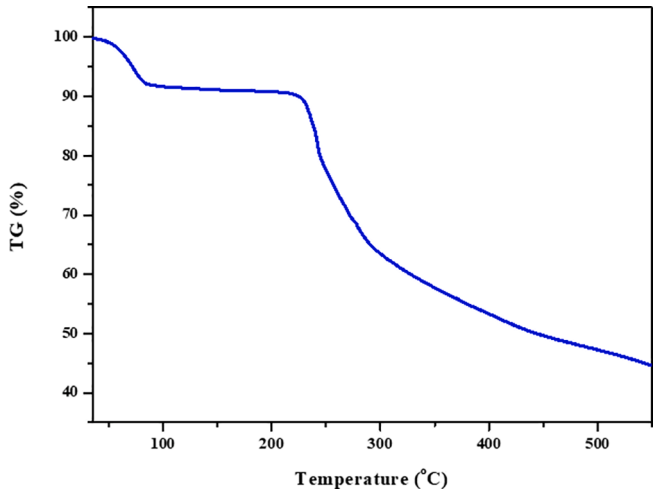

Fig. 3. TGA curve of complex.

three successive steps. The first curve showed the first stage of decomposition at 40–100 °C with a practical weight loss of 7.40% Cald. 7.43%. This was attributed to the elimination of one coordinated water and two lattice water molecules. Furthermore, the complex underwent decomposition at 242 °C with a practical weight loss of 20.88% (Cald. 21.48%), which corresponded to a weight loss of 2bpy molecule. The third estimated weight loss within the temperature range might be attributed to the loss of ofx leaving CuO as the final decomposition product (found 48.0%, Cald.49.69%). The experimental result for mass loss agreed with the calculated for the three decomposition stages. The table of the thermo-analytical data of the complex is shown in Table S1.

4.6. EPR spectral study of the Cu(II) complex

The powdered as well as the solution EPR spectra of the complex were studied. X-band EPR spectra of polycrystalline Cu(II) complex at room temperature (RT) and solution at liquid nitrogen temperature (LNT) are shown in Figs. 4(a) and 4(b).

The EPR spectra in frozen solution of the complex were indicative of S = 1/2 and no Δ Ms = ±2 (half field) transition was observed and features for half-field signals were not also observed. The derived EPR

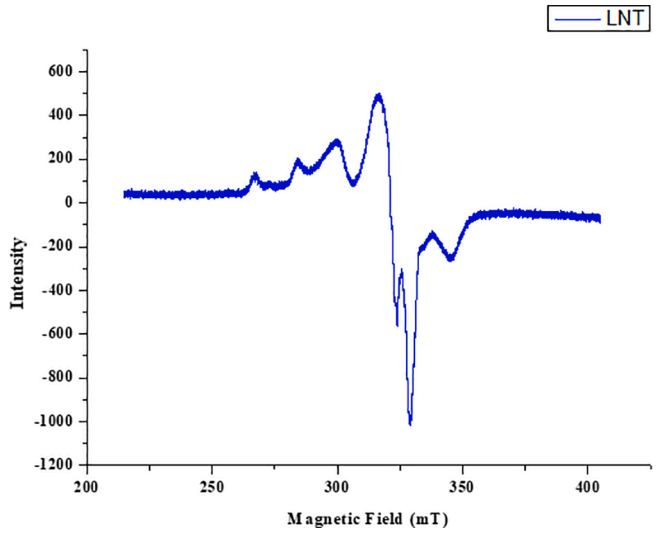

Fig. 4a. X-band EPR spectra of [Cu(ofx)(2bpy)(H_2O)].ClO_4·2H_2Ocomplex in DMSO solution at LNT. EPR conditions for LNT: microwave power, 0.9950mW, modulation amplitude 70.0, microwave frequency 9.19GHZ, modulation frequency 100 kHz.

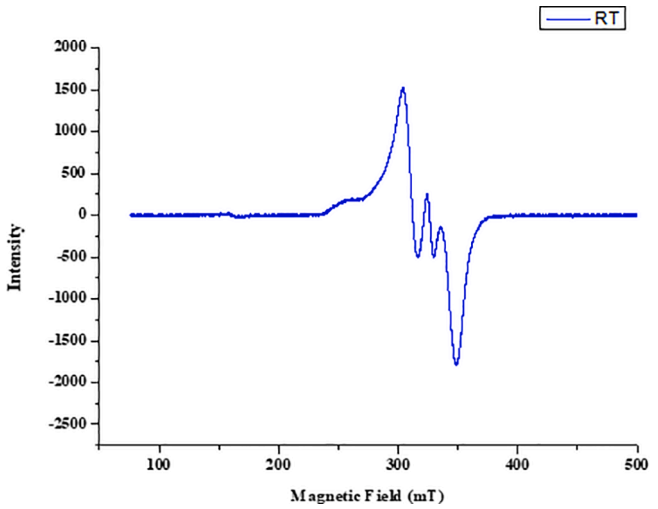

Fig. 4b. X-band EPR spectra of [Cu(ofx)(2bpy)(H_2O)].ClO_4·2H_2O complex in polycrystalline state at RT EPR conditions for RT: microwave power, 0.9950mW, modulation amplitude 80.0, microwave frequency 9.45GHZ, modulation frequency 100 kHz.

Hamiltonian spin parameters for the complex at LNT in Table 6 are $g_{\|}$ = 2.145, $g_{\perp}$= 2.033, $A_{\|}$=169G(170 $^{\times}10^{-4}$ cm^{-1}), and G = 5, which was normally observed only in magnetically diluted Cu(II) complexes. The EPR spectrum showed the usual line shape similar to mononuclear complexes with $g_{\|} > g_{\perp} > 2.0023$ indicating an axial symmetry. The trend of $g_{\|}(2.145) > g_{\perp}(2.033) > 2.0023$ values indicated that the unpaired electron of Cu(II) resided in d^{22}_{x-y} orbital having $^2B_{1g}$ at the ground state, which was indicative of square-pyramidal geometry of the complex [70]. The $g_{\|}$ value was an important parameter for indicating the covalent character of the metal–ligand bond, $g_{\|} < 2.3$ for covalent characters and $g_{\|} > 2.3$ for ionic respectively, [71] thus $g_{\|}$ value of 2.145 obtained for the complex understudy, was less than 2.3 which indicated covalency for the metal–ligand bond. The g-value of the complex was related to the exchange-coupling parameter between the copper center (G) and was calculated for each axial species using the expression G= ($g_{\|}$-2.0023/ $g_{\perp}$-2.0023) according to the literature [69]. The calculated G-value was found to be 5 which is greater than 4. The value of exchange interaction term G > 4 inferred that there was negligible interaction between the copper center in the complex [72].

The derived Hamiltonian parameters ($g_{\|}$, $g_{\perp}$, and $A_{\|}$) were used to estimate the bonding parameters α^2(covalent in-plane σ-bonding) and β^2 (covalent in-plane π-bonding). When the molecular orbital coefficient $\alpha^2 = 0.5$, it indicated a complete covalent bonding between a ligand and the metal ion, but when α^2 = unity, it suggested a complete ionic bonding [73,74].The obtained value of α^2 = 1.524 and β^2 = 0.285 indicated that complex was mainly ionic and an in-plane π-bonding was present. From the above values observed, it indicated that there was interaction in the out- plane π- bonding whereas in-plane σ-bonding was completely ionic which was verified by orbital reduction factors $K_{\|}$ and $K_{\perp}$.

$K_{\|} \approx K_{\perp}$ in the case of pure σ- bonding, but when $K_{\|} < K_{\perp}$, it indicated an in-plane π- bonding while $K_{\|} > K_{\perp}$ for out plane π- bonding [69]. Based on the observed trend, $K_{\|}(0.434) > K_{\perp}(0.090)$, it implied a greater contribution from out-plane π- bonding than in-plane π- bonding in Metal to ligand π bonding.

4.7. Antimicrobial activity of the parent ligand and its copper complex

The potency of the parent ligand and its Cu(II) complex was evaluated by monitoring the growth of five organisms, three Gram (+) strains namely *Bacillus subtilis*, *Staphylococcus aureus, Bacillus megaterium*, and two Gram (-) *Salmonella typhi*, *Escherichia coli*by the agar disk diffusion

Table 6
X-band EPR Hamiltonian parameters for Cu(II) complex.

Complexes	$g_{\|}$	$g_{\perp}$	g_{iso}	G	$A_{\|}$ (cm^{-1})	α^2	β^2	$k_{\|}$	$k_{\perp}$
1	2.145	2.033	2.070	5	169.36	1.524	0.285	0.434	0.090

Table 7
Antimicrobial activity of ofx, and its Cu(II) complex evaluated by the zone of diameter in (mm).

Zone of inhibition (mm)	*E. coli*		*S. typhi*		*B. megatarium*		*B. subtilis*		*S. aureus*	
Compound/Conc.	10 μg/ml	20 μg/ml	10 μg/ml	20 μg/ml	10 μg/ml	20 μg/ml	10 μg/ml	20 μg/ml	10 μg/ml	20 μg/ml
Ofx	29	30.5	24	29	36	31	43	44	33.5	37
Complex	31.5	31	34	36.5	36.5	37.5	43.5	47	35	39

method [75]. The results of the antimicrobial test given by the zone of inhibition (mm) in the concentration of 10 μg/ml and 20 μg/ml per disk are presented in (Table 7). It was evident from the obtained data that the coordination of the ofx ligand with Cu(II) in the presence of 2bpy results into superior antimicrobial complex against *E. coli, S. aureus, S. typhi, B. subtilis, and B. megaterium* which might be due to the complexation of the metal ion with ligand; [76,77] while the same level of efficacy was observed against *B. megaterium on* 10 μg/ml level of exposure. The complex exhibited the best inhibition against *B. subtilis* at 20 μg/ml concentration. The results also agreed with the finding of other researchers that antibacterial potency is usually concentration-dependent [78,79]. The enhanced activity of the Cu(II) complex was expected when the biological role and the activity of copper [80,81] were considered since the nature of the metal ion coordinated to a drug might have a significant role to this diversity. For metal complexes showing higher antimicrobial activity, the following five principal factors [7,82,83] should be considered: (i) The chelate effect, i.e. Ligands that are bound to metal ions in a bidentate way like quinolones, 2bpy, bipym, and phen showed better antimicrobial effectiveness towards complexes than monodentate Nitrogen-donor ligands e.g., pyridine; (ii) the total charge of the complex. Generally, the antimicrobial efficiency decreases in the order cationic > neutral > anionic complex; (iii) the nature of the ligands; (iv) the nuclearity of the metal center in the complex. Generally, dinuclear metal centers are more active than mononuclear ones; (v) the nature of the ion neutralizing the ionic complex.

Thus, factors (i) and (iii) of the five factors mentioned above were present in the complex; i.e. the nature of the ligands and the chelate effect provided by both the quinolone (ofx) and the Nitrogen-donor ligand (2bpy) which could be considered increasing the antimicrobial activity. The antimicrobial activity chart is depicted in Fig. 5.

5. Computational studies

5.1. Geometrical structure of complex

The results of thermochemical properties of the $[Cu(ofx)(2bpy)(H_2O)]^+$, the free ligands (ofloxacin), and 2,2′-bipyridine) and $Cu(ClO_4)_2{\cdot}6H_2O$ in acetonitrile are shown in Table 8. The values for enthalpy (H), entropy (S) andGibb's free energy (G) for the formation of the reacting species and the productswere as obtained after correction with the zero-point energy (ZPE) and the thermal electronic energy (ΔH_{ele}) at 298.15 K. Thevalue of ΔH and ΔG for thereaction are obtained as -8.0×10^3kJmol^{-1} from the expressions:

$$\Delta H = \sum \Delta H_{products} - \sum \Delta H_{reactants} \quad (11)$$

$$\Delta G = \sum \Delta G_{products} - \sum \Delta G_{reactants} \quad (12)$$

The estimated negative values of ΔH and ΔG for the reaction by the DFT studies confirmed that the formation of the $[Cu(ofx)(2bpy)(H_2O)]^+$ (Fig. 6) through the experimentally proposed reaction path and conditions is an exothermic and thermodynamically feasible process.

Fig. 7 showed the molecular orbitals surface plots for the HOMO-LUMO of $[Cu(ofx)(2bpy)(H_2O)]^+$. The HOMO orbitals were primarily electron donor whereas LUMO was electron acceptor. Similarly, the gap between HOMO and LUMO described the chemical stability of molecules [84]. For the $[Cu(ofx)(2bpy)(H_2O)]^+$, the electron density of the HOMO were largely distributed on the 2,2′-bipyridine (2bpy) ring and the outer heterocyclic ring of the ofloxacin ligand while the electron density of the LUMO was only distributed on the 2,2′-bipyridine (2bpy) ring. This might be connected to the fact that 2bpy being an N, N-bidentate ligand that has both σ-donating and π-accepting characters which resulted in a low-lying LUMO with better π-electron interaction between its two *N*-atoms and the Cu atom than the two O-atoms of the ofx. Thus, the formation and stabilization of the $[Cu(ofx)(2bpy)(H_2O)]^+$ largely depend on the electronic charge transfer (CT) transitions between the d-orbitals of the Cu atom and the heteroatoms of the 2bpy and the ofx.

In the free ofloxacin and 2,2′-bipyridine ligands; the HOMO and LUMO surface plots showed that electron densities were well distributed around the unsaturated carbon atoms and the heteroatoms since the most favorable electronic transitions in these molecules were the $n \rightarrow \pi^*$ and the $\pi \rightarrow \pi^*$ transitions.

The global molecular descriptor as evaluated from the DFT calculations is presented in Table 9. The $[Cu(ofx)(2bpy)(H_2O)]^+$ has a small HOMO-LUMO energy gap (ΔE) value of 0.951 eV indicating that the complex ion has highly mobile π-electrons from the π-orbitals of its heteroatoms and conjugated systems and this conferred extra stability on it. The correspondingly high values of the other molecular descriptors (I, A, χ, μ, and ω) further substantiated the stability of the complex ion. The relatively small global hardness value ($\eta = 0.475$) indicated high polarizability and magnetizability of the complex ion. The greater reactivity of 2,2′-bipyridine in the formation of the complex ion was further corroborated with its higher ΔE value of 5.00 *eV* as compared to that of ofloxacin (3.522 eV) since the smaller ΔE value for ofloxacin implied greater stability.

6. Conclusion

A new Cu(II) mononuclear complex with CuN_2O_3 chromophore has been described and the molecular structure was elucidated by single-crystal X-ray spectral method. Ofx as the second generation quinolone and 2bpy, which form a stable complex with Cu(II), have been produced and characterized by physicochemical and spectroscopic techniques. A single-crystal X-ray diffraction data revealed that the crystal has intermolecular H-bonds and a distorted square-bipyramidal geometry around the metal center. Based on spectroscopic studies, the coordinating factor of the ligands has been proved on a complexation reaction with Cu(II) ion. The metal ion was coordinated through the pyridone and carboxylate oxygen atom of ofx via deprotonation and pyridyl nitrogen of 2bpy. ESR spectral data confirmed the mononuclear nature of the complex. The molar conductance in DMSO revealed the electrolytic

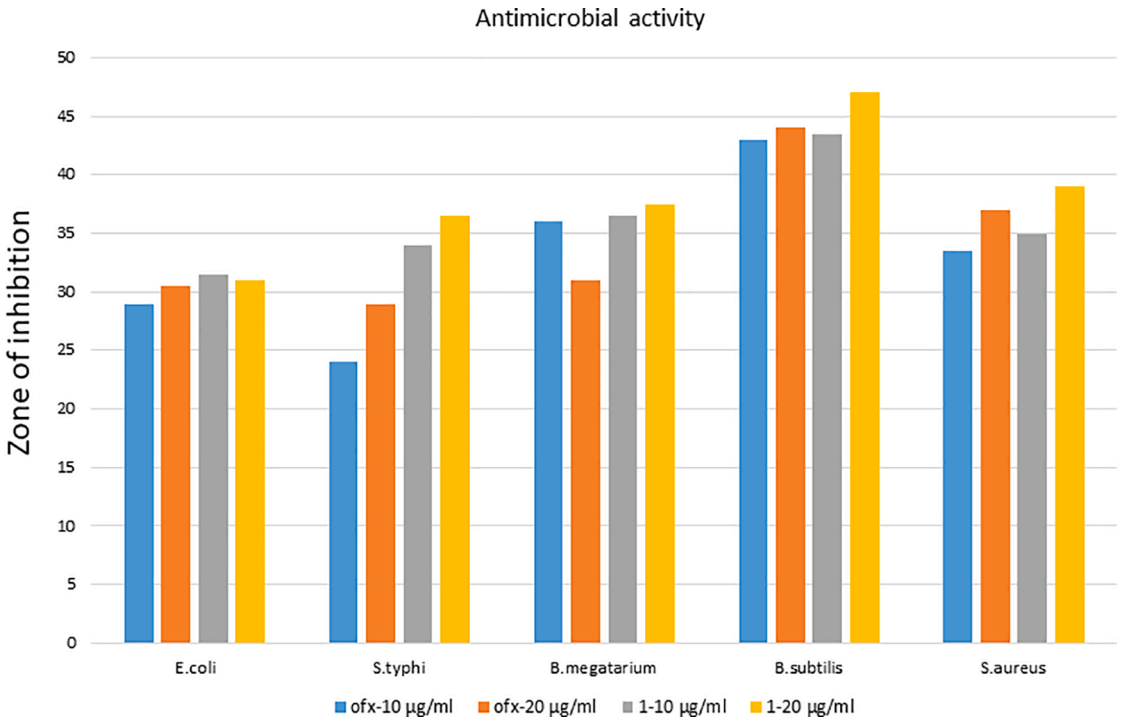

Fig. 5. Antimicrobial activity chart.

Table 8
Thermochemical properties from DFT calculations at 298.15 K using acetonitrile as solvent.

Compound	Zero-point energy (ZPE) [kJmol^{-1}]	Internal Energy (U) [kJmol^{-1}]	Enthalpy (H) [kJmol^{-1}]	Entropy (S) [kJmol^{-1}]	Gibb's Free Energy (G) [kJmol^{-1}]
$Cu(ClO_4)_2{\cdot}6H_2O$	396.555	-4.497×10^6	-4.497×10^6	0.547	-4.497×10^6
2,2′-bipyridine	414.834	-1.300×10^6	-1.300×10^6	0.365	-1.300×10^6
Ofloxacin	1000.788	-3.316×10^6	-3.316×10^6	0.672	-3.316×10^6
$[Cu(ofx)(2bpy)(H_2O)]^+$	1507.210	-9.124×10^6	-9.124×10^6	1.002	-9.124×10^6
ClO_4^-	27.364	-1.997×10^6	-1.997×10^6	0.286	-1.997×10^6

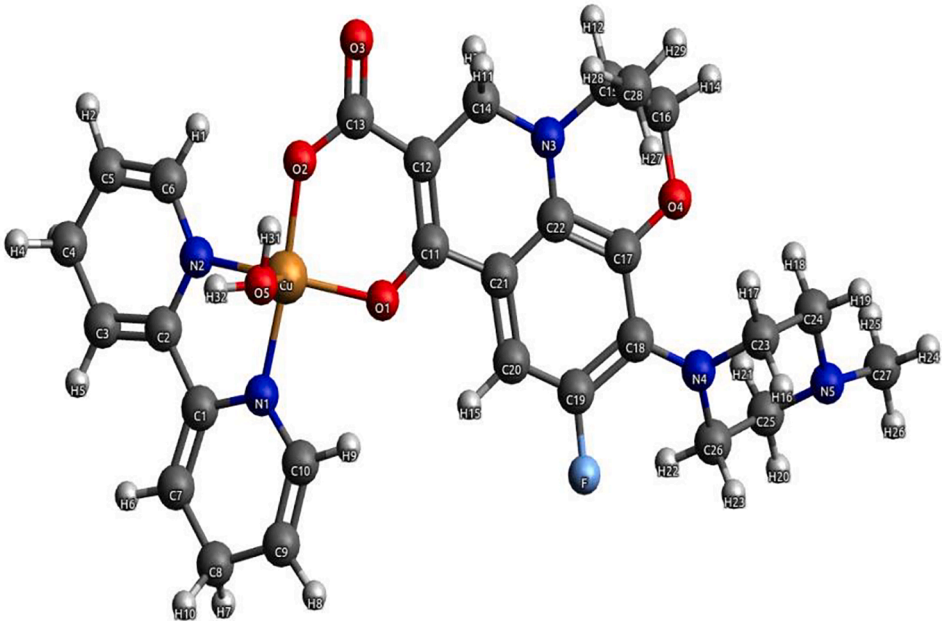

Fig. 6. The optimized structure of $[Cu(ofx)(2bpy)(H_2O)]^+$ using DFT calculations.

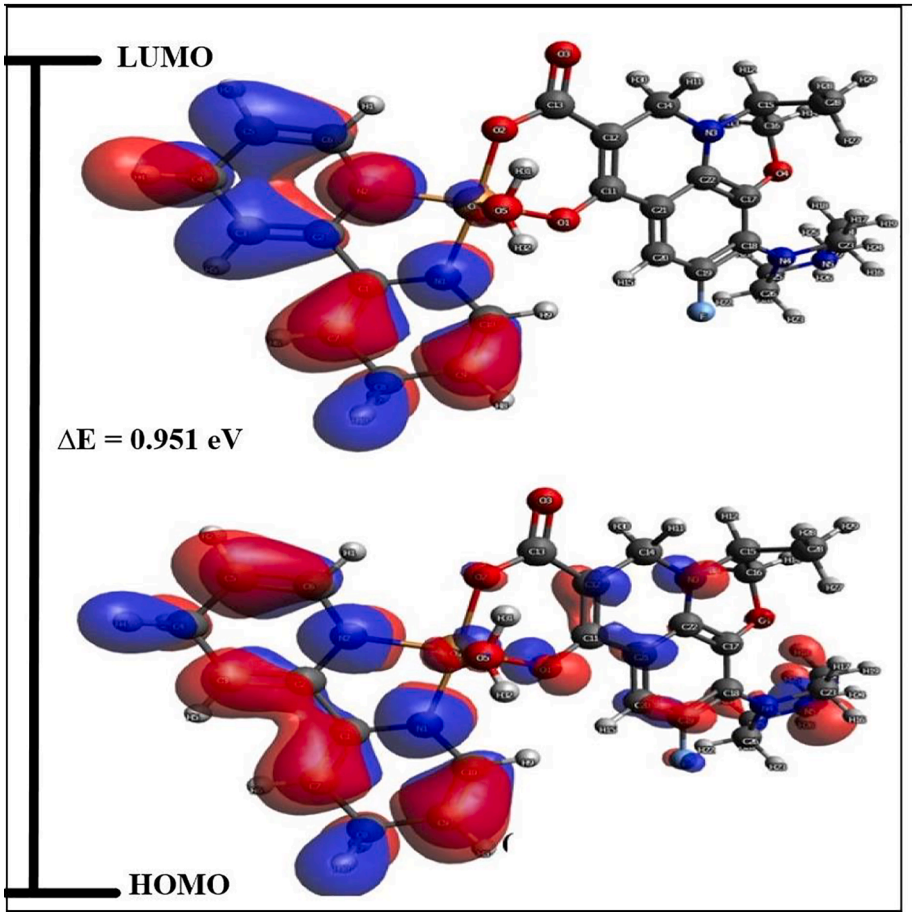

Fig. 7. HOMO and LUMO surface representation for $[Cu(ofx)(2bpy)(H_2O)]^+$ using DFT calculations.

Table 9
Molecular descriptors.

Parameters (eV)	$[Cu(ofx)(2bpy)H_2O]^+$		Ofloxacin		2,2′-bipyridine	
	Gas	Acetonitrile	Gas	Acetonitrile	Gas	Acetonitrile
E_{HOMO}	−10.580	−6.070	−5.250	−5.124	−6.004	−6.296
E_{LUMO}	−9.724	−5.119	−1.653	−1.602	−1.180	−1.296
ΔE (E_{LUMO}-E_{HOMO})	0.856	0.951	3.597	3.522	4.824	5.000
I	10.580	6.070	5.250	5.124	6.004	6.296
A	9.724	5.119	1.653	1.602	1.180	1.296
η	0.428	0.475	1.799	1.761	2.412	2.500
S	2.336	2.105	0.556	0.568	0.415	0.400
χ	10.152	5.595	3.452	3.363	3.592	3.796
μ	−10.152	−5.595	−3.452	−3.363	−3.592	−3.796
ω	120.401	32.952	3.313	3.211	2.675	2.882

nature of the compound. The results obtained from DFT calculations have been compared with those obtained from the experimental (X-ray analysis) and agreements between them have been observed. The antimicrobial activity results showed that the complex has exhibited a better and higher activity when compared to its respective ligand. This compound can also be a promising addition of a new class of metallodrugs [85,86].

CRediT authorship contribution statement

Joshua Ayoola Obaleye: Supervision, Conceptualization, Project administration, Resources, Writing - review & editing. **Misitura Lawal:** Investigation, Formal analysis. **Rajendrasinh N. Jadeja:** Supervision, Conceptualization, Data curation, Resources. **Vivek Kumar Gupta:** Formal analysis, Visualization, Writing - review & editing. **Ginikachukwu Grace Nnabuike:** Investigation, Software, Visualization. **Mercy Oluwaseyi Bamigboye:** Investigation, Software, Visualization. **Hetal Roy:** Formal analysis, Visualization, Writing - review & editing. **Olaniyi Kamil Yusuff:** Investigation, Software, Visualization. **Poonam Bhagariya:** Formal analysis, Visualization, Writing - review & editing.

Declaration of Competing Interest

The authors declare that they have no known competing financial interests or personal relationships that could have appeared to influence the work reported in this paper.

Acknowledgements

ML Acknowledges DBT-TWAS Postgraduate Fellowship (FR number: 3240300011) and Kebbi State University of Science and Technology, Aliero, Kebbi State, Nigeria for granting me study leave, RNJ acknowledges Head, Department of Chemistry, the Maharaja Sayajirao University of Baroda for providing necessary facilities to carry out this research. JAO is grateful for the support from the Science and Technology Education Post-Basic Project (STEP-B), TETFUND, Department of Chemistry, University of Ilorin. The authors are thankful to SAIF IIT Mumbai for ESR measurements and CHN analysis and the Council for Scientific and Industrial Research (CSIR), Cape Town, South Africa, for granting them access to their High-Performance Computing resources for this work.

Appendix A. Supplementary data

Crystallographic data for the structure reported in this paper have been deposited with the Cambridge Crystallographic Data Center as supplementary publication no. CCDC 2022672. Copies of the data can be obtained free of charge from the CCDC (12 Union Road, Cambridge CB2 1EZ, UK; tel.: +44 1223 336 408; fax: +44 1223 336 003; email: deposit@ccdc.cam.ac.uk; http://www.ccdc.cam.ac.uk). Supplementary data to this article can be found online at https://doi.org/10.1016/j.ica.2021.120264.

References

[1] M.A. Zoroddu, S. Zanetti, R. Pogni, R. Basosi, J. Inorg. Biochem. 63 (1996) 291–300.
[2] S.S. Hindo, M. Frezza, D. Tomco, M.J. Heeg, L. Hryhorczuk, B.R. McGarvey, Q. P. Dou, C.N. Verani, Eur. J. Med. Chem. 44 (2009) 4353–4361.
[3] P.F. Liguori, A. Valentini, M. Palma, A. Bellusci, S. Bernardini, M. Ghedini, M. L. Panno, C. Pettinari, F. Marchetti, A. Crispini, D. Pucci, Dalton Trans. 39 (2010) 4205–4212.
[4] G. Psomas, C. Dendrinou-Samara, P. Philippakopoulos, V. Tangoulis, C. P. Raptopoulou, E. Samaras, D.P. Kessissoglou, Inorg. Chim. Acta. 272 (1998) 24–32.
[5] C. Dendrinou-Samara, G. Psomas, K. Christophorou, V. Tangolius, C. P. Raptopoulou, Terzis C. Dendrinou-Samara, G. Psomas, K. Tangoulis, V. P. Raptopoulou, A. Terzis, D.P. Kessissoglou, J. Chem. Soc. Dalton Trans. 12 (1996) 3737–3743.
[6] G. Psomas, C.P. Raptopoulou, L. Iordanidis, C. Dendrinou-Samara, V. Tangoulis, D. P. Kessissoglou, J. Inorg. Chem 39 (2000) 3042–3048.
[7] C. Dendrinou-Samara, G. Psomas, C.P. Raptopoulou, D.P. Kessissoglou, J. Inorg. Biochem. 83 (2001) 7–16.
[8] I. Turel, Coord. Chem. Rev. 232 (2002) 27–47.
[9] I. Turel, I. Leban, N. Bukovec, J. Inorg. Biochem. 56 (1994) 273–282.
[10] I. Turel, I. Leban, N. Bukovec, J. Inorg. Biochem. 66 (1997) 241–245.
[11] B. Macías, M.V. Villa, I. Rubio, A. Castiñeiras, J. Borrás, J. Inorg. Biochem. 84 (2001) 163–170.
[12] M. Kumar, G. Kumar, K.M. Dadure, D.T. Masram, New J. Chem. 43 (2019) 15462–15481.
[13] D.K. Saha, U. Sandbhor, K. Shirisha, S. Padhye, D. Deobagkar, C.E. Anson, A. K. Powell, Bioorg. Med. Chem. Lett. 14 (2004) 3027–3032.
[14] E. Chalkidou, F. Perdih, I. Turel, D.P. Kessissoglou, G. Psomas, J. Inorg. Biochem. 113 (2012) 55–65.
[15] M. Lawal, J.A. Obaleye, R.N. Jadeja, M.O. Bamigboye, V.K. Gupta, H. Roy, I. U. Shaikh, Polyhedron 190 (2020).
[16] C.Y. Chen, Q.Z. Chen, X.F. Wang, M.S. Liu, Y.F. Chen, Transit. Met. Chem. 34 (2009) 757–763.
[17] P. Ruiz, R. Ortiz, L. Perelló, G. Alzuet, M. Gonzalez-Alvarez, M. Liu-González, F. Sanz-Ruiz, J. Inorg. Biochem. 101 (2007) 831–840.
[18] G. Psomas, A. Tarushi, E.K. Efthimiadou, Y. Sanakis, C.P. Raptopoulou, N. Katsaros, J. Inorg. Biochem. 100 (2006) 1764–1773.
[19] E.K. Efthimiadou, Y. Sanakis, M. Katsarou, C.P. Raptopoulou, A. Karaliota, N. Katsaros, G. Psomas, J. Inorg. Biochem. 100 (2006) 1378–1388.
[20] H.C. Neu, Am. J. Med. 82 (1987) 395.
[21] D.E. King, R. Malone, S.H. Lilley, Am. Fam. Physician 619 (2000) 2741–2748.
[22] J.C. Rodriguez, M. Ruiz, A. Climent, G. Royo, Int. J. Antimicob. Agents 17 (2001) 229–231.
[23] A. Tarushi, E. Polatoglou, J. Kljun, I. Turel, G. Psomas, D.P. Kessissoglou, Dalton Trans. 40 (2011) 9461–9473.
[24] O.G. Francis, G.F. Roger, G.W. David, Antibiotic and Chemotherapy, 7th ed., Churchill Living Stone, New York, 1997, pp. 451–469.
[25] F.C. Tenover, Am. J. Med. 119 (2006) S3–S10.
[26] R. Saraiva, S. Lopes, M. Ferreira, F. Novais, E. Pereira, M.J. Feio, P. Gameiro, J. Inorg. Biochem. 104 (2010) 843–850.
[27] G.N. Lipunova, E.V. Nosova, V.N. Charushin, Russ. J. Gen. Chem. 79 (2009) 2753–2766.
[28] M.J. Frisch, G.W. Trucks, H.B.S. Chlegel, G.E. Scuseria, M.A. Robb, J. R. Cheeseman, G. Scalmani, V. Barone, B. Mennucci, G.A. Petersson, et al., Gaussian 09 revision D.01, Gaussian Inc. (2010).
[29] G.M. Sheldrick, SHELXS97 and SHELXL97. University of Göttingen, Germany. ActaCrystallographicaSection E Structure Reports Online ISSN, (1997) 600-5368.
[30] G.M. Sheldrick, Crystal structure refinement with SHELXL, 71 (2015) 3–8.
[31] A. Altomare, G. Cascarano, C. Giacovazzo, A. Guagliardi, J. Appl. Crystallogr., 27 (7771045-1050.
[32] C. K. Johnson, Ortep-II. Report ORNL-5138. Oak Ridge National Laboratory, Oak Ridge, TN, 1976, 37830.
[33] L.J. Farrugia, J. Appl. Crystallogr. 30 (1997) 565.
[34] A.L. Spek, E.E. Van Tamelen, M. Shamma, J. Am. Chem. Soc. (1954) 2315–2317.
[35] M. Nardelli, J. Appl. Crystallogr. 28 (1995) 659.
[36] N.G. Heatley, Biochem. J. 38 (1944) 61–65.
[37] A.D. Becke, J. Chem. Phys. 98 (1993) 5648–5652.
[38] C. Lee, W. Yang, G.R. Parr, Phys. Rev. B. 37 (1988) 785–789.
[39] E. Runge, E.K. Gross, Phys. Rev. B. 52 (1984) 997–1000.
[40] K.E. Riley, B.T. Op'tHolt, K.M. Merz, J. Chem. Theory Comput. 3 (2007) 407–433.
[41] J. Tirado-Rives, W.L. Jorgensen, J. Chem. Theory Comput. 4 (2008) 297–306.
[42] D. Shoba, S. Periandy, M. Karabacak, S. Ramalingam, Spectrochim. Acta A 83 (2011) 540–552.
[43] T. Koopmans, Über die Zuordnung von Wellenfunktionen und Eigenwertenzu den einzelnenElektroneneines Atoms, Physica 1 (1934) 104–113.
[44] R.S. Mulliken, J. Chem. Phys. 2 (1934) 782–793.
[45] R.G. Parr, R.A. Donnelly, M. Levy, W.E. Palke, J. Chem. Phys. 68 (1978) 381–387.
[46] R.G. Parr, L.V. Szentpaly, S. Liu, J. Am. Chem. Soc. 121 (1999) 1922–1924.
[47] R.G. Parr, R.G. Pearson, J. Am. Chem. Soc. 105 (1983) 7512–7516.
[48] W. Yang, R.G. Parr, Proc. Natl. Acad. Sci. 82 (1985) 6723–6726.
[49] L. Coury, Curr. Sep. 18 (1999) 91–96.
[50] G. Psomas, D.P. Kessissoglou, Dalton Trans. 42 (2013) 6252–6276.
[51] K. Nakamoto, Infrared and Raman Spectra of Inorganic and Coordination Compounds, fourth ed., John Wiley, New York, 1986.
[52] C. Dendrinou-Samara, G. Tsotsou, L.V. Ekateriniadou, A.H. Kortsaris, C. P. Raptopoulou, A. Terzis, D.P. Kessissoglou, J. Inorg. Biochem. 71 (1998) 171–179.
[53] G. Manoussakis, C. Bolos, L. Ecateriniadou, C. Sarris, Eur. J. Med. Chem. 22 (1987) 421–425.
[54] W.M.I. Hassan, M.A. Badawy, G.G. Mohamed, H. Moustafa, S. Elramly, Spectrochim. Acta A 111 (2013) 169–177.
[55] J. Coates, Interpretation of infrared spectra, a practical approach. Encyclopedia of analytical chemistry: applications, theory and instrumentation. John Wiley & Sons Ltd, Chichester, 2006, 10815–10837.
[56] M.N. Patel, P.A. Parmar, D.S. Gandhi, Bioorg. Med. Chem. 18 (2010) 1227–1235.
[57] S. Sagdinc, S. Bayarı, J. Mol. Struct. 691 (2004) 107–113.
[58] I. Turel, Coord. Chem. Rev. 232 (2002) 27–47.
[59] E.K. Efthimiadou, Y. Sanakis, M. Katsarou, C.P. Raptopoulou, A. Karaliota, N. Katsaros, G. Psomas, J. Inorg. Biochem. 100 (2006) 1378–1388.
[60] E.K. Efthimiadou, H. Thomadaki, Y. Sanakis, C.P. Raptopoulou, N. Katsaros, A. Scorilas, A. Karaliota, G. Psomas, J. Inorg. Biochem. 101 (2007) 64–73.
[61] M. Múdra, J. Švorec, M. Melník, P. Lönnecke, T. Glowiak, R. Kirmse, Inorg. Chem. Commun. 6 (2003) 1259–1265.
[62] Z. Vasková, N., Kitanovski, N., Jagličić, Z., Strauch, P., Růžičková, Z., Valigura, D., ... and J. Moncol, Polyhedron., 81 (2014) 555-563.
[63] G. Mendoza-Díaz, L.M.R. Martínez-Aguilera, R. Moreno-Esparza, K.H. Pannell, F. Cervantes-Lee, J. Inorg. Biochem., 50 (1993) 65-78.
[64] G. Psomas, C. Dendrinou-Samara, P. Philippakopoulos, V. Tangoulis, C. P. Raptopoulou, E. Samaras, D.P. Kessissoglou, Inorg. Chim. Acta 272 (1998) 24–32.
[65] G. Mendoza-Díaz, L.M.R. Martinez-Aguilera, R. Pérez-Alonso, X. Solans, R. Moreno-Esparza, Inorg. Chim. Acta, 138 (1987) 41–47.
[66] A.W. Addison, T.N. Rao, J. Reedijk, J. van Rijn, G.C. Verschoor, J. Chem. Soc., Dalton Trans. 7 (1984) 1349–1356.
[67] D. Kovala-Demertzi, M. Staninska, I. Garcia-Santos, A. Castineiras, M.A. Demertzis, J. Inorg. Biochem. 105 (2011) 1187–1195.
[68] K. Das, S. Dolai, P. Vojtíšek, S.C. Manna, Polyhedron 149 (2018) 7–16.
[69] B. Hathaway, D.E. Billing, Coord. Chem. Rev. 5 (1970) 143–207.
[70] C. Rajarajeswari, R. Loganathan, M. Palaniandavar, E. Suresh, A. Riyasdeen, M. A. Akbarsha, Dalton Trans. 42 (2013) 8347–8363.
[71] D. Kilveson, J. Phys. Chem. B 101 (1997) 8631–8634.
[72] A.M.F. Benial, V. Ramakrishnan, R. Murugesan, Spectrochim. Acta A 56 (2000) 2775–2781.
[73] A.H. Maki, B.R. McGarvey, J. Chem. Phys. 29 (1958) 31–34.
[74] 74. D.E Fenton, Bio-coordination chemistry, Oxford University Press; 1st Edition, 1996 https://www.amazon.com/Biocoordination-Chemistry-Oxford-Primers/dp/0198557736.
[75] M.K. Bharty, R.K. Dani, S.K. Kushawaha, N.K. Singh, R.N. Kharwar, R.J. Butcher, Polyhedron 88 (2015) 208–221.
[76] V.A. Joseph, J.H. Pandyab, V.K. Gupta, R.N. Jadeja, J. Indian Chem. Soc. 89 (2012) 1455–1464.
[77] J.H. Pandya, R.N. Jadeja, K.J. Ganatra, Saudi Chem. Soc. 18 (2014) 190–199.
[78] U.N. Ekwenye, N.N. Elegalam, Int. J. Mol. Med. Adv. Sci. 1 (2005) 411–417.
[79] P.F. Omojasola, S. Awe, Biosci Res Commun. 16 (2004) 25–28.

[80] M. Melník, Coord. Chem. Rev. 42 (1982) 259–293.
[81] M. Kato, Y. Muto, Coord. Chem. Rev. 92 (1988) 45–83.
[82] A. D. Russell. vknize: Disinfection, Sterilization, and Preservation (Block SS, ed.), kap. 3. Lea &Febiger, Philadelphia, 1991, 27–59.
[83] H.W. Rossmore, In Disinfection, Sterilization and Preservation (Block SS, Ed., 4th ed.) Lea and Febinger: Philadelphia, 1991, 290–321.
[84] K. Fukui, Science, 218 (1982) 747–754.
[85] J.A. Obaleye, A.A. Ajibola, V.B. Bernardus, E.C. Hosten, A. Ozarowski, Inorg. Chim. Acta, 503 (2020) 119404. doi: 10.1016/j.ica.2019.119404.
[86] I. Shaikh, A. Vohra, R. Devkar, R. Jadeja, Eur. J. Chem. 10 (2019) 131-138.

cogent biology

Cogent Biology

Taylor & Francis
Taylor & Francis Group

ISSN: (Print) 2331-2025 (Online) Journal homepage: https://www.tandfonline.com/loi/oabi20

Evaluation of abamectin induced hepatotoxicity in *Oreochromis mossambicus*

Shweta Kushwaha, Isha Anerao, Shweta Rajput, Poonam Bhagriya & Hetal Roy |

To cite this article: Shweta Kushwaha, Isha Anerao, Shweta Rajput, Poonam Bhagriya & Hetal Roy | (2020) Evaluation of abamectin induced hepatotoxicity in *Oreochromis mossambicus*, Cogent Biology, 6:1, 1761277

To link to this article: https://doi.org/10.1080/23312025.2020.1761277

Published online: 13 May 2020.

cogent biology

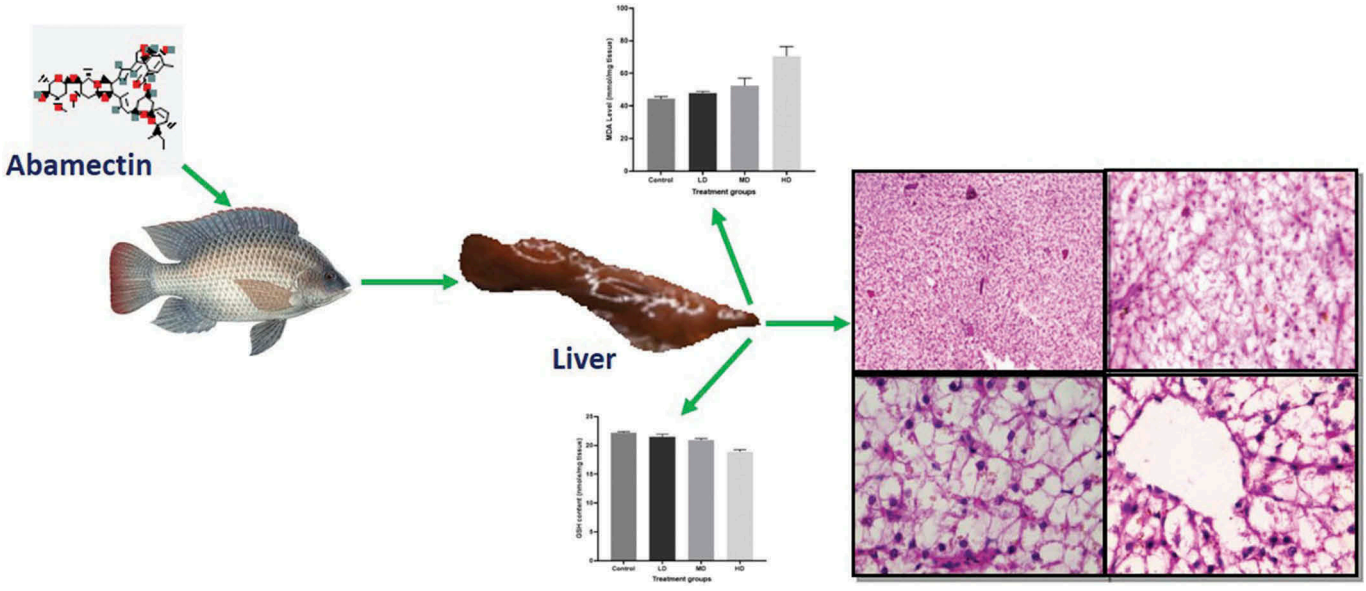

TOXICOLOGY | RESEARCH ARTICLE

Evaluation of abamectin induced hepatotoxicity in *Oreochromis mossambicus*

Shweta Kushwaha, Isha Anerao, Shweta Rajput, Poonam Bhagriya and Hetal Roy

Cogent Biology (2020), 6: 1761277

cogent oa

Kushwaha et al., *Cogent Biology* (2020), 6: 1761277
https://doi.org/10.1080/23312025.2020.1761277

cogent biology

TOXICOLOGY | RESEARCH ARTICLE

Evaluation of abamectin induced hepatotoxicity in *Oreochromis mossambicus*

Shweta Kushwaha[1,2], Isha Anerao[1,3], Shweta Rajput[1], Poonam Bhagriya[1] and Hetal Roy[1*]

Received: 01 March 2020
Accepted: 16 April 2020

*Corresponding author: Hetal Roy, Department of Zoology, Faculty of Science, The Maharaja Sayajirao University of Baroda, Vadodara, Vadodara, Gujarat, India
E-mail: royhetal@yahoo.com

Reviewing editor:
Tianzhu Zang, University of Pennsylvania Perelman School of Medicine, USA

Additional information is available at the end of the article

Abstract: Abamectin (ABM) is a naturally fermented product of *Streptomyces avermitilis*. It is used to control pests in livestock and agriculture. In the present study, it has been hypothesized that intoxication of ABM to *Oreochromis mossambicus* impairs the function of the hepatocyte. Fishes were exposed to ABM with 40, 45, and 55 ppb for 48 h. Test animals were observed at regular intervals of time and sacrificed at the end of the regimen. Liver function tests, oxidative stress parameter, and histopathological alterations were taken into account to analyze hepatotoxicity induced by the test compound. Plasma transaminase activities were increased significantly in all the treated groups. The activity of lipid peroxidation was measured higher due to ABM intoxication, whereas catalase activity was depleted. The marked focal necrotic alteration was examined in liver tissue. The low-dose group showed a less adverse effect on liver, whereas the medium and high dose induced moderate-to-severe hepatotoxicity. Data from this study demonstrate that ABM exposure generates reactive oxygen species (ROS) and alter liver function of fishes, which may lead to liver necrosis. The authors' emphasis on the regulatory use of ABM to protect fish health against ABM-induced toxicological effects.

Subjects: Environmental and Ecological Toxicology; Pesticides toxicity; Hepatotoxicity

Keywords: Abamectin; hepatotoxicity; reactive oxygen species; transaminase; histopathology

1. Introduction

Abamectin (avermectin B1, ABM) is a family of macrocyclic lactones produced by the soil microorganism *Streptomyces avermitilis* and used as a pesticide for crop protection (Abd-Elhady & Abou-Elghar, 2013; Boonstra et al., 2011; Chung et al., 1999). ABM comprises of two active components,

Shweta Kushwaha

ABOUT THE AUTHOR

Research group is interested to observe the effect of abamectin on non-targeted organism. Fish is one of the non-targeted organisms against pesticide. It is known vital organism of food chain therefore fish health is major concern of public health and economic wealth. Usage of any pesticide may alter fish physiology or kill the fishes. Due to its lipophilic nature, abamectin penetrates easily into fish body that leads pathogenesis. Liver is a key organ of biotransformation and detoxification, therefore this study focused to explain the hepatotoxic potential of abamectin on fish.

PUBLIC INTEREST STATEMENT

Abamectin, itself and with combination, shows adverse effects on animal health. The research study has been conducted to confirm abamectin induced adverse effects on fish, one of the food preferences of human. The result of the study authenticated the concentration dependent degradation of fish health and accumulation of abamectin that is ultimately hazardous to human via food chain. Therefore, outcome of present study will facilitate textual support to define policies to use abamectin and its management which curtail environment damage.

avermectin B1a (≥80%) and avermectin B1b (≤20%), which affect insect nervous system by acting on GABAergic neurons (Maioli et al., 2013; Raftery & Volz, 2015). The toxicological properties of ABM are due to these two active components that affect inhibitory synapses via a mode of action involving glutamate-sensitive chloride channels (Yoon et al., 2004). On the scale of toxicity, ABM is classified under class II category of pesticide and used extensively all over the world although ABM is more toxic than ivermectin (Kolar et al., 2008; Mossa et al., 2018).

The intoxication of ABM not only impairs coordination of neurons but also affects the function of hepatocytes and induces liver toxicity (Hsu et al., 2001; Terali et al., 2018; Zanoli et al., 2012). Higher activity of serum aminotransferase was measured in the rat after oral intoxication of ABM (Abd-Elhady & Abou-Elghar, 2013; Hsu et al., 2001; Mossa et al., 2018). The study reports of Kennedy et al. (2014) suggested that ABM exposure alters the fish physiology. Neuronal degeneration and liver dysfunction were the results of ABM exposure to cyprinids fish (Thiripurasundari et al., 2014). Moreover, the accumulation of ABM in liver tissue was confirmed by Howells and Sauer (2001).

Aquatic ecotoxicological research for ABM has become very important since its residue regularly enters the aquatic environment after application on a crop by drift or runoff. The presence of ABM in the aquatic body as well as in fish body (ABM accumulates as it is lipophilic) was quantified for ecotoxicity measure (Novelli et al., 2012). Fish play an important role to maintain the aquatic ecosystem. It is a key organism for the food chain and biomagnifications that is consumed by human also. Fengmei et al. (2011) quantified the presence of avermectin in fish sample that clarify the accumulation of ABM pesticide in fish which is one of the food sources of human. Furthermore, expansion of fish industries suggests increased demands for fish as a source of animal protein. Hence, there is a need for analyzing ABM-induced toxicity in the fish, although it is a non-target organism. Xenobiotic acquisition from any route of exposure comes to the liver for biotransformation as it is primary site of detoxification and facilitated clearance. During high level of metabolism, oxidative stress is generated as well as secondary metabolites make liver possible target of damage (Hong et al., 2016; Lushchak et al., 2018). It is also known that acute liver intoxication is also associated with chronic pesticide exposure which results into irreversible alteration in liver tissue and modulate whole body homeostasis (Wahlang et al., 2013). This study, therefore, aims to evaluate the hepatotoxicity of ABM to provide the first detailed description of liver pathology in *O. mossambicus* during ABM exposure.

2. Material and methods

2.1. Fish maintenance

Oreochromis mossambicus, commonly known as Tilapia (weighing 30 ± 3 gm and 15 ± 2 cm length), used in this study was obtained from the pure brooders. Glass tanks containing 40 l of dechlorinated tap water (temperature 27 ± 4 °C, dissolved oxygen 7.3 ± 0.5 mg/L, pH 7.4) was used. Ten fishes were placed in each tank and then acclimatized to environment for 15 days. The fishes were fed daily with commercial fish pellets equal to 2.5% of their body weight. A commercial formulation of ABM benzoate (Proclaim—5.27% SG, manufactured by Syngenta Agri. Crop Ltd., Batch No. PGSC000002) was purchased from a local distributor. Tilapia was separated into four groups: (1) control (C); (2) low dose (40 ppb, LD); (3) medium dose (45 ppb, MD) and (4) high dose (55 ppb, HD). The fishes were exposed to calculated (1/10th (LD), 1/20th (MD) and 1/30th (HD) concentration of LC50 value of ABM) concentrations of ABM for 48 h under controlled laboratory conditions. At the end of the treatment period, fishes were sacrificed and tissues were collected from each fish for biochemical estimation and analysis of histopathology.

2.2. Behavioral study

At regular interval of time, the behavior of fishes was recorded after ABM exposure to analyze the toxicant induced behavioral changes. Operculum movement, surfacing on water, swimming efficiency, and swimming patterns of tilapia were recorded to analyze the altered behavioral pattern due to ABM exposure.

2.3. Liver function test

Fish blood was collected in K2-EDTA coated tubes. Blood was centrifuged at 3000 rpm for 15 min to separate plasma. Enzyme activity of aspartate transaminase (AST) and alanine transaminase (ALT) were determined at 340 nm using commercially available Reckon diagnostic kit (Bergmeyer et al., 1978). The activity of alkaline phosphatase (ALP) was measured by adopting the protocol of Tietz et al. (1983). 0.5 ml of buffered substrate (0.01 M PNPP in 0.1 M phosphate buffer) and 100 µl of liver supernatant was mixed and incubated for 15 min at room temperature. 0.5 ml of 0.5 N NaOH was added as stopping reagent and intensity of color was measured at 405 nm.

2.4. Biochemical analysis

The liver was homogenized, centrifuged, and the supernatant was collected for biochemical analysis. At 750 nm, total protein was measured using Folin–Ciocalteu's phenol reagent (Lowry et al., 1951). Two hundred microliters of liver homogenate and 500 µl of Lowry reagent (alkaline CuSO4 solution) were incubated for 15 min. Folin phenol reagent (0.5 ml) was added in it and incubated for 5 min at room temperature. Optical density was measured at 750 nm. Direct bilirubin was estimated using Jendrassik and Grof (1938) method using Reckon diagnostic kit. Estimation of glycogen was performed using Seifter et al. (1950) method. Hundred milligrams of tissue digested in boiling KOH and glycogen was precipitated in Ethyl alcohol. Five hundred microliters of aliquot and 2 ml of anthrone reagent were carefully added and heated in boiling water bath for 5 min. The intensity of the green color was read at 620 nm.

2.5. Oxidative stress parameter

Using the method of Buege and Aust (1978), lipid peroxidation product, malondialdehyde (MDA) level was measured by thiobarbituric acid reactive substance (TBARS). In 100 µl of liver homogenate, 200 µl of 8% SDS, 500 µl of 20% acetic acid, 500 µl of 2% thiobarbituric acid (TBA) and 1 ml phosphate buffer were incubated in a water bath at 95°C for 60 min. After cooling, 2 ml of 10% TCA was added and centrifugation at 3000rpm for 10 min, the supernatant was removed and its absorbance was read at 532 nm.

Catalase activity was estimated at 590 nm (Sinha, 1972). Two hundred microliters of liver homogenate and 500 µl of phosphate buffer (0.1 M, pH 7.0) were mixed. At the interval of 15 and 30 s, 0.3 ml H_2O_2 (0.2 M) was added. Dichromate acetic acid reagent (1 ml) was mixed and incubated in boiling water bath for 10 min. Absorbance was recorded at 590 nm.

Reduce Glutathione (GSH) level was measured using Beutler et al. (1963) protocol. This method was based on the development of yellow color when thiol reagent (Elman reagent) 5,5′-dithio-bis -2-nitrobenzoic (DTNB) reacts with GSH present in tissue sample forming 5-thio nitrobenzoic acid (TNB). Intensity of color was measured at 412 nm.

2.6. Histopathology

Liver tissue was collected and fixed in 10% neutral buffered formalin for 24 h. Tissue was dehydrated in an ascending series of ethanol and embedded in paraffin. Sections were cut and stained by hematoxylin-eosin. Slides were examined under light microscope. The degree of tissue changes (DTC) was calculated according to Poleksic & Mitrovic-Tutundzic method (Poleksic & Mitrović-Tutundžić, 1994). The histological alteration was classified based on semi-quantitative estimation of degree of damage with reference to observed histomorphological changes in tissue section (stages I, II, and III). Fewer damage of tissue is classified as stage I in which tissue damage is reversible itself; stage II alterations are more severe and it disturb the homeostasis of tissue. This is reversible up to certain level with treatment. Stage III changes are extremely severe and irreversible. The DTC value in tissue section was calculated by summation of pathological lesions found in each stage and multiplying with the stage using given equation below:

$$\mathrm{DTC} = 10^0 \times \sum(\mathrm{StageI}) + 10^1 \times \sum(\mathrm{StageII}) + 10^2 \times \sum(\mathrm{StageIII})$$

For each group, five tissue sections were observed under the microscope and average DTC value was calculated. These average DTC values were used to evaluate liver damage due to ABM based

on standard classifications given: (1) 0–10 DTC—physiological normal, (2) 11–20 DTC—slightly damaged, (3) 21–50 DTC—moderately damaged, (4) 50–100 DTC—severe damaged, and (5) more than 100 DTC—highly severe and irreversibly damaged.

2.7. Statistical analysis

The statistical analysis of all parameters was performed by one-way analysis of variance (ANOVA) followed by post hoc Dunn–Bonferroni test to determine the significance level with control. Statistical analysis was performed using GraphPad Prism 6 software. The statistical significance was taken to be $p < 0.05$. All the results were expressed as mean ± standard error of the mean (SEM) for each group.

3. Results

3.1. Behavior analysis

Unusual altered behavior of living organisms is one of the clues of impaired physiology and disturbed homeostasis. Stress behavior of fish, due to exposure of xenobiotic can be determined using swimming, feeding, and respiratory (Operculum movement) behaviors. There were no observed change in body movement (swimming) and pigmentation of the control group of fish. One-way ANOVA followed by post hoc Bonferroni comparison of the frequency of operculum movements of treated fishes showed significantly increased movements up to 36 h, after this period operculum movement was decreased at 45 ppb and 55 ppb doses of ABM per minute (Graph 1(A)), whereas nonsignificant increased movement was observed in LD group of fishes. Increased movement of operculum and consistent gulping of air were observed behavioral changes in treated fish that supports induction of hypoxia due ABM exposure. Surfacing behavior of fish is commonly observed when xenobiotics induce the stress by reducing the carrying capacity of O_2. Abnormal behavior like excessive mucus secretion, shedding of scale, loss of pigmentation, loss of balance, restlessness, and swimming on the back were recorded during ABM intoxication. The intensity of altered behavioral activities of the fish was increased with increasing concentration and duration of ABM exposure. However, fishes of the control group maintained normal behavior during 48 h of experiment period.

To observe the swimming efficiency of fishes after ABM exposure, they were released into a channel of 1 m. Swimming patterns and distance travelled by fishes were recorded to observe ABM induced physiological modification. Low and slow stroke of swimming was resulted into significant drop in length travelled by fish per minute due to ABM treatment of MD and HD groups. The difference in distance covered by fishes was increased with an increased exposure period and concentration of ABM (Graph 1(B)). After 24 h of the exposure, frequency to swim on the back was increased in MD and HD group of tilapias. It was also observed that fishes could not maintain body balance during swimming after 36 h of ABM exposure at 55-ppb level. Nonsignificant change was noticed in 40 ppb ABM exposed fishes after 36 h. There was no record of altered behavior of swimming in reference group of tilapias.

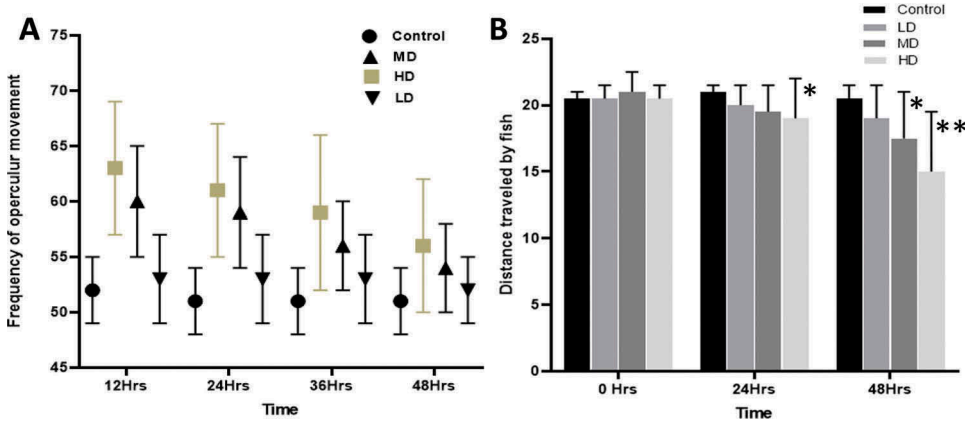

Graph 1. (A) Frequency of opercular movement of *O. mossambicus at different time intervals* after abamectin exposure. (B) Effect of ABM on swimming efficiency of fishes at different time intervals (Frequency was calculated at the interval of 12 h for opercular movement and 24 h for swimming efficiency as mean ± SEM, n = 10).

3.2. Liver function test

To validate ABM-induced hepatic injuries, serum enzymatic activities of ALP, AST, and ALT were estimated. There were no observed changes in mean plasma ALT activity of control and low-dose group of fishes. ALT activity was estimated nonsignificantly higher in the MD group of *O. mossambicus*, whereas the significantly increased activity of ALT was reported in 55 ppb ABM-treated tilapia ($p < 0.05$). Aspartate aminotransferase activity was measured significantly higher when compared to the HD groups ($p < 0.01$) of fishes with experimental control group. There was nonsignificant higher activity of AST measured at 45-ppb treatment, whereas no change of activity was recorded after 40-ppb exposure of ABM to tilapias (Table 1). The AST/ALT ratio was <1.0 in the high-dose group of *O. mossambicus* that indicates the fibrotic insult of liver tissue. ALP activity was nonsignificantly elevated in fishes that were exposed to 40 ppb and 45 ppb of ABM for 48 h as compared to that of the reference group of tilapias. However, test organisms of high dose group showed a statistically significant increase in the activity of ALP due to biliary obstruction generated by ABM exposure (Table 1, Figure 2(b)).

Table 1. Effect of abamectin on liver marker enzymes after 48 h of intoxication on *O. mossambicus*

Enzymes	Control	LD	MD	HD
ALT (IU/L)	10.66 ± 0.03	10.75 ± 0.06	10.9 ± 0.1	11.08 ± 0.14*
AST (IU/L)	10.4 ± 0.34	10.79 ± 0.49	11.09 ± 0.3	13.19 ± 0.39**
ALP (μmolPNP released/min)	42.43 ± 3.21	52.63 ± 4.05	58.63 ± 5.56	74.57 ± 5.76**

(Data values are shown as mean ± SEM. One-way analysis of variance was followed by post hoc Dunn–Bonferroni test with control at: * = $p < 0.05$; ** = $p < 0.01$).

3.3. Biochemical test

There were no significant changes found in total protein levels in low toxicant exposed fish. The quantified level of protein in mid- and high-dose groups was measured significantly low after 48 h of ABM treatment (Table 2). Majority of serum proteins are synthesized in the liver; therefore, the altered level of total protein is an indicator of liver function impairment. On the contrary, the test organism from mid- and high-dose groups showed a significant decrease in glycogen level ($p < 0.05$ and $p < 0.01$, respectively), whereas low-dose group showed unremarkable depletion in the level of glycogen after ABM intoxication as compared to control fishes (Table 2). There were no significant changes in the total bilirubin levels in LD and MD groups of ABM-exposed tilapia as compared to the value obtained from the control fishes. The significantly higher level of bilirubin was estimated on 55 ppb intoxication of ABM to fishes.

Table 2. Biochemical alteration due to 48 h of abamectin exposure to *O. mossambicus*

Bio-molecules	Control	LD	MD	HD
Protein (mg/gm tissue)	18.28 ± 0.51	16.85 ± 0.75	14.58 ± 0.90*	12.67 ± 0.75**
Glycogen (mg/gm tissue)	37.97 ± 0.58	32.7 ± 2.0	29.9 ± 1.1*	26.27 ± 2.06**
Bilirubin (mg/dL)	0.72 ± 0.01	0.77 ± 0.03	0.79 ± 0.03	0.89 ± 0.06*

Values are shown as mean ± SEM, n = 10; * = $p < 0.05$; ** = $p < 0.01$.

3.4. Oxidative stress parameters

The effects of ABM on certain oxidative stress parameters are summarized in Graph 2. Treated groups of *O. mossambicus*, LD, MD, and HD, exhibited an increase in the level of MDA that indirectly shows higher the activity of LPO (Graph 2(A)). The MDA levels in the liver tissues of fish exposed to higher concentration of ABM were significantly higher than those in the control ($p < 0.01$). However, the MD and HD treatment of ABM to tilapias depleted the activity of catalase significantly when compared to the control group (Graph 2(B)). Data also show a significant decrease in catalase activity of hepatocytes observed in the fishes of MD and HD groups, whereas 40-ppb treatment of ABM did not result in a significant change in catalase activity compared to the control fishes. Graph 2(C) shows the effects of ABM on reduced glutathione content in liver tissues from the fishes of ABM treated groups. Reduced glutathione content in the liver was significantly decreased ($p < 0.005$) in the HD group of fishes as compared to the value obtained from the control tilapias. Nonsignificant depletion of GSH level was recorded in 40 ppb and 45 ppb ABM-intoxicated groups of tilapias.

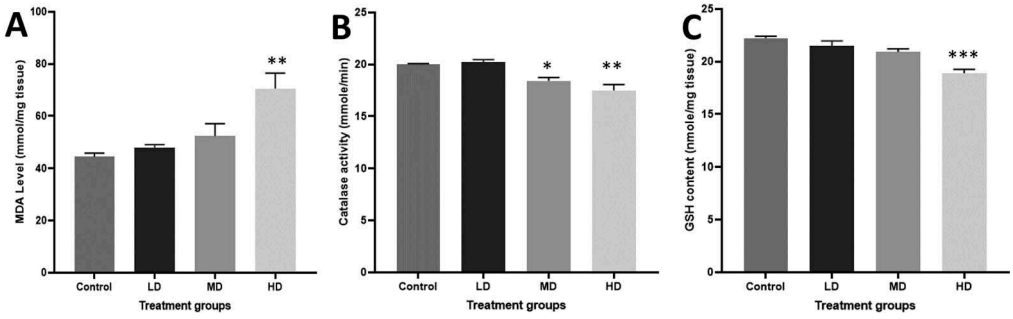

Graph 2. Effect of abamectin on oxidative stress parameters of liver after 48 h intoxication to tilapias. (A) Alteration in MDA level in hepatic tissue of fishes; (B) modulation in catalase activity after ABM treatment; (C) GSH level in liver tissue of tilapias (each value is the mean ±SEM, n = 10, * = p < 0.05; ** = p < 0.01; *** = p < 0.005).

3.5. Histopathology

Common pathological alteration found in the liver tissue was centrilobular destruction, vacuolar degeneration, dilation of sinusoid, fibrosis, and bile stagnation. Histology of control fish liver (Figure 1(a,b)) shown a regular arrangement of hepatocytes in glandular pattern with an intact central vein. The hepatic histopathology of a low dose group of fishes showed sinusoid dilation due to ABM exposure (Figure 1(c)). On 45 ppb exposure of ABM to tilapia induced vacuolar degeneration of hepatocytes. Sinusoid dilation was also a commonly observed feature at a medium dose of ABM exposure (Figure 1(d)). Liver fibrosis was commonly observed histoarchitectural damage of high dose group of test organism. Centrilobular destruction and bile stagnation were marked identified histopathological alteration on 55 ppb intoxication of ABM (Figure 2(b,d)). Bile stagnation was observed as yellow-brown patches in hepatic tissue. Observed hepatic alteration of the HD group was severe and irreversible. Calculated DTC value was 53.18 for 45 ppb ABM exposure, whereas at 55 ppb ABM exposure, DTC value was raised on 139.6 in comparison to control hepatic tissue). DTC value above 100 indicates irreversible damage to the liver (Graph 3).

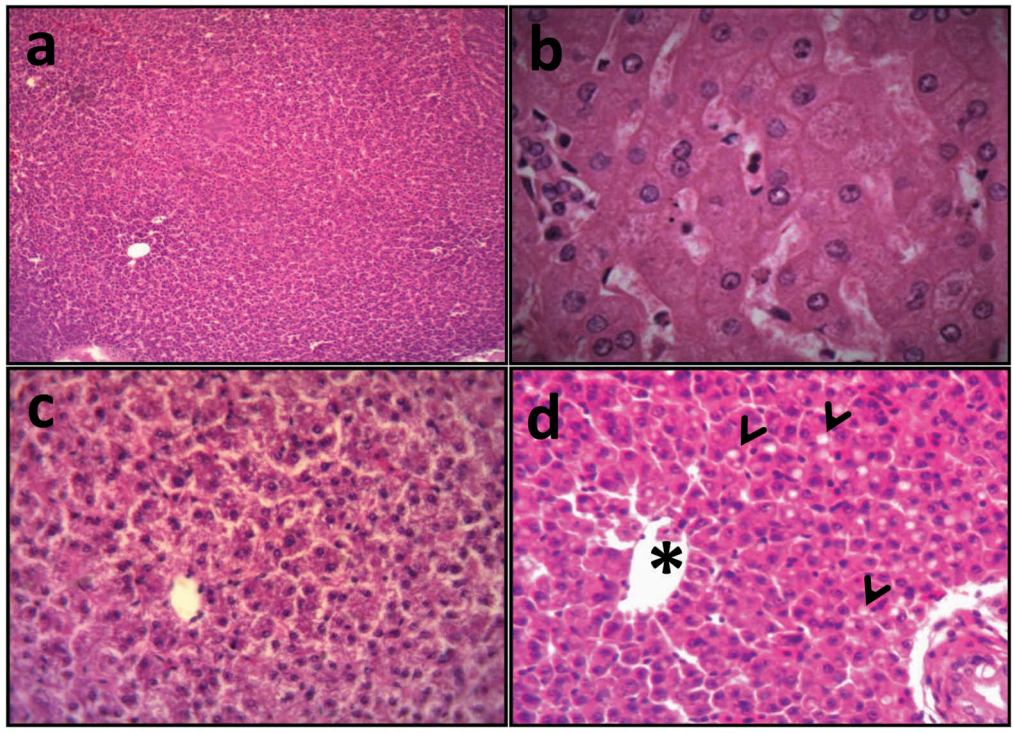

Figure 1. Photomicrograph of Liver histology of *O. mossambicus* (a) control fish liver histoarchitecture 4X; (b) control hepatic section 45X; (c) 40 ppb ABM-treated liver histopathology of tilapia with mild sinusoid dilation, 10X; (d) sinusoid dilation after 45 ppb ABM intoxication to fishes 10X, * shows centrilobular destruction and arrow shows vacuolar degeneration).

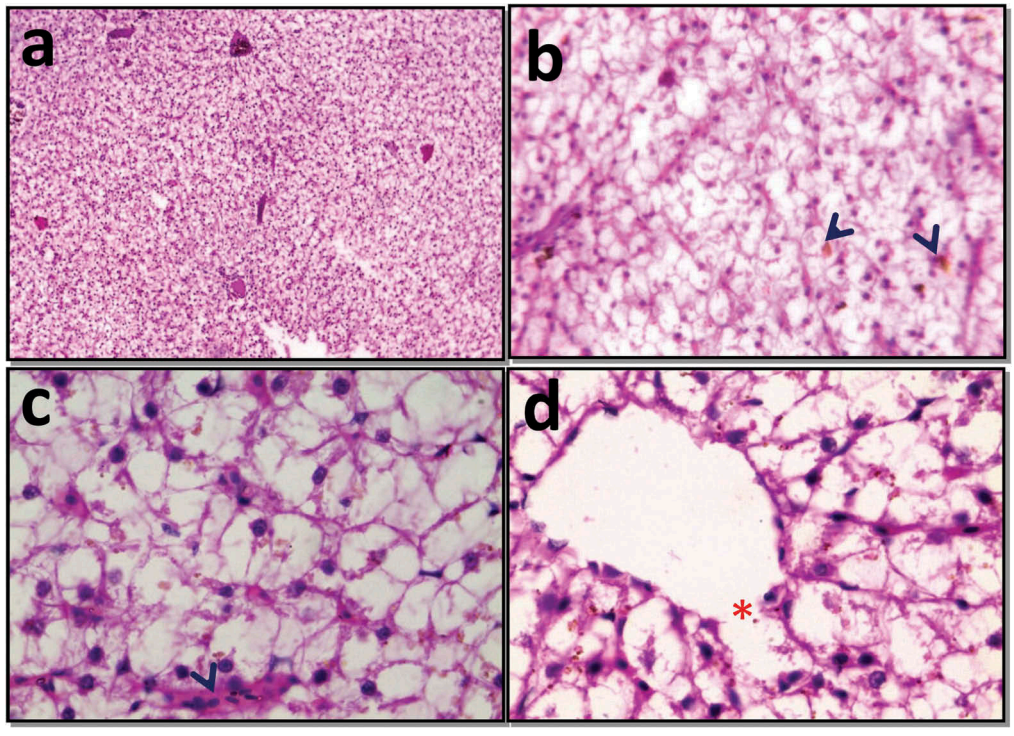

Figure 2. Photomicrograph of histopathological of hepatic tissue after 55 ppb exposure of ABM. (a) Histological damage of liver, 4X; (b) bile stagnation (arrow) and necrosis with gross hepatocellular damage, 10X; (c) Kupffer cell proliferation (arrow), 45X; (d) centrilobular destruction (*) and gross necrosis, 45X).

Graph 3. Shows degree of tissue change at 40, 45, and 50 ppb of ABM exposure to tilapia after 48 h.

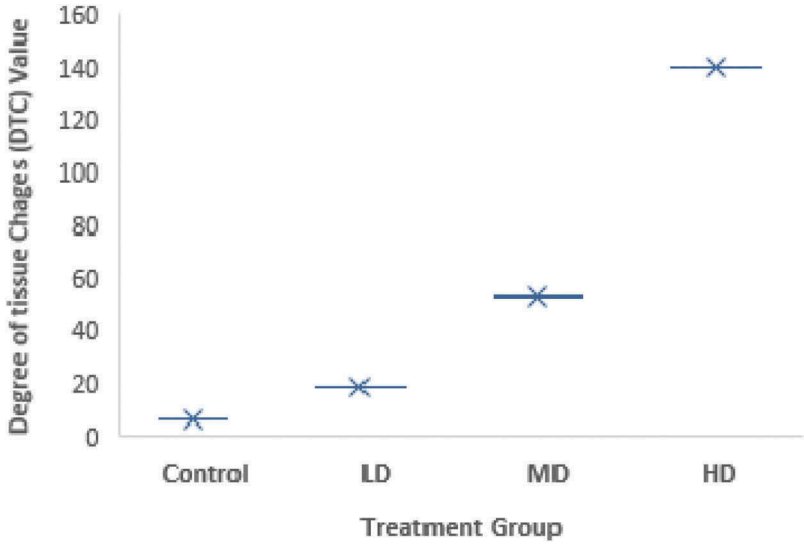

4. Discussion

Alteration in behavior patterns is one of the most sensitive indicators of environmental stress (Byrne & O'halloran, 2001). The behavior parameter provides the information of external (morphological) and internal (physiological) adaptive changes of an organism due to the insult of any chemical (Legradi et al., 2018). The increased opercular movement of gills, surfacing, and gulping was observed after ABM exposure. Increased surfacing and gulping during exposure periods of ABM suggests an elevated rate of metabolism and altered physiology of fish due to hypoxia. Hypoxia triggers numerous potential detrimental metabolic disturbances in fish because aerobic metabolism gradually becomes more compromised as oxygen levels decreases, which results into loss of appetite, growth, and locomotory activity (Oldham et al., 2019). In the state of hypoxia, fishes struggled to meet the oxygen demands required to maintain basal homeostasis, making them acidotic from anaerobic metabolism that eventually damage the tissue or become fatal to fishes (Hvas & Oppedal, 2019). Exposures of fishes to different concentrations of ABM-altered swimming pattern and impaired movement (Ballesteros et al., 2009; Gormley & Teather, 2003; Pereira et al., 2012). In current study, increased mucus secretion in treated fishes was due to nonspecific adaptive response against ABM which provides additional protection against irritation or form barrier between body and pesticide so absorption of pesticide decreases (Saleh et al., 2019).

The nervous system controls muscle movement by the neurotransmitter. The inhibition of the neurotransmitter by ABM may affect swimming pattern and equilibrium of body of tilapia (Bretaud et al., 2000; Golombieski et al., 2008; Varo et al., 2003). Our results show that fish exposed to ABM during 48 h exhibit decreased swimming speed and movement percentage with respect to the reference group. The drop of locomotor activity as adaptive phenomenon is called Hypoactivity Syndrome. Lowered swimming activity in fishes could be adaptive response to restrain energy against higher metabolism of biotransformation (Ballesteros et al., 2009; Cazenave et al., 2008). ABM induces neurotoxicity by activation of GABA-gated chloride channels and develops hypoactivity of muscle; moreover, consistent exposure of ABM persuades paralyzing effect to organism (Dawson et al., 2000; Novelli et al., 2012; Raftery & Volz, 2015; Xu et al., 2017). Decline travel distance in treated group was attribution of GABAergic inhibition. ABM is designed to control the pest through GABA-gated chloride flux disrupt to seize the movement (Casida, 1993). Due to this mechanical action of ABM, swimming activity and balancing of body was modulated after treatment.

Liver function tests are important to evaluate liver physiology on the exposure of pesticides. Hence, activities of serum ALT and AST have been routinely used to assess alter fish physiology as well as for the detection of tissue damage by pesticide exposure (McGill, 2016; Rao, 2006). The present results showed that the treatment of ABM to fish caused a significant increase in the plasma activities of AST and ALT when compared to the control fish. An increased activity of these enzymes in serum is a sensitive indicator of cellular damage (Fırat et al., 2011; Jee et al., 2005; Palanivelu et al., 2005). Elevated liver enzyme activity in serum indicates stress-based tissue impairment, degenerative changes and hepatic hypofunction as the effects of the toxicant on hepatocytes induce to release cellular enzymes into blood. A high level of liver specific enzyme activity in serum is one of the indicators of necrosis which could be result of hypoxia-induced ABM exposure and elevation of ROS due to biotransformation.

Elevated activity of LPO is in support of the production of hydroxyl radicals that causes oxidative damage to hepatocyte. The present study recorded significant increased MDA level in HD group of fishes. Lipid peroxidase peroxides the lipid of the plasma membrane and makes the membrane leaky which escorts the necrotic event (Zambo et al., 2013). Thus, elevated level of hepatocyte specific enzymes ALT and AST activities were recorded higher in serum. Ogueji et al. (2020) reported depletion in antioxidant level and increased hepatic LPO and ROS levels in *Clarias gariepinus* exposed to acute concentrations of ivermectin.

There was a negative correlation with catalase activity and GSH level due to ABM exposure. Catalase removes H_2O_2 by converting it into O_2 and H_2O and protects the cell. Present study showed lower the activity of catalase on ABM exposure. A low level of GSH was observed in the treated group during experiment. GSH involved in elimination of H_2O_2.Therefore, reduction in GSH level and catalase activity directly escort overproduction of H_2O_2 that enhance the activity of LPO that supports our results. Notably reduction in GSH level was observed in the liver tissue of *O. mossambicus* after 96 h of ABM exposure (Al Ghais et al., 2019). Juliana et al. (2018) have shown that ABM exposure perturbs mitochondrial bioenergetics and participate in the mitochondrial dependent pathological event via a reduction in GSH level and elevation of ROS.

The present results demonstrate a significant decrease in the mean level of serum proteins with increase in the dose of ABM and developed hypoproteinemia. The results indicate that ABM caused alterations in the protein metabolism of fish. Low content of protein level may be due to increased proteolytic activity to compensate pesticide metabolic stress or ABM treatment may be attributed to impairment in protein synthesis (Bradbury et al., 1987; Mastan & Rammayya, 2010). Depletion of protein content may be attributed to cell damage by ABM treatment and consequent inability of cell to synthesize protein or protein may be utilize for alternative source of energy for repair of the damaged cells caused by ABM intoxication (Al-Kahtani, 2011; Thanosmit, 2016). Hypoproteinemia is a result of the high requirement of glucose to compensate stress and homeostasis which may be balanced by gluconeogenesis from protein. Observed low level of glycogen is in support with resultant hypoproteinemia due to ABM exposure. Known metabolic response of fish to toxic effects is elevation in blood glucose level which is produced by lysis of glycogen. Hence, the level of glycogen was reported low (Luskova et al., 2002; Ogueji et al., 2020) To After 48 h of treatment of ABM, direct bilirubin level was measured high due to the disruption of hepatic architecture or altered hemoglobin breakdown. Measured higher activity of ALP in serum of ABM treated fishes is in patronage with elevated level of bilirubin.

The elevation of ALT, AST, and MDA level and induction of hypoxia in the present study suggest probable liver damage due to ABM exposure. The damage alters the histoarchitecture of tissue that can be seen in the histopathological lesions. Marked degenerative changes like vacuolar degeneration, centrilobular degeneration, and fibrosis were noticed in the liver of treated fish. After ABM exposure to fish, a reduction in antioxidant enzyme might occur due to the overproduction of free radicals that hamper the defense mechanism of hepatocyte and leads necrosis. Bile stagnation was reported during histopathological analysis that is in support of increased

activity of alkaline phosphatase. Repeated administration of avermectin causes significant histopathological alteration in liver tissues. Necrotic changes were observed in hepatocyte of rat on avermectin exposure (Ahmed et al., 2020). Cellular degeneration and atrophy of liver tissue indicated the direct toxicosis of ABM due to oxidative stress generated on ABM exposure.

5. Conclusion

In summary, the present results demonstrated that intoxication of ABM negatively affects fish physiology. Exposure to ABM, change the swimming behavior of tilapias and induce hypoxia which can be fatal for fish survival. Dose dependent altered liver physiology was observed on 48 h of ABM exposure. ABM intoxication impaired hepatic function of fishes by inducing oxidative stress and modulate antioxidant enzymes. Forty-eight hours of ABM treatment alters the activity of liver marker enzymes (ALT, AST, and ALP). Severe histoarchitectural damage was also observed in hepatic tissue. Hepatic necrosis suggests that ABM is potential toxic to tilapias which develops toxicological manifestation and impaired fish health. Hence, ABM must be used with utmost caution.

Abbreviation

ABM	Abamectin
ppb	Parts per billion
ALT	Alanine transaminase
AST	Aspartate transaminase
ALP	Alkaline Phosphatase
ROS	Reactive oxygen species
PBS	Phosphate buffer saline
LPO	Lipid peroxidation
MDA	Malondialdehyde
TBA	Thiobarbituric acid
TBARS	Thiobarbituric acid reactive substance
PNPP	4 -Nitro phenyl phosphate
SEM	Standard error of the mean

Funding
The authors received no funding for present research. It is a self-funded research.

Competing interest
The authors declare that they have no conflict of interest.

Author details
Shweta Kushwaha[1,2]
E-mail: shweta.r.kushwaha@gmail.com
Isha Anerao[1,3]
E-mail: ishaanerao@gmail.com
Shweta Rajput[1]
E-mail: shwetarajput9427@gmail.com
Poonam Bhagriya[1]
E-mail: bhagriya.poonam@gmail.com
Hetal Roy[1]
E-mail: royhetal@yahoo.com
[1] Department of Zoology, Faculty of Science, The Maharaja Sayajirao University of Baroda, Vadodara, Gujarat, India.
[2] Department of Toxicology, JDM Research, Vadodara, Gujarat, India.
[3] Department of Biological Sciences and Bioengineering, Indian Institute of Technology, Kanpur, India.

Compliance with ethical standards
The research carried out was in accordance with the guidelines of APHA-AWWA-WEF (1998).

Citation information
Cite this article as: Evaluation of abamectin induced hepatotoxicity in *Oreochromis mossambicus*, Shweta Kushwaha, Isha Anerao, Shweta Rajput, Poonam Bhagriya & Hetal Roy, *Cogent Biology* (2020), 6: 1761277.

Graphical abstract
Source: Author.

References

Abd-Elhady, H. K., & Abou-Elghar, G. E. (2013). Abamectin induced biochemical and histopathological changes in the albino rat, *Rattus norvegicus*. *Journal of Plant Protection Research*, *53*(3), 263–270. https://doi.org/10.2478/jppr-2013-0039

Ahmed, E. A., Mohammed, A. A., Atef, M. K., Ali, S. A., Ashraf, A. E., Serag, E. I. E., Ahmed, A. A., Morsy, K. S., Alshehri, M. A., El-Mekkawy, H. I., Elmansi, A. A., & Alfaifi, A. E. (2020). Co-administration of vitamin E and selenium in vivo and in vitro ameliorates the toxic effects caused by ivermection and doramectin. *Veterinarni medicina*, *65*(2), 71–83. https://doi.org/10.17221/74/2019-VETMED

Al Ghais, S. M., Varadharajulu, S., & Kumbhar, P. (2019). Effects of Abamectin on Tilapia mossambica peters changes in reduced glutathione (GSH) and protein content. *International Journal of Fisheries and Aquatic Studies*, *7*(4), 280–284.http://www.fisheriesjournal.com/archives/2019/vol7issue4/PartD/7-4-9-917.pdf

Al-Kahtani, M. A. (2011). Effect of an insecticide abamectin on some biochemical characteristics of Tilapia fish (*Oreochromis niloticus*). *American Journal of Agricultural and Biological Sciences*, *6*(1), 62–68. https://doi.org/10.3844/ajabssp.2011.62.68

Ballesteros, M. L., Durando, P. E., Nores, M. L., Díaz, M. P., Bistoni, M. A., & Wunderlin, D. A. (2009). Endosulfan induces changes in spontaneous swimming activity and acetylcholinesterase activity of *Jenynsia multidentata* (Anablepidae, Cyprinodontiformes). *Environmental Pollution*, *157*(5), 1573–1580. https://doi.org/10.1016/j.envpol.2009.01.001

Bergmeyer, H. U., Horder, M., & Moss, D. W. (1978). Provisional recommendations on IFCC methods for the measurement of catalytic concentrations of enzymes. Part 2. Revised IFCC method for aspartate aminotransferase. *Clinical Chemistry*, *24*(4), 720–721. https://doi.org/10.1093/clinchem/24.4.720

Beutler, E., DURON, O., & KELLY, B. M. (1963). Improved method for the determination of blood glutathione. *Journal of Laboratory and Clinical Medicine*, *61*, 882–888.

Boonstra, H., Reichman, E. P., & Van den Brink, P. J. (2011). Effects of the veterinary pharmaceutical ivermectin in indoor aquatic microcosms. *Archives of Environmental Contamination and Toxicology*, *60*(1), 77–89. https://doi.org/10.1007/s00244-010-9526-1

Bradbury, S. P., McKim, J. M., & Coats, J. R. (1987). Physiological response of rainbow trout (*Salmo gairdneri*) to acute fenvalerate intoxication. *Pesticide Biochemistry and Physiology*, *27*(3), 275–288. https://doi.org/10.1016/0048-3575(87)90057-5

Bretaud, S., Toutant, J. P., & Saglio, P. (2000). Effects of carbofuran, diuron, and nicosulfuron on acetylcholinesterase activity in goldfish (*Carassius auratus*). *Ecotoxicology and Environmental Safety*, *47*(2), 117–124. https://doi.org/10.1006/eesa.2000.1954

Buege, J. A., & Aust, S. D. (1978). Microsomal lipid peroxidation. *Methods in enzymology, 52, 302-310.* https://doi.org/10.1016/S0076-6879(78)52032-6 .

Byrne, P. A., & O'halloran, J. (2001). The role of bivalve molluscs as tools in estuarine sediment toxicity testing: A review. *Hydrobiologia*, *465*(1–3), 209–217. https://doi.org/10.1023/A:1014584607501

Casida, J. E. (1993). Insecticide action at the GABA-gated chloride channel: Recognition, progress, and prospects. *Archives of Insect Biochemistry and Physiology*, *22*(1-2), 13–23. https://doi.org/10.1002/arch.940220104

Cazenave, J., Nores, M. L., Miceli, M., Dıaz, M. P., Wunderlin, D. A., & Bistoni, M. A. (2008). Changes in the swimming activity and the glutathione S-transferase activity of Jenynsia multidentata fed with microcystin-RR. *Water Research*, *42*(4–5), 1299–1307. https://doi.org/10.1016/j.watres.2007.09.025

Chung, K., Yang, C. C., Wu, M. L., Deng, J. F., & Tsai, W. J. (1999). Agricultural avermectins: An uncommon but potentially fatal cause of pesticide poisoning. *Annals of Emergency Medicine*, *34*(1), 51–57. https://doi.org/10.1016/S0196-0644(99)70271-4

Dawson, G. R., Wafford, K. A., Smith, A., Marshall, G. R., Bayley, P. J., Schaeffer, J. M., … McKernan, R. M. (2000). Anticonvulsant and adverse effects of avermectin analogs in mice are mediated through the γ-aminobutyric acid receptor. *Journal of Pharmacology and Experimental Therapeutics*, *295*(3), 1051–1060. http://jpet.aspetjournals.org/content/295/3/1051.short

Fengmei, W., Junhui, C., Hongyan, C., Zhixu, T., Gang, Z., Zengyuan, N., Shiping, P., Xiaoru, W., & Frank, S. C. L. (2011). Multi-residue method for the confirmation of four avermectin residues in food products of animal origin by ultra-performance liquid chromatography–tandem mass spectrometry. *Food Additives & Contaminants: Part A*, *28*(5), 627–639. https://doi.org/10.1080/19440049.2011.563367

Fırat, O., Cogun, H. Y., Yüzereroğlu, T. A., Gök, G., Fırat, Ö., Kargin, F., & Kötemen, Y. (2011). A comparative study on the effects of a pesticide (cypermethrin) and two metals (copper, lead) to serum biochemistry of Nile tilapia, *Oreochromis niloticus*. *Fish Physiology and Biochemistry*, *37*(3), 657–666. https://doi.org/10.1007/s10695-011-9466-3

Golombieski, J. I., Marchesan, E., Camargo, E. R., Salbego, J., Baumart, J. S., Loro, V. L., Machado, S. L. D. O., Zanella, R., & Baldisserotto, B. (2008). Acetylcholinesterase enzyme activity in carp brain and muscle after acute exposure to diafuran. *Scientia Agricola*, *65*(4), 340–345. https://doi.org/10.1590/S0103-90162008000400003

Gormley, K. L., & Teather, K. L. (2003). Developmental, behavioral, and reproductive effects experienced by Japanese medaka (*Oryzias latipes*) in response to short-term exposure to endosulfan. *Ecotoxicology and Environmental Safety*, *54*(3), 330–338. https://doi.org/10.1016/S0147-6513(02)00005-2

Hong, N. P., Le, S. H., & Van, T. P. (2016). Hepatoprotective activity of *Ganoderma lucidium* (Curtis) P. Karst against cyclophosphamide-induced liver injury in mice. *Cogent Biology*, *2*(1), 1267421.https://doi.org/10.1080/23312025.2016.1267421

Howells, L., & Sauer, M. J. (2001). Multi-residue analysis of avermectins and moxidectin by ion-trap LC-MSn© Crown copyright. *The Analyst*, *126*(2), 155–160. https://doi.org/10.1039/b008305o

Hsu, D. Z., Hsu, C. H., Huang, B. M., & Liu, M. Y. (2001). Abamectin effects on aspartate aminotransferase and nitric oxide in rats. *Toxicology*, *165*(2–3), 189–193. https://doi.org/10.1016/S0300-483X(01)00434-6

Hvas, M., & Oppedal, F. (2019). Physiological responses of farmed Atlantic salmon and two cohabitant species of cleaner fish to progressive hypoxia. *Aquaculture*, *512*, 734353. https://doi.org/10.1016/j.aquaculture.2019.734353

Jee, J. H., Masroor, F., & Kang, J. C. (2005). Responses of cypermethrin-induced stress in haematological parameters of Korean rockfish, *Sebastes schlegelii* (Hilgendorf). *Aquaculture Research*, *36*(9), 898–905. https://doi.org/10.1111/j.1365-2109.2005.01299.x

Jendrassik, L., & Grof, P. (1938). Colorimetric method of determination of bilirubin. *Biochemische Zeitschrift*, *27*, 81–82.

Juliana, C., Susana, G. L., Cal, G. B., Juba, A., O'Brien, S., Jun, C. H., & Buhlman, L. M. (2018). Vulnerable parkin loss of function *Drosophila* dopaminergic neurons have advanced mitochondrial aging, mitochondrial network loss and transiently reduced autophagosome recruitment. *Frontier in Cellular Neuroscience*, *12*, 39. https://doi.org/10.3389/fncel.2018.00039

Kennedy, C. J., Tierney, K. B., & Mittelstadt, M. (2014). Inhibition of P-glycoprotein in the blood–brain barrier alters avermectin neurotoxicity and swimming performance in rainbow trout. *Aquatic Toxicology*, *146*, 176–185. https://doi.org/10.1016/j.aquatox.2013.10.035

Kolar, L., Eržen, N. K., Hogerwerf, L., & van Gestel, C. A. (2008). Toxicity of abamectin and doramectin to soil invertebrates. *Environmental Pollution*, *151*(1), 182–189. https://doi.org/10.1016/j.envpol.2007.02.011

Legradi, J. B., Di Paolo, C., Kraak, M. H. S., Van der Geest, H. G., Schymanski, E. L., Williams, A. J., Dingemans, M. M., Massei, R., Brack, W., Cousin, X., & Begout, M. L. (2018). An ecotoxicological view on neurotoxicity assessment. *Environmental Sciences Europe*, *30*(1), 46.

Lowry, O. H., Rosebrough, N. J., Farr, A. L., & Randall, R. J. (1951). Protein measurement with the Folin phenol reagent. *Journal of Biological Chemistry*, *193*(1), 265–275.https://www.jbc.org/content/193/1/265.long

Lushchak, V. I., Matviishyn, T. M., Husak, V. V., Storey, J. M., & Storey, K. B. (2018). Pesticie toxicity: A mechanistic approach. *EXCLI Journal: Experimental and Clinical Sciences*, *17*, 1101–1136.http://dx.doi.org/10.17179/excli2018-1710

Luskova, V., Svoboda, M., & Kolarova, J. (2002). Effect of diazinon on blood plasma biochemistry in Carp

(*Cyprinus carpio L.*). *Acta Veterinaria Brno*, *71*(1), 117–123. https://doi.org/10.2754/avb200271010117

Maioli, M. A., De Medeiros, H. C., Guelfi, M., Trinca, V., Pereira, F. T., & Mingatto, F. E. (2013). The role of mitochondria and biotransformation in abamectin-induced cytotoxicity in isolated rat hepatocytes. *Toxicology In Vitro*, *27*(2), 570–579. https://doi.org/10.1016/j.tiv.2012.10.017

Mastan, S. A., & Rammayya, P. J. (2010). Biochemical profile of *Channa gachua* (Ham) exposed to sublethal doses of Dichlorovas (DDVP). *The Internet Journal of Toxicology*, *8(1)*, 27–32.https://print.ispub.com/api/0/ispub-article/11029

McGill, M. R. (2016). The past and present of serum aminotransferases and the future of liver injury biomarkers. *EXCLI Journal*, *15*, 817–828. https://doi.org/10.17179/excli2016-800

Mossa, A. T. H., Mohafrash, S. M., & Chandrasekaran, N. (2018). Safety of natural insecticides: Toxic effects on experimental animals. *Biomedical Research International*, *2018*, 4308054. https://doi.org/10.1155/2018/4308054

Novelli, A., Vieira, B. H., Cordeiro, D., Cappelini, L. T. D., Vieira, E. M., & Espíndola, E. L. G. (2012). Lethal effects of abamectin on the aquatic organisms *Daphnia similis, Chironomus xanthus* and *Danio rerio*. *Chemosphere*, *86*(1), 36–40. https://doi.org/10.1016/j.chemosphere.2011.08.047

Ogueji, E., Nwani, C., Mbah, C., Iheanacho, S., & Nweke, F. (2020). Oxidative stress, biochemical, lipid peroxidation, and antioxidant responses in Clarias gariepinus exposed to acute concentrations of ivermectin. *Environmental Science and Pollution Research*,27, 16806-16815. https://doi.org/10.1007/s11356-019-07035-4

Oldham, T., Nowak, B., Hvas, M., & Oppedal, F. (2019). Metabolic and functional impacts of hypoxia vary with size in Atlantic salmon. *Comparative Biochemistry and Physiology Part A: Molecular & Integrative Physiology*, *231*, 30–38. https://doi.org/10.1016/j.cbpa.2019.01.012

Palanivelu, V., Vijayavel, K., Balasubramanian, S. E., & Balasubramanian, M. P. (2005). Influence of insecticidal derivative (cartap hydrochloride) from the marine polycheate on certain enzyme systems of the fresh water fish *Oreochromis mossambicus*. *Journal of Environmental Biology*, *26*(2), 191–195.

Pereira, V. M., Bortolotto, J. W., Kist, L. W., De Azevedo, M. B., Fritsch, R. S., Da Luz Oliveira, R., Pereira, T. C. B., Bonan, C. D., Vianna, M. R., & Bogo, M. R. (2012). Endosulfan exposure inhibits brain AChE activity and impairs swimming performance in adult zebrafish (*Danio rerio*). *Neurotoxicology*, *33*(3), 469–475. https://doi.org/10.1016/j.neuro.2012.03.005

Poleksic, V., & Mitrović-Tutundžić, V. (1994). Fish gills as a monitor of sublethal and chronic effects of pollution. In: R. Muller, and R. Lloyd, ed. Sublethal and chronic effects of pollutants on freshwater fish.. Fishing News Books Ltd., Farnham, 339-352.

Raftery, T. D., & Volz, D. C. (2015). Abamectin induces rapid and reversible hypoactivity within early zebrafish embryos. *Neurotoxicology and Teratology*, *49*, 10–18. https://doi.org/10.1016/j.ntt.2015.02.006

Rao, J. V. (2006). Toxic effects of novel organophosphorus insecticide (RPR-V) on certain biochemical parameters of euryhaline fish, *Oreochromis mossambicus*. *Pesticide Biochemistry and Physiology*, *86*(2), 78–84. https://doi.org/10.1016/j.pestbp.2006.01.008

Saleh, M., Kumar, G., Abdel-Baki, A. A. S., Dkhil, M. A., El-Matbouli, M., & Al-Quraishy, S. (2019). Quantitative proteomic profiling of immune responses to *Ichthyophthirius multifiliis* in common carp skin mucus. *Fish & Shellfish Immunology*, *84*, 834–842. https://doi.org/10.1016/j.fsi.2018.10.078

Seifter, S., Dayton, S., Novic, B., & Muntwyler, E. (1950). The estimation of glycogen with the anthrone reagent. *Archives of Biochemistry and Biophysics*, *25*,(1) 191–200.

Sinha, A. K. (1972). Colorimetric assay of catalase. *Analytical Biochemistry*, *47*(2), 389–394. https://doi.org/10.1016/0003-2697(72)90132-7

Terali, K., Dalmizrak, O., Hoti, Q., & Ozer, N. (2018). Evaluation of the inhibitory effect of abamectin on mammalian butyrylcholinesterase: Enzyme kinetic and molecular docking studies. *Journal of Environmental Science and Health, Part B*, *53*(11), 713–718. https://doi.org/10.1080/03601234.2018.1480155

Thanosmit, C. (2016). Evaluation of abamectin effect on some biochemical constituents and histological alterations in Asian sea bass (Lates calcarifer). *Naresuan University Journal: Science and Technology*, *24*(1), 72–81.

Thiripurasundari, M., Sathya, K., Uma, A., Srinivasan, M. R., & Rajasekar, P. (2014). A comparative study on the toxicity of ivermectin in Zebra fish and Catla fish models. *Indo American Journal of Pharmaceutical Research*, *4*(9), 3683–3688.

Tietz, N. W., Rinker, A. D., & Shaw, L. M. (1983). IFCC methods for the measurement of catalytic concentration of enzymes Part 5. IFCC method for alkaline phosphatase (orthophosphoric-monoester phosphohydrolase, alkaline optimum, EC 3.1. 3.1). *Journal of Clinical Chemistry and Clinical Biochemistry. Zeitschrift fur klinischeChemie Und klinischeBiochemie*, *21*(11), 731.

Varo, I., Navarro, J. C., Amat, F., & Guilhermino, L. (2003). Effect of dichlorvos on cholinesterase activity of the European sea bass (*Dicentrarchus labrax*). *Pesticide Biochemistry and Physiology*, *75*(3), 61–72. https://doi.org/10.1016/S0048-3575(03)00019-1

Wahlang, B., Beier, J. I., Clair, H. B., Bellis-Jones, H. J., Falkner, K. C., McClain, C. J., & Cave, M. C. (2013). Toxicant-associated steatohepatitis. *Toxicologic Pathology*, *41*(2), 343–360. https://doi.org/10.1177/0192623312468517

Xu, Z., Liu, Y., Wei, P., Feng, K., Niu, J., Shen, G., Xu, Q., Wang, J., Smagghe, G. J., Xu, Q., He, L., & Lu, W. (2017). High gama-aminobutyric acid contents involved in abamectin resistance and predation, an interesting phenomenon in spider mites. *Frontiers in Physiology*, *8*, 216. https://doi.org/10.3389/fphys.2017.00216

Yoon, Y. J., Kim, E. S., Hwang, Y. S., & Choi, C. Y. (2004). Avermectin: Biochemical and molecular basis of its biosynthesis and regulation. *Applied Microbiology and Biotechnology*, *63*(6), 626–634. https://doi.org/10.1007/s00253-003-1491-4

Zambo, V., Simon-Szabó, L., Szelényi, P., Kereszturi, É., Bánhegyi, G., & Csala, M. (2013). Lipotoxicity in the liver. *World Journal of Hepatology*, *5*(10), 550. https://doi.org/10.4254/wjh.v5.i10.550

Zanoli, J. C. C., Maioli, M. A., Medeiros, H. C., & Mingatto, F. E. (2012). Abamectin affects the bioenergetics of liver mitochondria: A potential mechanism of hepatotoxicity. *Toxicology In Vitro*, *26*(1), 51–56. https://doi.org/10.1016/j.tiv.2011.10.007

Cogent Biology **(ISSN: 2331-2025) is published by Cogent OA, part of Taylor & Francis Group.**

Inorganica Chimica Acta 503 (2020) 119371

Contents lists available at ScienceDirect

Inorganica Chimica Acta

journal homepage: www.elsevier.com/locate/ica

Research paper

Supramolecular assemblies of new pseudohalide end-to-end bridged copper (II) complex and molecular structural variety of penta and hexa-coordinted metal(II) complexes with hydrazido-based ligand

Yogendra Singh[a,*], R.N. Patel[a,*], S.K. Patel[a], R.N. Jadeja[b], A.K. Patel[b], N. Patel[b], H. Roy[c], P. Bhagriya[c], Rita Singh[d,*], R.J. Butcher[e], Jerry P. Jasinski[f], S. Herrero[g], M. Cortijo[g]

[a] Department of Chemistry, APS University, Rewa 486003, India
[b] Department of Chemistry, Faculty of Science, The MS University of Baroda, Vadodara 390002, India
[c] Department of Zoology, Faculty of Science, The MS University of Baroda, Vadodara 390002, India
[d] Department of Physics, Govt. Model Science College, Rewa, MP 486001, India
[e] Department of Inorganic & Structural Chemistry, Howard University, Washington, DC 22031, USA
[f] Department of Chemistry, Keene State College, 229 Main Street, Keene, NH 03435-2001, USA
[g] Departamento de Química Inorgánica, Facultad de Ciencias Químicas, Universidad Complutense, 28040 Madrid, Spain

ARTICLE INFO

Keywords:
Metal(II) complexes
Quantum chemical calculations
Crystal structure
X-band EPR spectroscopy
Coordination chemistry

ABSTRACT

With an hydrazido-based ligand, $C_{14}H_{13}N_2O$ and Cu, Ni metal(II) salts, three new mononuclear $[Ni(HL)(NO_3)(H_2O)]NO_3$,$C_{14}H_{15}N_5NiO_8$, **1,** $[Cu(HL)(H_2O)_2]2NO_3$, $C_{14}H_{17}CuN_5O_4$, **2,** $[Ni(HL)_2]2ClO_4$, $C_{28}H_{30}Cl_2N_6NiO_{12}$, **3** and one binuclear end-to-end thiocynate bridged $[Cu_2(\mu\text{-}SCN)_2(L)_2]$, $C_{30}H_{24}Cu_2N_8O_2S_2$, **4** complexes have been synthesized and characterized by physico-chemical techniques. All of the complexes were structurally characterized using single crystal X-ray diffraction. Complexes **1** and **2** have a penta-coordinated environment around the metal(II) centre, whereas complex **3** has a distorted hexa-coordinated geometry. In complex **4** two symmetry related, adjacent copper(II) coordination moieties are joined end-to-end in an unprecedented manner forming a thiocynate bridged, yielding a dicopper entity. The presence of two "symmetric" thiocynate bridges with Cu-SCN and Cu-NCS distances of 2.832 Å and 1.925 Å, respectively, results in a Cu···Cu distance of 5.503 Å. Binuclear complex, **4** exhibits a weak antiferromagnetic interaction between adjacent copper(II) centres. These copper(II) mononuclear and binuclear complexes have also been studied by X-band EPR spectroscopy. The crystal packing of these new complexes is stabilized by H-bonding, weak intermolecular interactions, CH···π and $\pi\cdots\pi$ interactions. Electrochemical data (CV and DPV) for the complexes shows $M^{II} \rightarrow M^{I}$ reduction activity. Electronic spectroscopy and computational features are examined by quantum chemical studies. The inhibitory effect of the complexes were tested on a cell population with IMR 32 (neuroblastoma), MCF 7 (breast cancer), HepG2 (hepatocellular carcinoma), L132 (lung cells) cell lines by MTT assay. Complex **3** showed a prominent cytotoxicity against the all cell lines. Expression levels of the Bax (pro-apoptotic) and Bcl2 (anti-apoptotic) genes were also studied, wherein the genes of interest showed a moderate down regulation after treatment with complexes **1** and **3**. Finally, antioxidant superoxide dismutase activity measurements show that the complexes behave as superoxide dismutase mimics.

1. Introduction

In the present years, synthetic inorganic materials have achieved considerable interest in the production of a structural variety of molecular aggregates have received significant attention owing to their structural variety resulting from their transition metal-rich nature and chemical stability combined with their fascinating potential applications in advanced materials [1]. The chemistry of transition metal complexes has been found recently on the growth and improvement of supramolecular assemblies, ensembles and different structures aggregates [2]. Many attempts have been exercised to control the molecular structures arrangements in the crystals by simultaneous use of coordination bonds of a transition metal ion and involved hydrogen bondings [3]. A structural variety of ligands are commonly obtainable

* Corresponding authors.
E-mail addresses: ysapsurewa182@gmail.com (Y. Singh), rnp64@ymail.com (R.N. Patel), phy18188@gmail.com (R. Singh).

https://doi.org/10.1016/j.ica.2019.119371
Received 6 November 2019; Received in revised form 14 December 2019; Accepted 14 December 2019
Available online 17 December 2019

having the N, N and O as donor atoms, which can be used for the synthesis of metal organic frameworks [4] and coordination polymers [5]. Interest in coordination chemistry of aromatic hydrazones has increased due to their variable binding modes towards transition metal ions and to the possession of good biological activities [6]. Transition metal complexes with hydrazones have been a subject of a variety of studies for many years due to their potential antimicrobial and antitumor activities [7]. Transition metal complexes with aromatic hydrazone ligands are of great interest as well, since they have attractive biological properties [8]. Aromatic hydrazones may acts as tridentate (N_2O donors) neutral or monobasic ligands due to keto-enol tautomerization. Designed synthesis of di and polynuclear copper(II) complexes is an interesting area of research for their diverse structures and potential applications in magnetic materials. Hydrazone based copper (II) complexes can be mentioned for their structural diversity, as well as for their applications to see the effects of structural and chemical factors that govern the exchange coupling between paramagnetic centres [9]. The design and synthesis of pseudo halide bridged binuclear complexes has attracted considerable attention in the resent years, since such complexes with diverse structural variety can be obtained with new molecular materials with interesting technological importance [10]. The unprecedented asymmetric end-to-end thiocynate bridges within the equatorial axial copper(II) binuclear complex shows it to be an efficient transmitter of magnetic inter-coupling interactions, whereby $\pi\cdots\pi$ stacking interactions also play key roles in the field of the magnetic interaction.

The anticancer activity of copper(II) complexes originates from their redox activity which could result in the generation of a cytotoxic reactive oxygen species (ROS) [11] (Scheme 1). The superoxide anion ($O_2^{\cdot -}$) is a reactive oxygen species which is formed in biological systems. These superoxide radicals are formed when oxygen molecules gain one electron, which occurs mostly in mitochondria. In the presence of two electrons and two protons, O_2 is converted to H_2O_2, that is

$$O_2 \xrightarrow{2e^- + 2H^+} H_2O_2 \quad (1)$$

The role of a CuZnSOD enzyme is to disproportionate $O_2^{\cdot -}$ to O_2 and H_2O_2 in the following manner

$$Cu(II)SOD + O_2^{\cdot -} \rightarrow Cu(I)SOD + O_2 \quad (2)$$

$$Cu(I)SOD + O_2^{\cdot -} + 2H^+ \rightarrow Cu(II)SOD + H_2O_2 \quad (3)$$

It has been proposed that the reaction cycle of CuZnSOD involves inner sphere electron transfer from $O_2^{\cdot -}$ to Cu(II) and outer sphere electron transfer from Cu(I) to $O_2^{\cdot -}$ [12].

The strategy of mixed-ligand assembly has been becoming a successful approach for the manufacture of coordination frameworks with fascinating topologies [13]. The flexible *N*-donor ligands have been widely applicable in the formation of metal organic frameworks with different topologies [14]. In this work, we selected aromatic hydrazones with NNO donors sides flexible tridentate ligand to get intriguing structures and various potential applications. In the present study, we have reported the syntheses, crystal structure and characterizations of a binuclear Cu(II) complex and metal(II) mononuclear complexes. The reaction between copper(II) nitrate trihydrate, ligand (HL) and ammonium thiocynate (as a co-ligand) leads to the formation of an unprecedented pseudohalide end-to-end bridged complex, **4.** All of these complexes were characterized by elemental analysis, IR, UV–vis, X-band EPR of the copper(II) complexes, single crystal X-ray diffraction analysis and magnetic susceptibility studies. The inhibitory effects of the complexes were tested on a cell population with four cell lines by MTT assay. Cell lines are namely IMR 32 (neuroblastoma), MCF 7 (breast cancer), HepG2 (hepatocellular carcinoma), L132 (lung cells). Complex **3** showed a prominent cytotoxicity against the all cell lines. Expression levels of the Bax (pro-apoptotic) and Bcl2 (anti-apoptotic) genes were also studied. These complexes showed a similar activity compared to that of cisplatin, however no systematic behavior could be observed. Moreover, antioxidant superoxide measurements showed that these complexes exhibit effective dismutase activity and hence form a potential application as an antioxidant.

2. Experimental section

2.1. Materials

All of the chemicals and solvents used for the synthesis of these complexes were used as received without further purification. Copper (II) perchlorate hexahydrate, nickel(II) nitrate hexahydrate, 2-benzoylpyridine and acetylhydrazide were purchased from Aldrich and

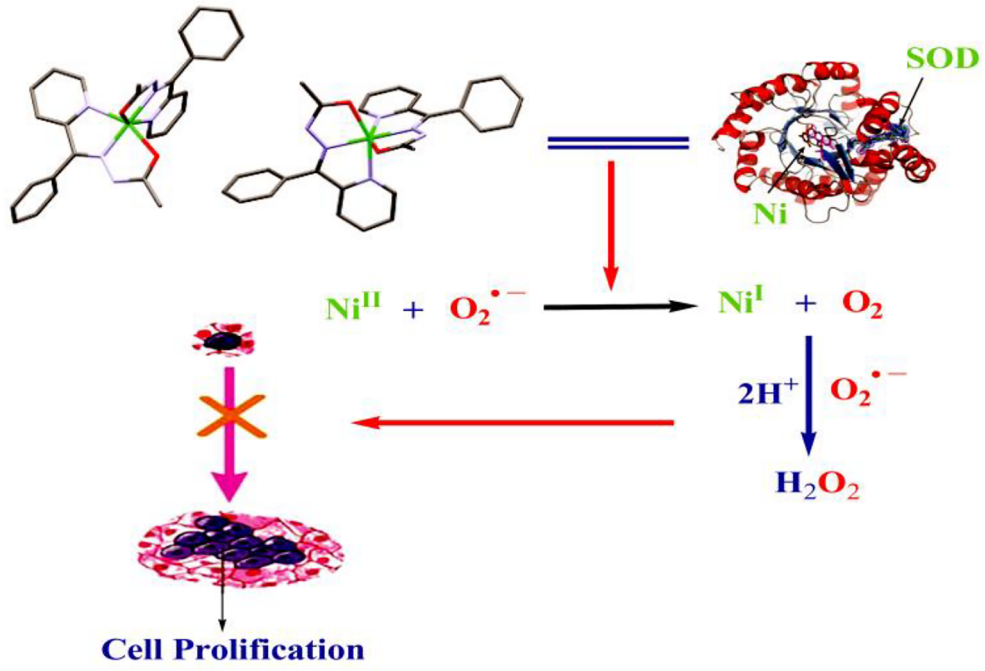

Scheme 1. A proposed mechanism suggested for dismutation reaction catalyzed by **3**.

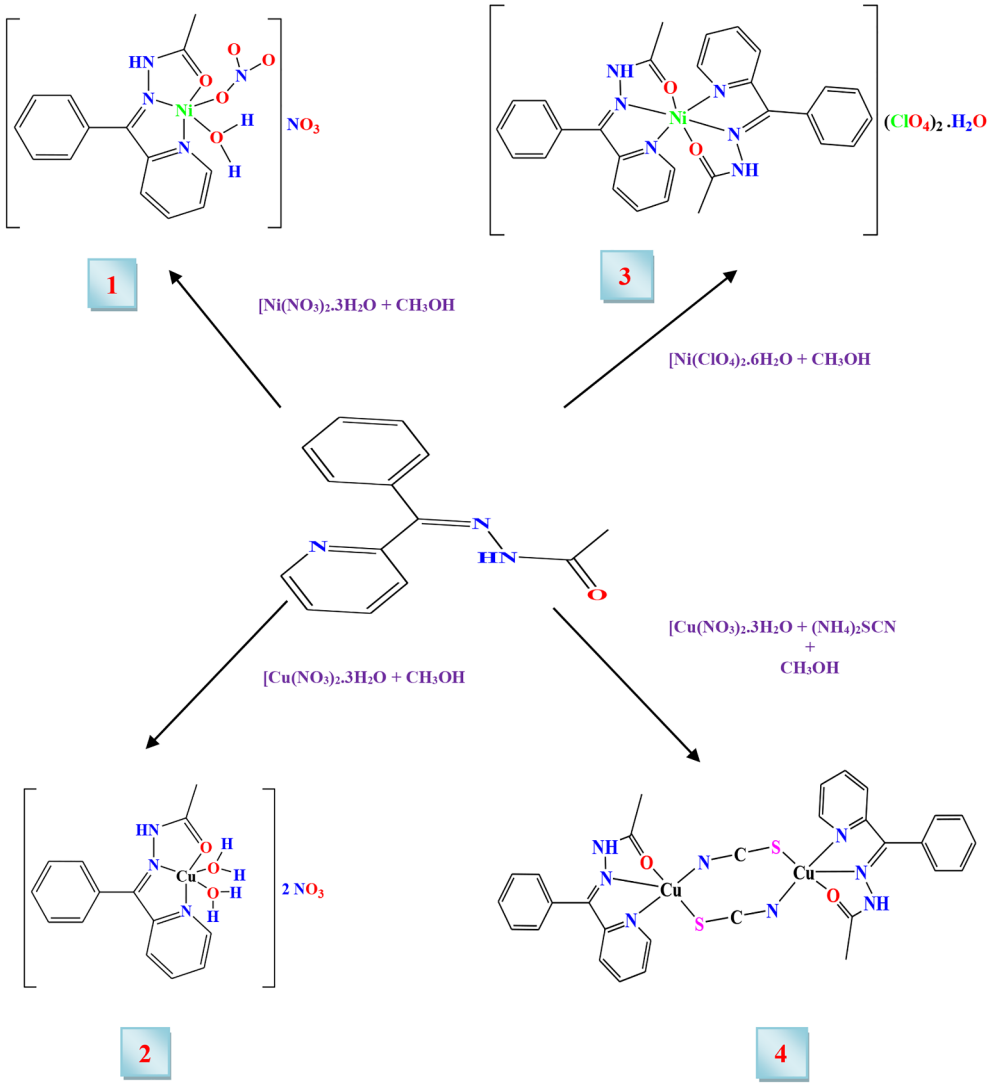

Scheme 2. Synthesis of complexes **1–4.**

Across Chemicals and used without further purification. The solvents were purified before use [15].

2.2. Physical measurements

Elemental analyses were determined by an Elementar Vario EL III Carlo Erba 1108 Analyzer. Electrical conductivity measurements were performed on freshly prepared 3 × 10^{-3} M DMSO solutions measured on a Systronics Conductivity TDS meter 308. The solutions were ~10^{-3} mol dm^{-3} in the complexes and 0.1 mol dm^{-3} in tetrabutyl ammonium perchlorate (TBAP) as a supporting electrolyte. UV–vis spectra were taken at room temperature on a Shimadzu UV–vis recording Spectrophotometer UV-1601 in quartz cells. Infrared (IR) spectra (4000–400 cm^{-1}) were recorded using the KBr pellet technique on a Perkin-Elmer FTIR spectrophotometer. The ^{1}H NMR spectrum of the ligand was obtained in CH_3OD with a Bruker Advance 400 (FT-NMR) Instrument. Chemical shifts were reported in parts per million (ppm) using tetramethylsilane (TMS) as internal standard. The electron paramagnetic resonance (EPR) spectra were recorded with a Varian E-line Century Series X-band Spectrometer equipped with a dual cavity. Tetracyanoethylene (TCNE) was used as a marker (g = 2.00277). Cyclic voltammetry was performed using a BAS-100 Epsilon Electrochemical Analyzer on complexes **1–4** in DMSO solutions using Ag/AgCl as a reference electrode and glassy carbon as a working electrode. The solutions were ~10^{-3} mol dm^{-3} in the complex and 0.1 mol dm^{-3} in tetrabutyl ammonium perchlorate (TBAP) as a supporting electrolyte. Ferrocene (Fe) was added to the solution as an internal standard. All measurements were carried out at room temperature under a nitrogen atmosphere. Magnetic data were recorded at 2–300 K under a 0.5 T magnetic field with a Quantum Design MPMSXL Superconducting Quantum Interference Device (SQUID) magnetometer whereby 25.33 mg of a finely ground sample of **4** was measured. The magnetic data was corrected taking into account the intrinsic diamagnetic contributions on the basis of Pascal's constants and the Temperature Independent Magnetism (TIP) of the Cu^{2+} ions and the sample holder. X-ray crystallographic data for **HL** and **1–4** were collected on a Rigaku-Oxford Diffraction Gemini Eos diffractometer using graphite monochromated CuKα radiation (λ = 1.54184 Å). All non-hydrogen atoms were refined anisotropically and all hydrogen atoms were geometrically fixed in their calculated positions. The structures

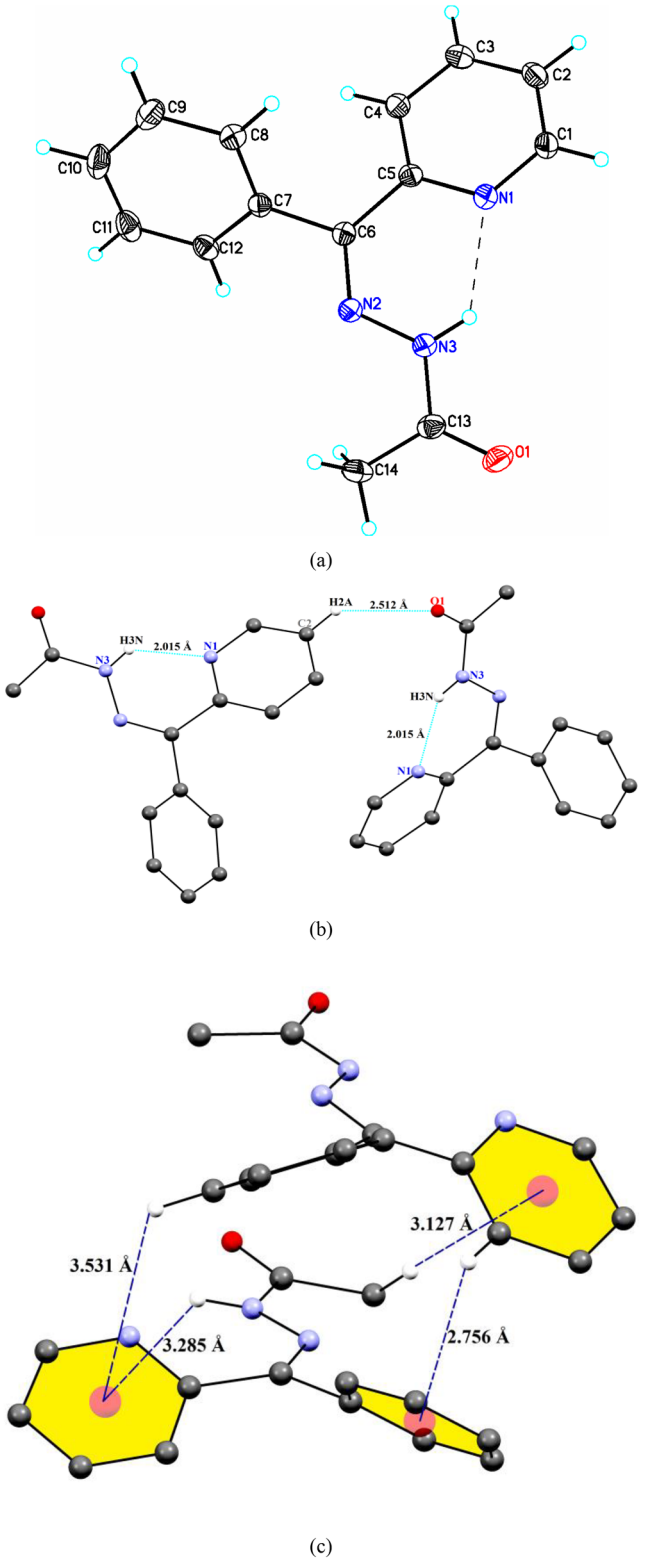

Fig. 1. (a) ORTEP Structure of **HL** (Dashed lines indicate *N*-H···N intramolecular H-bonds), (b) Structure of HL viewed along the a-axis (Dashed lines indicate *N*-H···N intra-molecular H-bonds and C-H···O weak intermolecular interactions), (c) A view of the weak CH···π interactions for **HL** (distances in Angstroms).

were solved by direct methods using SHELXS-97 [16] and refined by full-matrix least-squares using SHELXL-97 [17]. Crystals suitable for single-crystal X-ray analysis for of all complexes were grown by slow evaporation of the reaction mixtures at room temperature. Single crystals suitable for single-crystal X-ray analysis were mounted on polymer loops and then used for data collection.

2.3. Theoretical quantum chemical calculations

All quantum chemical calculations were carried out using the GUASSIAN 09 program package [18] by the DFT/B3LYP method. The input files of the metal(II) complexes were prepared with Gauss View 5.0.9 [19]. In the computational model, the anion was ignored and only the cationic complexes were taken into account. The electronic transitions of the complexes were made by using the time dependent density functional theory (TD-DFT)/B3LYP method with a LANL2DZ basis set in the gas phase [20]. Vertical electronic excitations based on B3LYP optimized geometries were computed using the time dependent density functional theory (TD-DFT) [21] in DMSO with a conductor-like polarizable continuum model (PCM) [22].

2.4. Antioxidant superoxide dismutase (SOD) assay

The *in-vitro* antioxidant superoxide dismutase (SOD) activity was measured using alkaline DMSO as a source of the superoxide radical ($O_2^{\cdot -}$) and NBT as an $O_2^{\cdot -}$ scavenger, according to a procedure already described in the literature [23]. In general, 400 µL samples to be assayed were added to a solution containing 2.1 ml of 0.2 mol L^{-1} potassium phosphate buffer (pH 8.6). 1 ml of 56 mmol L^{-1} alkaline DMSO solution was then added while stirring. The absorbance was monitored at 540 nm against a sample prepared under similar conditions except for using NaOH in DMSO. A unit of antioxidant SOD activity is the concentration of complex, which causes 50% (IC_{50}) inhibition of alkaline DMSO mediated reduction of NBT. The catalytic rate constants were calculated as $k_{McCF} = k_{NBT}$ [NBT] /IC_{50}, where k_{NBT} (pH = 7.8) = 5.94×10^4 M^{-1} S^{-1} [24].

Caution! Perchlorate salts of metal complexes with transition metal complexes are potentially explosive. They should be synthesized in small quantities and the materials should be synthesized with great care.

2.5. Synthesis of HL

The Schiff base was prepared by a standard literature method [25] and synthesized by reacting acetylhydrazide (0.741 g, 10.0 mmol) and 2-benzoylpyridine (1.832 g, 10.0 mmol) with each dissolved in ethanol for 1 h. After adding 2 drops of glacial acetic acid, the resulting solution was again refluxed for 4 h. The resulting light brown coloured solution was cooled to room temperature (RT) and filtered. The solid was dried over fused $CaCl_2$ in a desiccator. The product was recrystallized from hot ethanol (Scheme S1). Yield: 2.426 g, (53%). Anal. Calc. for $C_{14}H_{13}N_3O$ (239.27): C, 70.28; H, 5.48; N, 17.56. Found: C, 70.25; H, 5.46; N, 17.51%. IR (υcm^{-1}, KBr): υ (NH) 3455–3430 m; υ (C=O) 1638 s, υ (C=N) 1610 m (Fig. S1). ^{1}H NMR (MeOD, δppm): 2.35(s, 3H, CH_3); 4.83(s, NH); 7.34–8.81(m, 9H Ar-H). ^{13}C (MeOD); δ ppm) 20.12(m, CH_3); 40.94(s, C–O); 49.36 (S > C=N); 126.05–176.64(m, Ar-C). The single crystal structure of **HL** was further confirmed by XRD.

2.6. Synthesis of complexes

The reaction of **HL** with metal(II) salts in different conditions resulted in complexes **1–4** (Scheme 2).

2.7. Synthesis of [Ni(HL)(NO_3) (H_2O)](NO_3), 1

Complex **1** was synthesized by reacting 25 ml of methanolic solution of nickel(II) nitrate trihydrate (0.366 g 1 mmol) with 25 ml of a methanolic solution of ligand (0.239 g 1 mmol) in a round bottom flask. The resulting light brown coloured solution was cooled to room

Table 1
Crystal data and structure refinement for compounds HL and **1–4**.

Compounds	HL	1	2	3	4
Empirical formula	$C_{14}H_{13}N_3O$	$C_{14}H_{15}N_5NiO_8$	$C_{14}H_{17}CuN_5O_9$	$C_{28}H_{30}Cl_2N_6NiO_{12}$	$C_{30}H_{24}Cu_2N_8O_2S_2$
Formula weight	239.27	440.02	462.86	772.19	719.77
Temperature	173(2) K	173(2) K	173(2) K	173(2) K	173(2) K
Wavelength	1.54184 Å	1.54184 Å	1.54184 Å	1.54184 Å	1.54184 Å
Crystal system	Orthorhombic	Triclinic	Monoclinic	Triclinic	Orthorhombic
Space group	*Pna 2₁*	$P\bar{1}$	*P 2₁*	$P\bar{1}$	*Pbca*
Unit cell dimensions Å, °					
a	7.6525(2)	7.2740(5)	7.9488(7)	12.2765(6)	15.5879(5)
b	15.2519(4)	8.5854(5)	11.8141(9)	15.0985(8)	7.0707(2)
c	10.5906(3)	14.5486(11)	10.2189(9)	18.1055(7)	27.3859(9)
α	90	82.246(6)	90	94.701(4)	90°
β	90	76.509(6)	108.275(10)	90.228(4)	90°
γ	90	81.090(5)	90	90.494(4)	90°
Volume	1236.08(6) Å^3	868.20(11) Å^3	911.23(14) Å^3	3344.5(3) Å^3	3018.40(16) Å^3
Z	4	2	2	4	4
Density (calculated)	1.286 Mg/m^3	1.683 Mg/m^3	1.687 Mg/m^3	1.534 Mg/m^3	1.584 Mg/m^3
Absorption coefficient	0.676 mm^{-1}	2.148 mm^{-1}	2.270 mm^{-1}	2.926 mm^{-1}	3.390 mm^{-1}
F(0 0 0)	0.676 mm^{-1}	452	474	1592	1464
Crystal size	0.47 × 0.18 × 0.15 mm^3	0.41 × 0.23 × 0.21 mm^3	0.773 × 0.459 × 0.177 mm^3	0.41 × 0.35 × 0.18 mm^3	0.37 × 0.33 × 0.28 mm^3
Theta range for data collection	5.084 to 71.489°	5.243 to 71.502°	4.557 to 71.489°	3.977 to 71.319°	3.227 to 71.610°
Index ranges	$-9\le h\le 6$, $-18\le k\le 18$, $-13\le l\le 12$	$-6\le h\le 8$, $-10\le k\le 10$, $-17\le l\le 17$	$-9\le h\le 4$, $-13\le k\le 14$, $-11\le l\le 12$	$14\le h\le 15$, $-15\le k\le 18$, $-21\le l\le 16$	$-18\le h\le 18$, $-8\le k\le 8$, $-33\le l\le 27$
Reflections collected	7579	5718	2554	14,749	21,150
Independent reflections	2180 [R(int) = 0.0294]	3299 [R(int) = 0.0187]	2554 [R(int) = 0.1055]	10,404 [R(int) = 0.0309]	2919 [R(int) = 0.0531]
Completeness to theta = 67.500°	99.9%	99.6%	99.2%	99.9%	99.6%
Absorption correction	Semi-empirical from equivalents	Semi-empirical from equivalents	Analytical	Semi-empirical from equivalents	Semi-empirical from equivalents
Max. and min. transmission	1.00000 and 0.80380	1.00000 and 0.31352	0.700 and 0.355	1.00000 and 0.59703	1.00000 and 0.28996
Refinement method	Full-matrix least-squares on F^2	Full-matrix least-squares on F^2	Full-matrix least-squares on F^2	Full-matrix least-squares on F^2	Full-matrix least-squares on F^2
Data / restraints / parameters	2180 / 1 / 168	3299 / 12 / 277	2554 / 7 / 275	10,404 / 113 / 936	2919 / 0 / 201
Goodness-of-fit on F^2	1.044	1.043	1.065	1.020	1.096
Final R indices [I > 2sigma(I)]	R1 = 0.0341, w*R2* = 0.0908	R1 = 0.0327, w*R2* = 0.0864	R1 = 0.0473, w*R2* = 0.1259	R1 = 0.0594, w*R2* = 0.1607	R1 = 0.0404, w*R2* = 0.1061
R indices (all data)	R1 = 0.0349, w*R2* = 0.0917	R1 = 0.0355, w*R2* = 0.0883	R1 = 0.0483, w*R2* = 0.1277	R1 = 0.0694, w*R2* = 0.1762	R1 = 0.0443, w*R2* = 0.1098
Absolute structure parameter	0.0(3)	0.0028(4)	0.00(5)	–	–
Extinction coefficient	n/a	n/a	n/a	n/a	n/a
Largest diff. peak and hole	0.131 and −0.206 e.Å^{-3}	0.418 and −0.351 e.Å^{-3}	0.722 and −0.493 e.Å^{-3}	1.032 and −0.636 e.Å^{-3}	0.651 and −0.335 e.Å^{-3}

temperature (RT). The solid was dried over fused $CaCl_2$in a desiccator. A brown crystal of single crystal XRD quality was obtained after a few days by slow evaporation of a light dark brown solution of the complex. Yield from methanol. Brown, yield (68%) Anal. Calc. for $C_{14}H_{15}NiO_8$ (440.02): C, 38.22; H, 3.44; N, 15.92. Found: C, 38.18; H, 3.42; N, 15.78%. IR data (KBr disc, cm^{-1}): 3780, 3073, 2926, 1693, 1609, 1520, 1384, 1309, 1204, 1107, 1028, 917, 829, 694, 599,520, 472 and 431 [Fig. S1 (b)].

2.8. Synthesis of $[Cu(HL)\ (H_2O)_2](NO_3)_2$, 2

Complex **2** was synthesized using the same method as for complex **1**, except that nickel nitrate was replaced by copper nitrate. The deep green solution obtained was kept at room temperature (RT) for one week under going slow evaporation of the resulting solution by a similar method. Dark green crystals were obtained, which were isolated and dried over a fused $CaCl_2$in a desiccator. Green, yield (68%) Anal. Calc. for $C_{14}H_{17}NiO_9$ (462.86): C, 36.32; H, 3.70; N, 15.13. Found: C, 36.31; H, 3.68; N, 15.12%. IR data (KBr disc, cm^{-1}): 3443, 3076, 2932, 2778, 2429, 2327, 1893, 1609, 1521, 1385, 1308, 1210, 1139, 1109, 1030, 919, 830, 799, 694, 602,517 and 456 [Fig. S1(c)].

2.9. Synthesis of $[Ni(HL)_2](ClO4)_2$, 3

Complex **3** was synthesized in a manner similar to that for complex **1** except that nickel nitrate was replaced by nickel perchlorate. The deep brown solution obtained was kept at room temperature (RT) for one week by slow evaporation. Green crystals were obtained, which were isolated and dried over a fused $CaCl_2$in a desiccator. Green, yield (68%) Anal. Calc. for $C_{14}H_{17}NiO_9$ (772.19): C, 43.55; H, 3.92; N, 10.88.Found: C, 43.54; H, 3.89; N, 10.86%. IR data (KBr disc, cm^{-1}): 3413, 3078, 2927, 2767, 2017, 1623, 1512, 1458, 1379, 1336, 1270, 1198, 1089, 935, 853, 794, 747, 703, 626, 515 and 448 [Fig. S1(d)].

2.10. Synthesis of $[Cu_2\ (\mu\text{-}SCN)_2(L)_2]$, 4

Complex **4** was synthesized by reacting 25 ml of a methanolic solution of copper(II) perchlorate (0.370 g 1 mmol) with 25 ml of a methanolic solution of N'-[(Z)-phenyl(pyridin-2-l) methylidene]acetohydrazide (0.239 g 1 mmol) in a round bottom flask which produced a light green coloured solution. A methanol solution of ammonium thiocyanate (0.076 gm 1 mmol) was then added to it and stirred for 2 h. The resulting solution was filtered and left for slow evaporation to get

Table 2
Coordination bond lengths [Å] and angles [°] for **HL** and 1–**4**.

HL	Experimental Data	Theoretical Data*		Experimental Data	Theoretical Data*
O(1)-C(13)	1.218(3)	1.286	N(1)-C(1)	1.341(3)	1.368
N(1)-C(5)	1.355(3)	1.369	N(2)-C(6)	1.287(3)	1.298
N(2)-N(3)	1.368(3)	1.438	N(3)-C(13)	1.361(3)	1.398
N(3)-H(3 N)	0.89(3)	0.91			
C(1)-N(1)-C(5)	117.78(18)	117.87	C(6)-N(2)-N(3)	120.15(16)	121.42
C(13)-N(3)-N(2)	120.26(17)	120.56	C(13)-N(3)-H(3 N)	117.6(19)	118.78
N(2)-N(3)-H(3 N)	121.5(19)	121.59	N(1)-C(1)-C(2)	123.8(2)	124.08
N(1)-C(1)-H(1A)	118.1	118.60			
1					
Ni-N(2)	1.9426(17)	2.0422	Ni-O(1 W)	1.9459(16)	2.1089
Ni-N(1)	2.0029(18)	2.0320	Ni-O(1)	2.0111(15)	2.0218
Ni-O(11)	2.2036(16)	2.2096			
N(2)-Ni-O(1 W)	163.04(7)	163.34	N(2)-Ni-N(1)	79.81(7)	81.29
O(1 W)-Ni-N(1)	101.42(7)	102.02	N(2)-Ni-O(1)	79.48(6)	84.88
O(1 W)-Ni-O(1)	97.22(7)	98.38	N(1)-Ni-O(1)	158.89(7)	160.01
N(2)-Ni-O(11)	112.78(7)	112.98	O(1 W)-Ni-O(11)	84.06(7)	85.06
N(1)-Ni-O(11)	95.16(7)	96.36	O(1)-Ni-O(11)	96.53(6)	97.09
2					
Cu–N(2)	1.942(4)	2.024	Cu–O(1 W)	1.947(3)	2.048
Cu–N(1)	2.018(5)	2.038	Cu–O(1)	2.032(4)	2.053
Cu–O(2 W)	2.304(4)	2.338	Cu–O(12)	2.495(5)	2.533
N(2)-Cu–O(1 W)	175.80(17)	176.70	N(2)-Cu–N(1)	79.27(18)	80.54
O(1 W)-Cu–N(1)	97.61(18)	98.21	N(2)-Cu–O(1)	79.74(18)	81.78
O(1 W)-Cu–O(1)	103.13(17)	104.25	N(1)-Cu–O(1)	158.58(17)	160.88
N(2)-Cu–O(2 W)	95.7(2)	97.80	O(1 W)-Cu–O(2 W)	87.41(19)	90.48
N(1)-Cu–O(2 W)	95.61(18)	96.98	O(1)-Cu–O(2 W)	90.61(17)	91.68
N(2)-Cu–O(12)	96.5(2)	96.85	O(1 W)-Cu–O(12)	80.66(19)	81.86
N(1)-Cu–O(12)	91.45(19)	92.95	O(1)-Cu–O(12)	86.77(19)	87.76
O(2 W)-Cu–O(12)	166.85(16)	167.89			
3					
Ni(1)-N(2A)	1.971(3)	2.078	Ni(1)-N(5A)	1.980(3)	2.083
Ni(1)-N(1A)	2.070(3)	2.076	Ni(1)-N(4A)	2.077(3)	2.098
Ni(1)-O(1A)	2.105(2)	2.208	Ni(1)-O(2A)	2.106(3)	2.206
Ni(2)-N(5B)	1.983(3)	2.086	Ni(2)-N(2B)	1.988(3)	2.089
Ni(2)-N(1B)	2.066(4)	2.168	Ni(2)-N(4B)	2.077(3)	2.099
Ni(2)-O(2B)	2.102(3)	2.212	Ni(2)-O(1B)	2.115(3)	2.205
N(2A)-Ni(1)-N(5A)	175.09(12)	176.28	N(2A)-Ni(1)-N(1A)	78.27(12)	80.67
N(5A)-Ni(1)-N(1A)	105.86(12)	106.65	N(2A)-Ni(1)-N(4A)	104.16(12)	105.86
N(5A)-Ni(1)-N(4A)	78.28(12)	80.45	N(1A)-Ni(1)-N(4A)	95.87(11)	96.98
N(2A)-Ni(1)-O(1A)	77.94(11)	80.08	N(5A)-Ni(1)-O(1A)	97.69(11)	98.89
N(1A)-Ni(1)-O(1A)	155.66(11)	156.68	N(4A)-Ni(1)-O(1A)	94.83(10)	95.83
N(2A)-Ni(1)-O(2A)	99.91(11)	101.06	N(5A)-Ni(1)-O(2A)	77.52(11)	80.42
N(1A)-Ni(1)-O(2A)	91.49(11)	92.44	N(4A)-Ni(1)-O(2A)	155.79(12)	156.76
O(1A)-Ni(1)-O(2A)	87.59(11)	88.89	N(5B)-Ni(2)-N(2B)	177.00(13)	176.09
N(5B)-Ni(2)-N(1B)	102.77(13)	102.89	N(2B)-Ni(2)-N(1B)	78.15(13)	78.55
N(5B)-Ni(2)-N(4B)	77.82(13)	77.99	N(1B)-Ni(2)-N(4B)	95.78(13)	95.98
N(2B)-Ni(2)-N(4B)	104.98(13)	105.08	N(2B)-Ni(2)-O(2B)	99.68(12)	99.98
N(5B)-Ni(2)-O(2B)	77.43(12)	77.83	N(5B)-Ni(2)-O(1B)	102.00(12)	102.89
N(4B)-Ni(2)-O(2B)	154.81(13)	155.45	N(1B)-Ni(2)-O(1B)	155.16(12)	155.98
N(2B)-Ni(2)-O(1B)	77.02(12)	77.62	O(2B)-Ni(2)-O(1B)	89.53(12)	89.89
N(4B)-Ni(2)-O(1B)	91.08(13)	91.98			
4					
Cu–N(5)	1.925(2)	2.098	Cu–N(2)	1.927(2)	2.079
Cu–O(1)	1.9677(17)	2.064	Cu–N(1)	2.016(2)	2.092
Cu-S(1)#1	2.8220(7)	2.902			
N(5)-Cu–N(2)	176.60(9)	177.68	N(5)-Cu–O(1)	99.99(8)	100.09
N(2)-Cu–O(1)	80.25(7)	81.65	N(5)-Cu–N(1)	98.53(8)	100.03
N(2)-Cu–N(1)	80.72(8)	80.73	O(1)-Cu–N(1)	159.38(8)	162.89
N(5)-Cu-S(1)#1	96.48(7)	96.98	N(2)-Cu-S(1)#1	86.89(6)	90.08
O(1)-Cu-S(1)#1	92.04(6)	95.94	N(1)-Cu-S(1)#1	94.80(6)	95.76

*Quantum chemical calculations data.

X-ray quality single crystals. The solid was dried over fused $CaCl_2$in a desiccator. The product was recrystallized in yield from methanol. Green, yield (68%) Anal. Calc. for $C_{30}H_{24}Cu_2N_8O_2S_2$ (719.77): C, 50.05; H, 3.36; N, 15.56. Found: C, 50.04; H, 3.35; N, 15.49%. IR data (KBr disc, cm^{-1}): 3450, 3071, 2927, 2855, 2361, 2170, 2088, 1609, 1598, 1525, 1499, 1445, 1390, 1299, 1268, 1199, 1095, 937.69, 792, 745, 700, 621, 522, 454 and 428 [Fig. S1(e)].

2.11. Cytotoxicity assay

To analyse cytotoxicity of the synthesized compounds, an MTT assay was performed on selected cell lines of neuroblastoma (IMR 32), Breast cancer (MCF 7), Hepatocellular carcinoma (HepG2) and lung immortal cells (L 132). Cells were exposed to different concentrations of compounds **1**–**4** and **HL** for 24 h. MTT exposure was given for 4 h in the dark, and then the developed formazan crystals were dissolved in 200 ml of DMSO. Absorbance was measured at 590 nm.

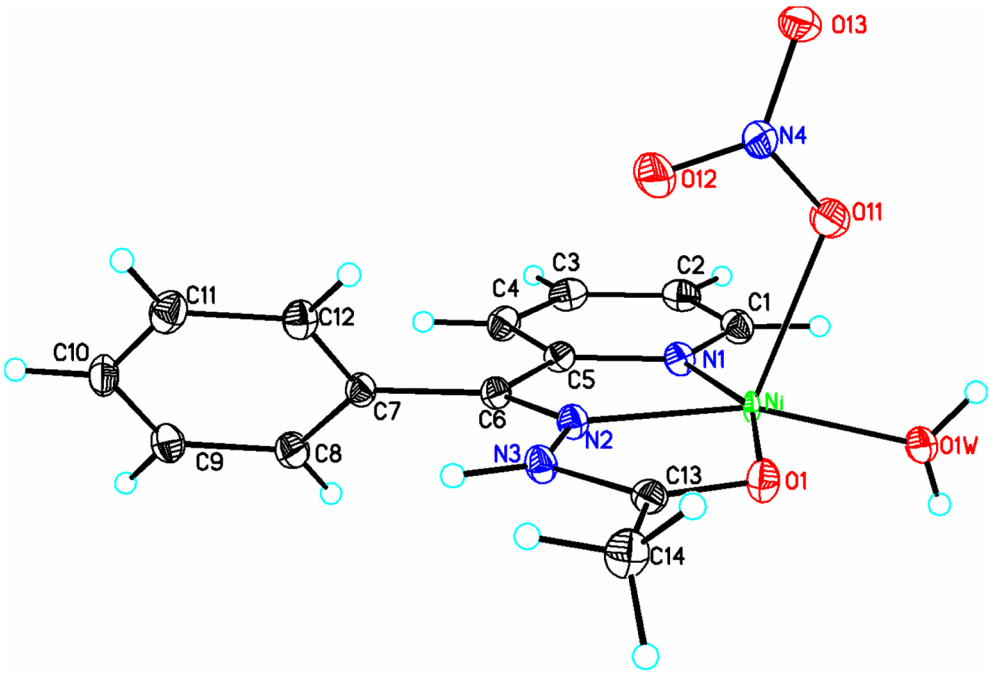

(a)

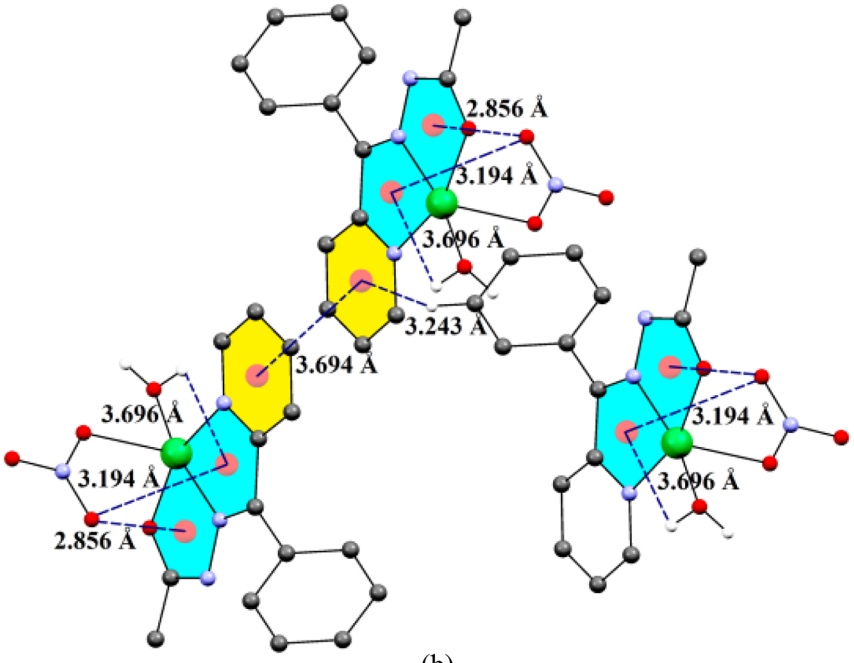

(b)

Fig. 2. (a)ORTEP structure of **1**, showing the atomic numbering scheme and 30% probability displacement ellipsoids, (b) A view of the weak CH···π and π···π interactions for **1** (distances are in Angstroms),(c) Bifurcated and trifurcated H-bonding and weak intermolecular interactions for **1**, see Table S1.

2.12. Gene expression analysis

IMR 32 cells were incubated in 6 well plates overnight for adhesion. Cells were exposed to compounds **1** and **3** for 24 h. RNA was isolated using the TRIzol reagent (Takara). Extracted RNA was quantified using a Nano Drop spectrophotometer. cDNA was synthesized using a BIO-RAD iScript cDNA synthesis kit. Real time PCR was performed on cDNA using a Power up SYBR Green mix (Invitrogen). The primer was designed using BLAST software from NCBI. β-actin was used as a housekeeping gene for the study (Bcl2: F-5′GCCCGAGAACCTAATGG CTT3′, R: 5′CTCAGGGACTCACTCTGCTG3′; Bax: 5′GCCCTTTTGCTTCA GGGTTT3′, R: 5′GGAAAAAGACCTCTCGGGGG3′; β-actin: F- 5′ CCACC ATGTACCCTGGCATT3′, R: 5′ CGCTCAGGAGGAGCAATGAT3′). Data were analyzed using comparative ΔCt method for each of the target gene with reference to housekeeping gene. Statistically significant difference data was evaluated with parametric ANOVA using Graph Pad prism software, version 7.

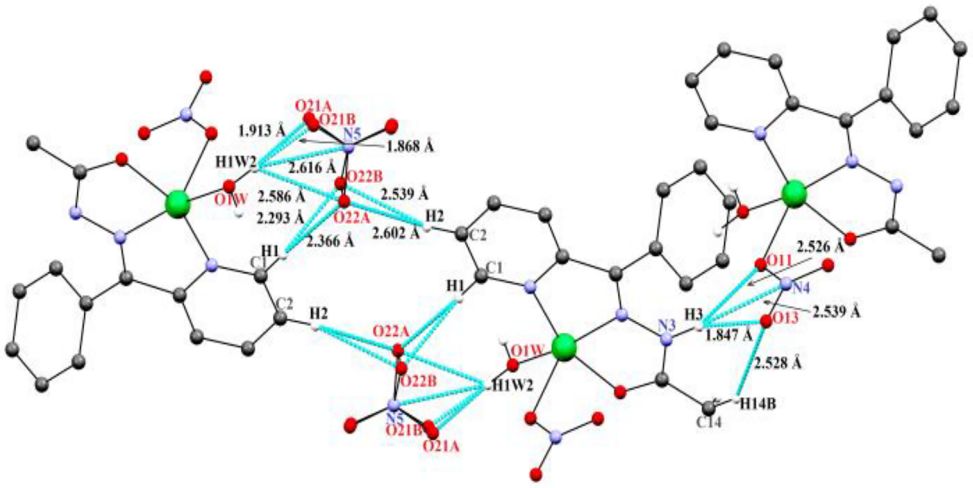

(c)

Fig. 2. (*continued*)

2.13. AO/EB staining

Cells were seeded on Poly L lysine coated with a coverslip in a 6 well-plate. Cells were treated by compounds **1** and **3** for 24 h. After treatment, the cells were fixed and stained by dual staining (acredine orange (AO) 4: Ethidium bromide (EB) 1) for 20 min in the dark. Cells were rinsed by PBS ad observed under a fluorescent microscope.

3. Results and discussion

3.1. Synthesis and characterization

Reaction between the metal(II) salts and the **HL** ligand mixed in a 1:1 ratio in methanol lead to the three mononuclear complexes (**1–3**). In a similar manner, complex **4** was synthesized by taking copper perchlorate hexahydrate, **HL**, and NH_4SCN as a co-ligand in a 1:1:1 ratio in methanol. These complexes were characterised by elemental analysis, UV–visible, IR and electrochemical techniques. Finally, these complexes were analyzed by single crystal X-ray diffraction and the structures of mono/binuclear complexes $[Ni(HL)(NO_3)(H_2O)]NO_3$ **1**, $[Cu(HL)(H_2O)_2]2NO_3$ **2**, $[Ni(HL)_2]2ClO_4$ **3** and $[Cu_2(\mu\text{-}SCN)_2(L)_2]$ **4** were obtained. The complexes showed a molar conductivity (ΛM) of 130 for **1**, 128 for **2** and 210 $\Omega\ cm^{-2}\ mol^{-1}$ for **3** in DMSO solution corresponding to ratios of 1:1 (**1** & **2**) and 1:2 (**3**) for the electrolyte. Complex **4** shows a molar conductance of 15 $\Omega\ cm^{-2}\ mol^{-1}$ which corresponds to a non-electrolyte in nature.

3.2. Crystal structure of ligand (HL)

The molecular structure of ligand (**HL**) with atomic labeling is shown Fig. 1a. **HL** crystallizes in the orthorhombic system with space group $Pna2_1$. The ligand molecule shows a *Z* molecular confirmation about the > C═N- bond. The N(2)-N(3) bond length of 1.368(3)Å, is shorter than a single bond length of 1.411 Å, and displays double bond character (Schiff base formation) [26]. The C(6)—N(2) and C(13)—O(1) bond lengths of 1.287(3) Å and 1.218(2) Å are also of double bond character [27]. The Py—C(6)—N(2)—C(13)═O(1) Skelton in **HL** is planar owing to presence of an N(3)—H···N(1) intra-molecular hydrogen bond. The molecular packing is dominated by a network of N(3)—H···N(1) intra-molecular H-bonds (Fig. 1b). Beside intra-molecular H-bonding, weak CH···π interactions are present respectively. Similarly, weak CH···π intermolecular distances (CH of a py/phenyl ring with a π electron of the py/phenyl rings) are in the range 2.756–3.531 Å (Fig. 1c). One more weak CH···π intermolecular interaction (CH of an acetyl group with aπ electron from a pyridine ring) is present with a distance of 3.127 Å. Crystal packing of **HL** viewed along the a-axis (Fig. S2a).

3.3. Description of molecular structures

The crystallographic parameters of these complexes are presented in Table 1, whereas the relevant bond angles and bond length are given in Table 2.

An ORTEP representation of molecular structure **1** including the atomic numbering scheme is shown in Fig. 2(a). Complex **1** has a penta-coordinate structure. The nickel atom is coordinated by three oxygen atoms (O1, O11 and O1W) and two nitrogen atoms (N1, N2). There are two nitrogen atoms and one oxygen atom from the tridentate ligand (**HL**) and one oxygen atom (O1W) from a coordinated water molecule in the equatorial plane and one terminal oxygen atom(O11) from a nitrate ion in the axial position. The Ni—O bond length of 2.2036(16) Å, in the axial position, is clearly longer than the Ni—O equatorial bond length, 1.9459(16) Å. The distances of the Ni-N1, Ni-N2 and Ni-O are 2.0029(18) Å, 1.9426(17) Å and 2.0111(15) Å, in agreement with the values of a similar Ni(II) complex [27]. The value of the structural index (τ index) [28] τ is 0.069 [$\tau=(\beta\text{-}\alpha)/60$, where α = N(1)-Ni-O (1) = 158.89(7) ° and β = N(2)-Ni-O(1 W) = 163.04(7)°; for perfect square pyramidal and trigonal bipyramidal geometries, the τ values are zero and unity [29], respectively]. Thus, such a low τ structural index value suggests a slightly distorted square pyramid geometry. The molecular structure of this complex is comparable to those of similar square pyramidal complexes reported in the literature [30]. A unique interactions between coordinated water molecules and chelate rings (lp···π) has been observed, by single crystal X-ray analysis [31]. One oxygen atom from a coordinated nitrate ion forms a weak intermolecular interaction with a lone pair electron of a metal chelate with short distances of 2.854 Å [32]. Besides these interactions, there are weak $\pi\cdots\pi$(aryl-aryl) intermolecular interactions in a slipped pattern between the pyridyl rings with centeroid-centeroid distances of 3.691 Å, Fig. 2(b), Table 3. Thus, the crystal structure of this complex is stabilized by weak intermolecular H-bonds, ln···π(metal chelate) [Fig. 2(b)] and $\pi\cdots\pi$ (aryl-aryl) interactions. Hydrogen atoms of co-ordinated water molecules form trifurcated H-bonding and weak intermolecular interactions with nitrogen and oxygen atoms of an un-coordinated nitrate ion (O1W-H···O21, O1W-H···N5 and O1W-H···O22). Similarly, H-atoms of the metal chelate ring form trifurcated H-

Table 3
Hydrogen bonds and weak intermolecular interactions for **HL** and **1-4** [Å and °].

D-H...A	d(D-H)	d(H...A)	d(D...A)	< (DHA)	Symmetry transformations used to generate equivalent atoms
HL					
N(3)-H(3N)...N(1)	0.89(3)	2.01(3)	2.675(2)	130(2)	#1 -x+1,-y+1,z-1/2
C(2)-H(2A)...O(1)#1	0.95	2.51	3.241(3)	133.5	
1					
O(1W)-H(1W1)...N(5)#1	0.831(17)	2.56(2)	3.269(2)	145(3)	#1 -x+2,-y,-z #2 x-1,y,z #3 -x+2,-y+1,-z
O(1W)-H(1W1)...O(23A)#1	0.831(17)	1.85(3)	2.67(3)	167(3)	
O(1W)-H(1W1)...O(23B)#1	0.831(17)	2.09(2)	2.905(11)	168(3)	
O(1W)-H(1W2)...N(5)	0.844(17)	2.60(2)	3.392(2)	157(3)	
O(1W)-H(1W2)...O(21A)	0.844(17)	1.90(2)	2.738(14)	175(3)	
O(1W)-H(1W2)...O(22A)	0.844(17)	2.57(3)	3.157(7)	128(3)	
O(1W)-H(1W2)...O(21B)	0.844(17)	1.84(2)	2.678(5)	170(3)	
N(3)-H(3N)...O(11)#2	0.94(3)	2.59(3)	3.200(2)	123(2)	
N(3)-H(3N)...O(13)#2	0.94(3)	1.88(3)	2.801(2)	165(3)	
N(3)-H(3N)...N(4)#2	0.94(3)	2.59(3)	3.442(2)	150(2)	
C(1)-H(1A)...O(22A)	0.95	2.39	3.334(6)	175.7	
C(1)-H(1A)...O(22B)	0.95	2.29	3.163(3)	153.1	
C(2)-H(2A)...O(22A)#3	0.95	2.63	3.487(7)	150.8	
C(2)-H(2A)...O(22B)#3	0.95	2.54	3.463(4)	164.7	
C(4)-H(4A)...O(21B)#4	0.95	2.64	3.373(5)	134.8	
C(14)-H(14C)...O(13)#2	0.98	2.55	3.362(3)	140.8	
2					
O(1W)-H(1W1)...O(21)	0.82(2)	1.91(4)	2.685(7)	156(8)	#1 -x+1,y-1/2,-z+1 #2 x+1,y,z+1
O(1W)-H(1W2)...O(11)#1	0.82(2)	1.92(3)	2.687(7)	156(7)	#3 x-1,y,z #4 -x+1,y-1/2,-z+2
O(2W)-H(2W1)...O(11)#1	0.82(2)	2.34(5)	3.013(6)	140(8)	
O(2W)-H(2W1)...O(12)#1	0.82(2)	2.58(6)	3.140(7)	127(6)	
O(2W)-H(2W2)...O(21)#1	0.82(2)	1.98(4)	2.773(7)	162(8)	
N(3)-H(3B)...N(5)#2	0.88	2.66	3.493(7)	158.4	
N(3)-H(3B)...O(22)#2	0.88	2.20	3.042(7)	160.6	
N(3)-H(3B)...O(23)#2	0.88	2.47	3.140(8)	133.1	
C(2)-H(2A)...O(2W)#3	0.95	2.52	3.397(7)	153.3	
C(4)-H(4A)...O(11)#4	0.95	2.52	3.449(7)	164.4	
C(14)-H(14B)...O(22)#2	0.98	2.56	3.457(9)	151.9	
3					
N(3A)-H(3AB)...O(11)	0.88	2.24	2.884(4)	130.3	#1 -x+2,-y+1,-z+1 #2 -x+1,-y+1,-z+1 3 -x,-y+2
N(6A)-H(6AA)...O(2W)	0.88	1.85	2.715(5)	168.1	-z #4 -x+1,-y+2,-z #5 -x+1,-y+1,-z #6 x,y,z-1
C(1A)-H(1AA)...O(31)	0.95	2.64	3.514(7)	153.5	
C(15A)-H(15A)...O(44)#1	0.95	2.51	3.173(6)	126.8	
C(28A)-H(28A)...O(41)#2	0.98	2.44	3.388(5)	161.6	
C(28A)-H(28B)...O(2W)	0.98	3.03	3.359(6)	101.3	
N(3B)-H(3BB)...O(1W)	0.88	1.86	2.717(4)	164.8	
N(6B)-H(6BA)...O(41)	0.88	2.40	2.984(5)	124.2	
C(1B)-H(1BA)...O(14)#2	0.95	2.50	3.289(6)	140.1	
C(2B)-H(2BA)...O(22A)#3	0.95	2.42	3.278(12)	150.6	
C(4B)-H(4BA)...O(21)	0.95	2.62	3.36(2)	134.6	
C(14B)-H(14E)...O(22)#4	0.98	2.53	3.094(18)	116.2	
C(14B)-H(14F)...O(1W)	0.98	2.50	3.326(6)	142.3	
C(15B)-H(15B)...O(24A)#4	0.95	2.19	3.040(10)	148.7	
C(28B)-H(28E)...O(13)#2	0.98	2.54	3.277(8)	132.3	
C(28B)-H(28F)...O(4WB)#5	0.98	2.34	2.991(13)	123.6	
O(1W)-H(1W1)...O(24)#4	0.820(17)	2.36(5)	2.860(18)	120(4)	
O(1W)-H(1W1)...O(23A)#4	0.820(17)	2.24(3)	2.955(8)	146(4)	
O(1W)-H(1W2)...O(4WA)	0.816(17)	1.921(19)	2.736(6)	177(6)	
O(1W)-H(1W2)...O(4WB)	0.816(17)	2.12(4)	2.788(12)	139(6)	
O(2W)-H(2W1)...O(3W)	0.806(17)	1.91(2)	2.673(6)	157(5)	
O(3W)-H(3W2)...Cl(4)	0.830(18)	2.86(4)	3.656(5)	160(8)	
O(3W)-H(3W2)...O(42)	0.830(18)	2.58(5)	3.303(7)	147(7)	
O(3W)-H(3W2)...O(43)	0.830(18)	2.17(4)	2.910(6)	148(7)	
O(4WA)-H(4W2)...O(2A)#6	0.823(18)	2.29(6)	2.965(5)	139(8)	
O(4WB)-H(4W4)...O(12)#6	0.821(19)	2.09(14)	2.735(14)	135(17)	
4					
C(2)-H(2A)...O(1)#2	0.95	2.51	3.418(3)	159.5	#1 -x+1,-y+2,-z+1 #2 x+1/2,-y+3/2,-z+1

bonding and weak intermolecular interactions with N and O atoms of a coordinate nitrate ion from another unit of the complex (-CH···O21, -CH···N5 and -CH···O22) Fig. 2(c), Table S1. Crystal packing of **1** viewed along the a-axis in Fig. S2(b).

The molecular structure of **2** is a penta-coordinated mononuclear complex. An ORTEP representation of **2** including the atomic numbering scheme is shown in Fig. 3(a). Complex **2** crystallized in the monoclinic lattice with space group $P2_1$. The X-ray diffraction data for this Cu(II) complex is given in Table 1 and the selected bond lengths and angles are summarized in Table 2.The Cu atom is five-coordinate with a ligand and two water molecules. The acethydrazone ligand, **HL**, is coordinated to a Cu(II) atom in the expected tridentate fashion, forming a five-membered chelate ring. In this molecular structure, the coordination geometry around the Cu atom is described as distorted square pyramidal (τ = 0.287) [28]. Distances of coordinated water molecules were found to be 2.304(4) Å, and 1.947(3) Å for Cu−O(2 W) and Cu−O(1 W), respectively. In addition, the Cu−O(1) carbonyl distance was found to be 2.032(4) Å. The Cu−N(1)and Cu−N(2) distances were found to be 1.942(4) Å and 2.018(5) Å, in agreement with the value of a similar copper complex [33]. Comparing the above data, the

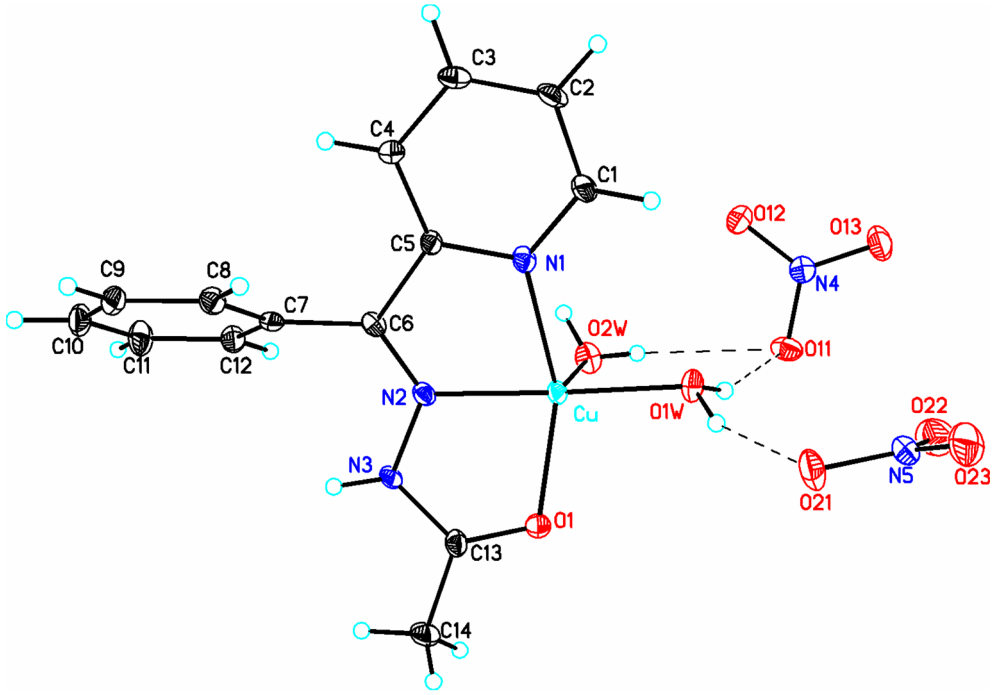

(a)

Fig. 3. (a) ORTEP structure of **2**, showing the atomic numbering scheme and 30% probability displacement ellipsoids. Dashed lines indicate O-H···O intermolecular H-bonds, (b) A view of the weak CH···π interactions for **2** (distances are in Angstroms), (c) Bifurcated and trifurcated H-bonding of **2** (see Table S1).

bond length of Cu—N(2) was shorter than any other bond length, indicating that the coordinated ability of the Cu—N(2) bond was the strongest. The bound and free nitrate anions behave as H-bond acceptors towards the aqua and acetyl moieties of the **HL** ligands resulting in the formation of a supramolecular network (Fig. 3a). In this supramolecular cluster three types of H-bond interactions are found (i) classical H-bonds between H atom of the acetyl moiety from the **HL** ligands and an O atom of a free nitrate ion. (ii) bifurcated H-bonds between the H-atom of a bound water and a bound nitrate ion and (iii) trifurcated H-bonds and weak intermolecular interactions between H atoms of the NH moiety from **HL** and O and N atoms of free nitrate ions. Details of the various types of H-bond interactions involving water molecules, nitrate anions, and NH/CH_3 groups from **HL** are shown in Fig. 3(c) (Table 3) for this complex. Thus, molecules of complex **2** are firmly connected by different types of classical H-bonds and weak H-bond intermolecular interactions with distances ranging from 1.921 to 2.659 Å. Crystal packing of **2** viewed along the a-axis in Figure S 2 (c).

The X-ray single crystal structure of **3** is a mononuclear complex. An ORTEP representation of molecular structure for **3** including the atomic numbering scheme is shown in Fig. 4(a). The X-ray diffraction data for this Ni(II) complex is given in Table 1 and the selected bond lengths and angles are summarized in Table 2. Complex **3** crystallizes with two independent molecules in the asymmetric unit in the triclinic space group $P\bar{1}$with a = 12.2765(6), b = 15.0985(8), c = 18.1055(7) Å. The Ni(II) ion is six-coordinate in a distorted octahedral geometry relative to the ideal geometry reflected by the bond angles around the centre Ni atoms ranging from 87.59(11)° to 175.09(12)°. There are two nitrogen atoms and one oxygen atom (N1, N2 and O1) from the tridentate **HL** ligand and another pair from the same ligand coordinated to the Ni atom. The coordination around the Ni atom forms an N_4O_2 chromophore. In molecule A, the basal plane of this complex is constructed by two azo nitrogen's (N2A, N5A), one pyridine nitrogen (N4A) and a carbonyl oxygen (O2A), while the apical positions are occupied by another pyridine nitrogen (N3A) and a carbonyl oxygen (O1A).The Ni-O bond distances in the axial position [2.105(2) Å and 2.106(3) Å] are clearly longer than the Ni-N equatorial bond distance (1.971(3) Å), attributed to the Jahn-Teller effect [34]. The distances of Ni(1)-N(1A), Ni(1)-N(2A) and Ni(1)-O(1A) are 2.070(3), 1.971(3) and 2.105(2) Å, which agrees with data of reported nickel(II) complexes [35]. O—H···π is the interaction of a hydrogen atom with a π-system of an aromatic ring. The classical image of an O—H···π interaction is a T shape with interacting hydrogen atoms approximately directly over the centre of the aromatic ring π_c. Measurements of distances π_c···H (dπCH), and π_c···O (dπCH) and horizontal distance (2.512 Å) were estimated (Fig. 4c). Two α angles (angles formed between the ring centre, hydrogen and donor atoms and θ (angles of approach of the vector Hπ_C to the place of the aromatic rings) were also recorded. In the present complex, two categories of O—H···π (phenyl) intermolecular interactions were measured. Type I, O—H···π interactions have the distance π_c···H (dπCH) 2.512 Å; π_c···O (dπCH) 3.242 Å and 0.2 Å and angles α, 83.61°; θ, 152.22°. Similarly, for type II interactions these values are π_c···H (dπCH) 3.210 Å; π_c···O (dπCH) 3.360 Å and 0.69 Å and angle α, 93.46°; θ, 152. Complex **3** also contains weak O—H···π (phenyl) intermolecular interactions. The existence of such interactions has been a subject of considerable study [35,36]. Crystal packing includes numerous *N*-H···O, classical intra-molecular H-bonds and a vast array of C-H···O and O-H···O weak inter-molecular interactions that contribute to a supramolecular structure, Fig. 4(d), Table 3. Crystal packing of **3** viewed along the a-axis (Figure S 2 e).

The crystal structure of **4** is a dinuclear complex**,** with an ORTEP drawing and atom numbering scheme shown in Fig. 5(a). The dimeric moiety contains two copper(II) atoms (Cu1 and Cu1A), which are symmetrically bridged by two thiocyanate anions, while the molecule of the tridentate L^- ligand (with deprotonation of the hydrazone backbone) is *N*-coordinated to each copper atom. The separation of the intramolecular Cu1 ··· Cu1A bond length is 5.5034(5) Å. The copper centres are located in a distorted square pyramidal [NNO + N + S] coordination environment as revealed by the addition parameter, τ = 0.287. The two thiocynate ligands bridge as μ-1, 3-SCN-equatorial–axial (EA) bridging ligands and bridge two Cu(II) ions with a

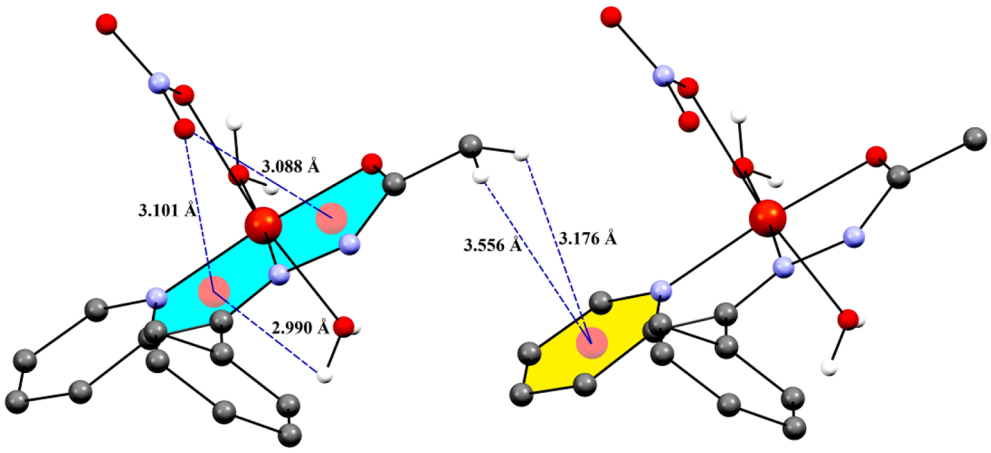

(b)

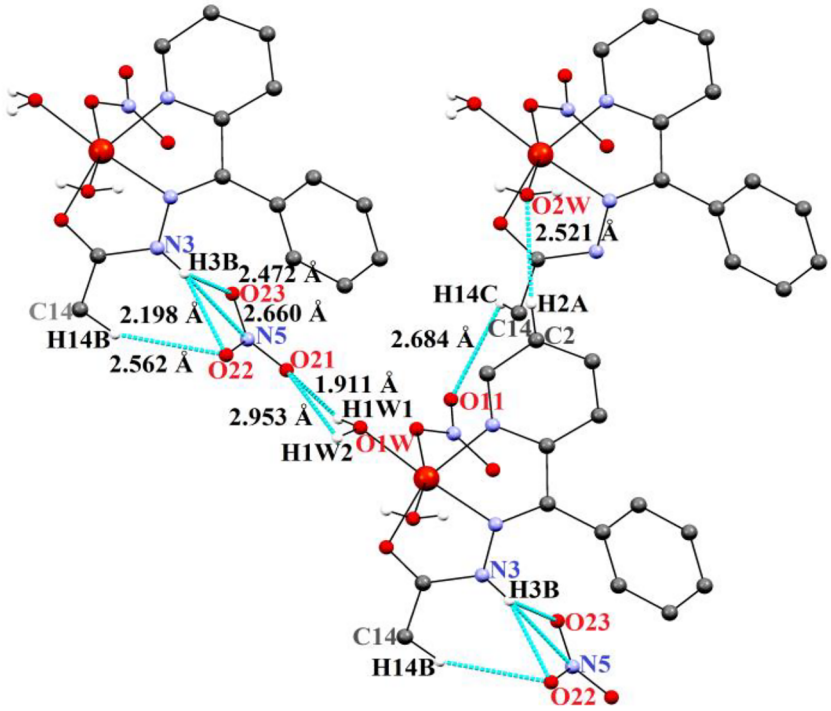

(c)

Fig. 3. (*continued*)

separation of 5.503(6) Å and result in the formation of a binuclear unit. The equatorial sites are occupied by tridentate **HL** ligands, coordinated by N1, N2, O1 and two bridging thiocynate groups coordinated in a "symmetric" end-to-end fashion (One via N and other via S) and a N donor atom of an unsymmetrical end-to-end bridge. The axial positions are occupied by a weakly bonded S- donor atom from the second thiocynate bridge, such that the Cu···S(1)$^{\#}$distance is 2.8220(7) Å (symmetry operation: 1-x + 1,-y + 2,-z + 1) and the bond angle of the axially coordinated Cu-S(1)$^{\#}$-C(15) is 97.91° The Cu-S bond distance is comparable to similar μ-1,3-SCN- bridged complexes. The Cu–N and Cu–O distances agree well with similar five-coordinate μ-1,3-SCN-bridged complexes [37]. The copper atom is 0.101 Å above the basal plane in the direction of the apex, which is usual for square pyramidal geometry. The two dimeric units are shown in Fig. 5a. The two pyridyl moieties of each of the dimeric units also show $\pi\cdots\pi$ stacking interaction distances of 3.727 Å, which is similar to $\pi\cdots\pi$ stacking interaction maximum limited distances, Fig. 5(b) [38]. Intermolecular hydrogen bonding observed in between C—H of aryl group and O atom of HL ligand Fig. 5(c). Crystal packing is influenced by weak C—H…O intermolecular interactions forming chains along [0 1 0], Fig. S2 (d). This stacking interaction leads to the formation of a three-dimensional supramolecular structure. The basal coordination positions are held by three nitrogen atoms (N1, N2 and N5) and one oxygen atoms (O1). The distances of Cu–N (1), Cu–N (2) and Cu–N (5) are 2.016(2), 1.927(2) and 1.925(2) Å, in agreement with the value of a similar bridged Cu(II) complex [37].

3.4. Electronic spectra

The electronic spectra of the ligand and four complexes were

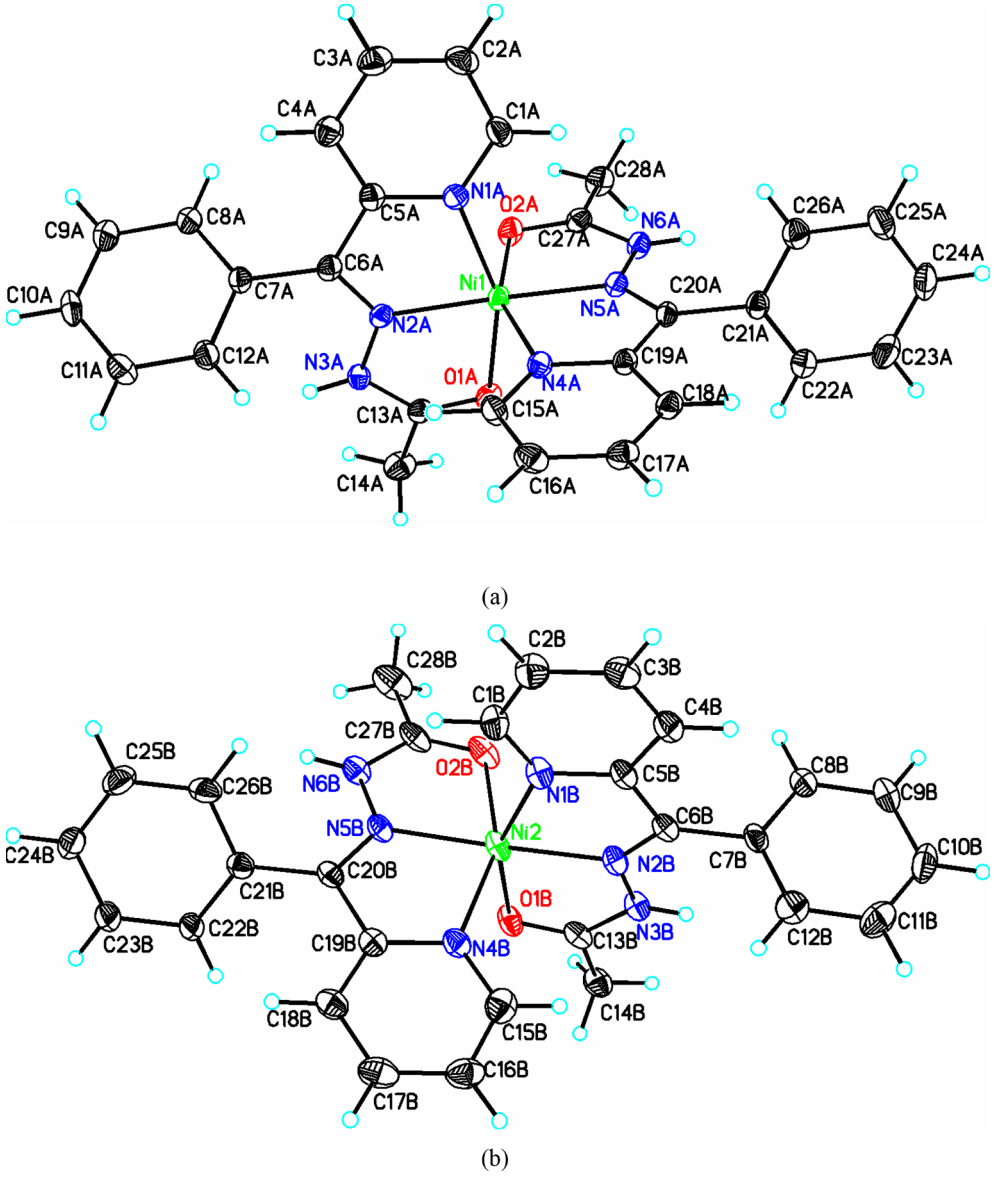

Fig. 4. (a) ORTEP structure of molecule **3a**, showing the atomic numbering scheme and 30% probability displacement ellipsoids. (b) ORTEP structure of **3b**, showing the atomic numbering scheme and 30% probability displacement ellipsoids. (c) A view of the weak H···π interactions (dashed lines) for **3,**; (d) A view of an O—H···π interaction is a T shape with interacting hydrogen atoms approximately directly over the centre of the aromatic ring π_c. (e) Bifurcated and trifurcated H-bonding and weak intermolecular interactions for **3**, see Table S1.

recorded in DMSO at ambient temperature. The ligand (**HL**) shows two bands, including an intense band at 303 nm and a weak band found near 382 nm. These may be assigned to π -π^* and n-π^* electronic transitions, respectively. The electronic spectra of complex **1** also indicate a d-d ligand-to-metal band transition at 682 nm. In addition, a charge transfer band at 380 nm and one π–π^* band at 300 nm are observed. Ligand **HL** forms stable five-coordinate distorted square-pyramidal complexes with Ni(II), which is not prone to add a sixth donor group. A coordination number of five is relatively rare for Ni (II),which much more often tends to form high-spin octahedral or low spin square-planar complexes [39]. In five-coordinate nickel(II) complexes special steric properties are operative, therefore, crowding around the metal ion is large enough to prevent a sixth coordination site [40]. The electronic spectrum of complex **3** is typical of a distorted octahedral complex. This complex exhibits bands near 980(ν_1), 832(ν_2), and 585(ν_3) nm [41], corresponding to the spin allowed d-d transitions of $^3A_{2g}\rightarrow{}^3T_{2g}$(F) ($\nu_1$), $^3A_{2g}\rightarrow{}^3T_{1g}$(F) ($\nu_2$) and $^3A_{2g}\rightarrow{}^3T_{1g}$(P) ($\nu_3$), respectively (Fig. 6). These electronic transitions agree with the literature values for nickel(II) octahedral complexes [41]. Both copper (II) complexes show broad bands at 681 nm and 684 nm for **2** and **4,** respectively (Fig. 6a). In addition, charge transfer bands are observed at 380 nm and 378 nm in complexes **2** and **4,** respectively (Fig. 6b). Strong absorption bands in regions around 300 nm are also due to n-π^* and π -π^* transitions. Such electronic transitions indicate square-pyramidal geometry.

3.5. Electrochemical properties

The electrochemical behavior of complexes **1–4** was explored using cyclicvoltammetry (CV) and differential pulse voltammetry (DPV) in DSMO solutions containing 0.1 M tetrabutyl ammonium perchlorate, $[(Bu)_4N]ClO_4$. Both nickel(II) complexes **1** and **3** show two redox waves. One representative CV for the nickel(II) complexes is shown in Fig. 7a.The potentials of the Ni^{II}/ Ni^{I} and Ni^{I}/ Ni^{II} redox couples for these two complexes are −0.147 V and −0.389 V for **1** and −0.027 V and −0.771 V for **3**. The complexes containing pyridine donor atoms

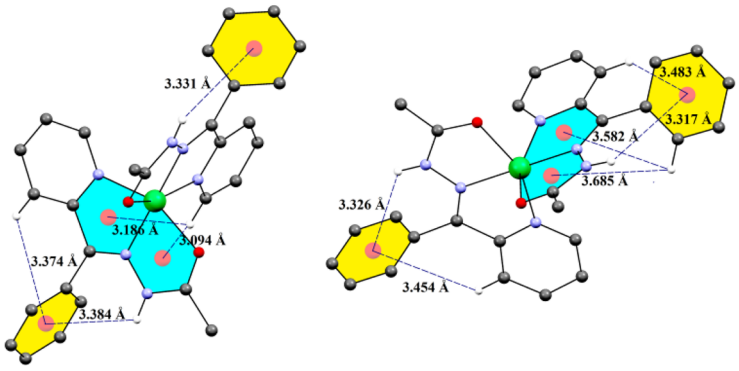

(c)

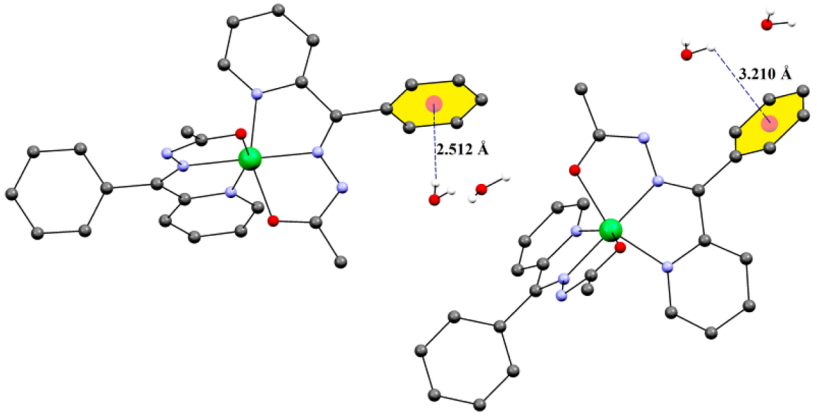

(d)

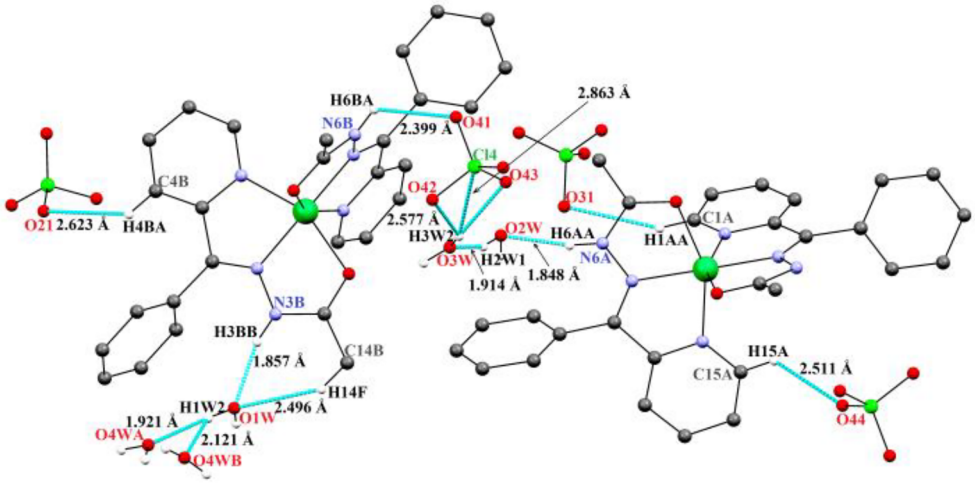

(e)

Fig. 4. (*continued*)

are insufficient for stabilization of Ni^{I} [42]. Steric and electronic factors appear to be necessary for the ability of nitrogen ligands to stabilize the Ni^{I} oxidation state. Additionally, complexes having ligands with long pendent arms are expected to form thermodynamically weaker complexes with Ni^{II} than their short analogues [43], resulting in positive or less negative reduction potentials for the redox couples [44]. Similar observations were observed from the DPV experiments. Differential pulse voltammograms of these complexes showed two reduction waves similar to the CV experiment. The CV of the five-coordinate complexes reported in the literature showed similar two redox waves in the cyclic voltammogram of five-coordinate copper(II) mononuclear complex **2,** and also shows similar behavior to that for nickel(II) mononuclear complexes **1** and **3.** A μ-1, 3 thiocynate bridged complex has also showed two reduction waves of two metal centers, corresponding to two separate couples (1) and (2) in:

$$Cu^{II}Cu^{II} \rightleftharpoons Cu^{II}Cu^{I} \quad (1)$$

$$Cu^{II}Cu^{I} \rightleftharpoons Cu^{I}Cu^{I} \quad (2)$$

But, both reduced copper(II) centers oxidized at the same potential. Two reduction waves are observed in the DPV (Fig. 7b)

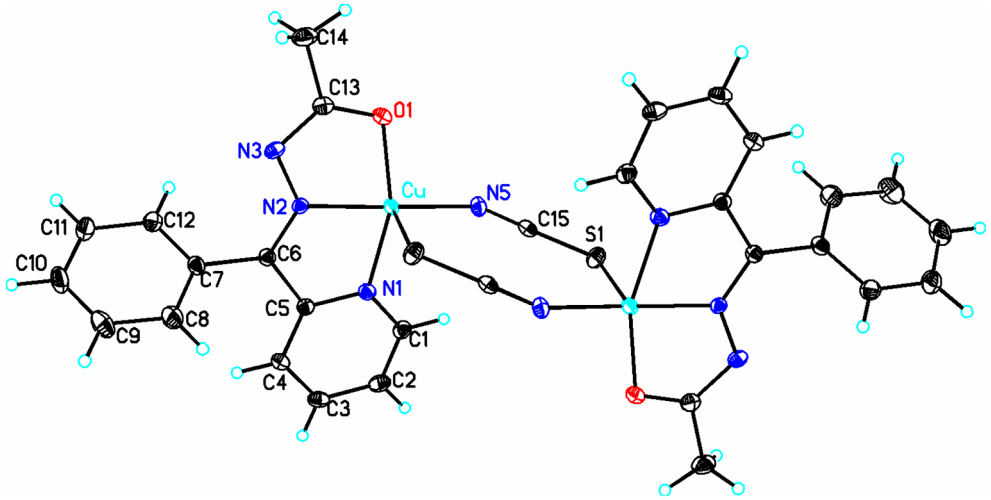

(a)

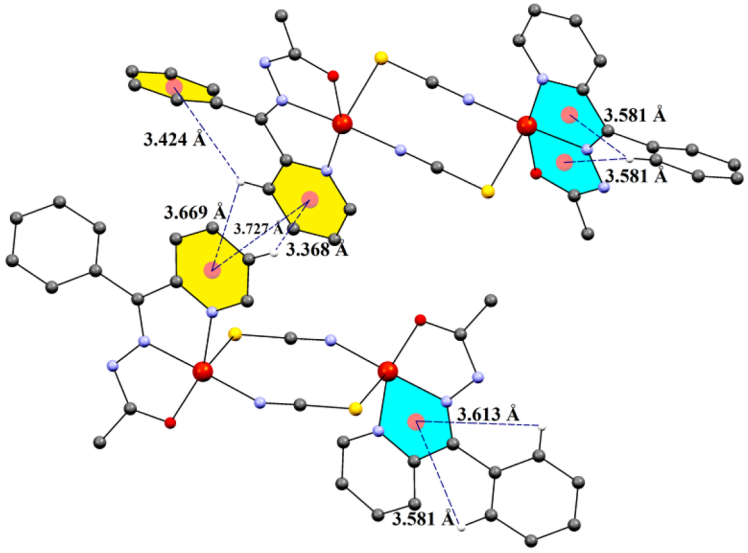

(b)

Fig. 5. (a) ORTEP drawing of **4**, showing the atomic numbering scheme of the asymmetric unit and 30% probability displacement ellipsoids. (b) A view of the weak C—H···π and $\pi\cdots\pi$ intermolecular interactions in **4**.

3.6. Quantum chemical analysis

Quantum Chemical calculations have been performed on complexes **1–4** in order to examine their corresponding theoretical geometrical parameters (bond lengths and bond angles). These results are in good agreement with the experimental parameter values (Table 2) and have been evaluated for comparison of the bond lengths and bond angles between the quantum chemical optimized and single crystal X-ray determined structures of **HL** and complexes **1–4.** The geometries of complexes **1–4** were fully optimized by the DFT/B3LYP method. The geometry optimized structures of **HL** and complexes **1–4** are represented in Fig. S3. The theoretical model was used for the DFT calculations and theoretical model are also represented in Fig. S3. Selected highly occupied molecular orbitals (HOMO) and lowly unoccupied molecular orbital (LUMO) structures for **1–4** are shown in Fig. 8. The energy gap, ΔE, is a very important parameter for biological chemical activity [45]. From this, one can gain insight on the way that the molecule interacts with other species. Hence, they are called the frontier molecular orbitals. The HOMO is the orbital that primarily acts as an electron donor and the LUMO is the orbital that largely acts as the electron acceptor [46]. The HOMO-LUMO energy gap is 2.1051 for **1**, 3.8662 for **2**, − 0.3975 for **3** and 2.0910 eV for complex **4**. The value of the energy gap in the contour plots reflects upon its catalytic activity [47]. The HOMO-LUMO energy gap for complex **3** is the lowest, indicating a relationship with the highest SOD data and may be considered as an active centre for the antioxidant reagent [48]. The corresponding spin-density representations for **1–4** are shown in Fig. 9. The quantum chemical spin density plots for complexes **1–4** are shown in Fig. 9. Fig. 9 illustrates the spin densities for ground state S = 1/2 in complexes **1–3** and S = 0 in complex **4.** The spin densities around the copper centres resemble an $d_{x^2-y^2}$ orbital with a contribution from d_{z^2}. The coordinated copper and donor atoms (N and O) of the coordinated tridentate Schiff base carry the spin densities with the same sign due to the spin-delocalization effect. In complexes **1–3** the π-conjugated hydrocarbon also carry spin density due to a spin-polarization mechanism [49], whereas in binuclear complex **4** the π-conjugated hydrocarbon network does not carry spin density. In binuclear complex **4** the bridging moieties also carry spin density Fig. 9(d).

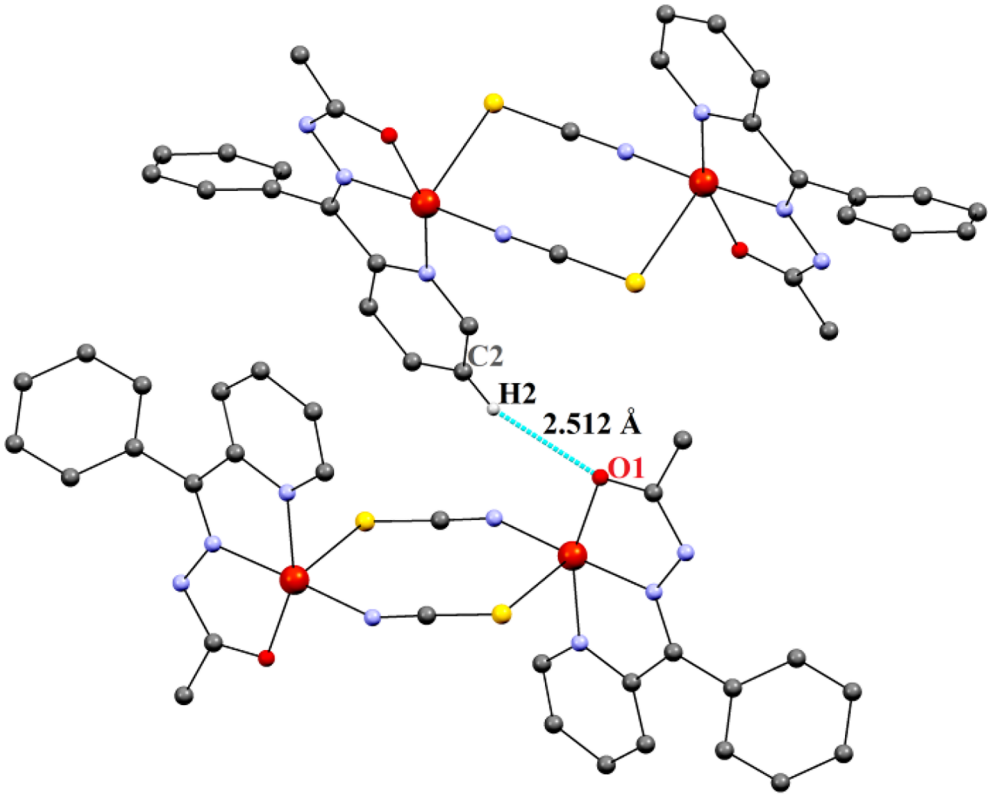

(c)

Fig. 5. (*continued*)

3.7. Magnetic properties

The magnetic susceptibility data for copper(II) mono and binuclear complexes **(2** and **4)** were collected and evaluated**.** A magnetic susceptibility measurement for mononuclear complex **2** was carried out at room temperature whereas for binuclear complex **4,** susceptibility data were measured in the temperature range 300–3 K. The temperature dependence of the $\chi_M T$ product for complex **4,** with χ_M being the molar magnetic susceptibility per Cu^{2+} ion and is shown in Figure S 4. The experimental $\chi_M T$ value is 0.37 ± 0.01 cm^3 K mol^{-1} in the 2–300 K temperature range and, therefore, indicated no significant magnetic interactions between the Cu^{2+} ions. Never-the-less, a fit of the magnetic data using the Bleany-Bowers equation ($H = -J S_1S_2$), considering the molar magnetic susceptibility per dimer, was carried out. The values obtained from this fit, $g = 1.99$ and $J = 0.08$ cm^{-1}, confirm that the magnetic interactions between metal centres in this compound are almost negligible. The magnetic behavior observed for **4** is similar to that of most *bis*(μ-NCS) copper (II) complexes, in which only small or negligible magnetic interactions are observed [50]. The weak antiferromagnetic coupling ($J = 0.08(1)$ cm^{-1}) is obviously due to the larger distance [5.5034(5)] among copper(II) centres. Two similar dinuclear copper(II) complex with Schiff base blocking ligand bridged by end-to-end thiocyanate is reported [51]. The structural and magnetic parameters for end-to-end bridged copper(II) complexes with tridentate NNO donor Schiff bases given in Table 4.

3.8. EPR spectroscopy

X-band EPR spectra of the copper(II) complexes have been measured in the polycrystalline state and in DMSO solution (3.0 mmol) at RT and 77 K, respectively. EPR spectroscopy is a useful technique for discriminating between mono-and binuclear copper(II) species. The X-band EPR spectrum of **2** in the polycrystalline state at room temperature (RT) is shown in Fig. 10.

The $\Delta M_s = 1$ transition at RT shows two broad signals at 2840G and 3085G, which are characteristic $\Delta M_s = 2$ transitions. Such EPR spectral features, confirming two spin-coupled, axially symmetric copper(II) centres(singlet–triplet transitions) with $\Delta M_s = 1$ and $\Delta M_s = 2$ transitions [52]. However, copper hyperfine spectral features are not visible in either $\Delta M_s = 1$ and $\Delta M_s = 2$ regions. The strong half-field signal ($\Delta M_s = 1$) at ≈1620G [52] identifies from coupling between S = 1/2 metal ions. Such spectral features are due to intermolecular magnetic dipole interactions and double/triple strand H-Bonding between acetyl oxygen and coordinated water molecules, as well as nitrate ions, which are also responsible for the above spin-spin interactions, in agreement with the X-ray structure. This EPR spectrum seems to be an “axial” spectrum with the apparent two g- values ($g_\parallel = 2.201$ and $g_\perp = 2.069$), $g_e = 3.74$ and $D = 0.026$ cm^{-1}. The value of D is similar to other known complexes [53].The geometry parameter, G, a measure of exchange interaction between two paramagnetic centres, was estimated [52]. If G >4, the interaction is negligible and G < 4 indicates an exchange interaction. For complex **2**, the value of G = 2.978, indicates a strong exchange interaction in the poly crystalline state. Such EPR spectral features following in the polycrystalline state are shown to be due to coordinated water molecules and the presence of anionic nitrate ions to form intra and intermolecular H-bonds. The frozen DMSO solution shows two kinds of $g_\parallel$ features, i.e. two kinds of copper nuclei with different structures, are present in solution. The frozen solution spectrum exhibits the usual line shape for the mononuclear copper(II) complex with $g_\parallel > g_\perp > 2.03$, showing axial symmetry [53]. The low temperature (77 K) X-band EPR solution spectra of both copper(II) complexes (**2** and **4**) are almost similar and typical of magnetically coupled mononuclear copper(II) complexes [54]. Six resolved hyperfine lines observed in the $g_\parallel$ region in the low temperature spectrum of **2**,

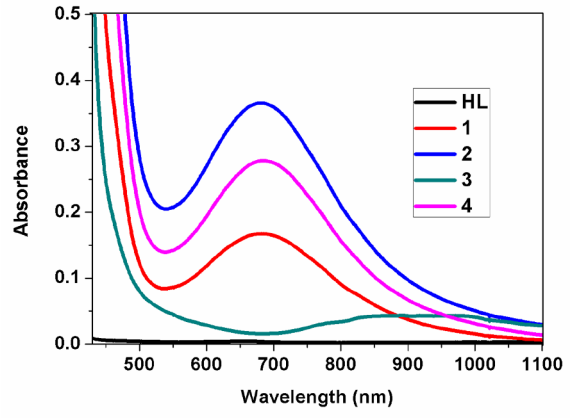

(a)

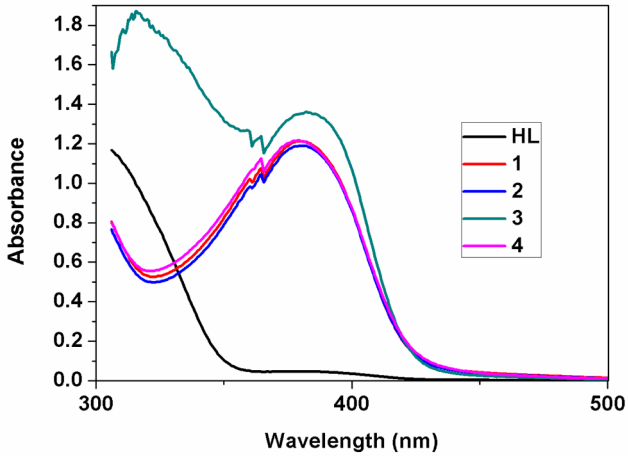

(b)

Fig. 6. (a) UV–visible spectra of copper(II), (**2** & **4**) and nickel(II) (**1** & **3**) complexes in 6.0 × 10^{-5} M DMSO solution. UV–visible spectra of copper(II) (**2** & **4**) and nickel(II) (**1** & **3**) complexes in 3.0 × 10^{-3} DMSO solution.

indicate the presence of more than one copper nuclei. Therefore, these nuclei interact with each other in solution and show exchange interaction in the system. In the case of complex **4**, the polycrystalline structure collapses in DSMO where mononuclear units are formed (Fig. S5).

The low temperature spectrum of complex **4** is characterized by axial symmetry with unpaired electrons in the $d_{x^2-y^2}$ orbital. The binuclear complex breaks through a C···S bond with the formation of a discrete [Cu(L)$_2$(NCS)] species($g_{\|}$ = 2.218, $g_{\perp}$ = 2.069 and $A_{\|}$ = 148×10^{-4} cm^{-1}). The formation of a mononuclear species after the dissociation of the polycrystalline sample in a DMSO like coordinating solvent has been reported for some other known thiocynate bridged copper(II) complexes. [55] A polycrystalline sample of thiocynate bridged complex **4** was measured at room temperature. The X-band EPR spectrum is characterized by rhombicity and three g- values (g_x = 2.217, g_y = 2.130 and g_z = 2.077) with the observed trend g_x>, g_y > and g_z> g_e. In this EPR spectrum, no resonances bellow 2700G and above 3300G were observed. In such a spectrum, the ground state can be described as a linear combination of $d_{x^2-y^2}$ and d_{z^2} orbitals [52]. The rhombicity parameter, R = (g_y-g_z/g_x-g_y) is indicative of the predominance of a $d_{x^2-y^2}$ and d_{z^2} orbital. If it is R< 1, a greater contribution to the ground state arises from d_{z^2} and if it is R< 1 the greater contribution to the ground state arises from the $d_{x^2-y^2}$ orbital [52]. The value of R of this thiocynate bridged complex is 0.6, which confirms the distorted square pyramidal geometry around each copper(II) center with a $d_{x^2-y^2}$ ground state orbital [56].

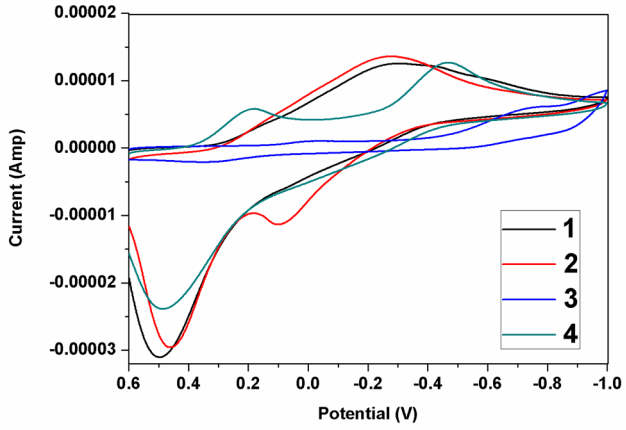

(a)

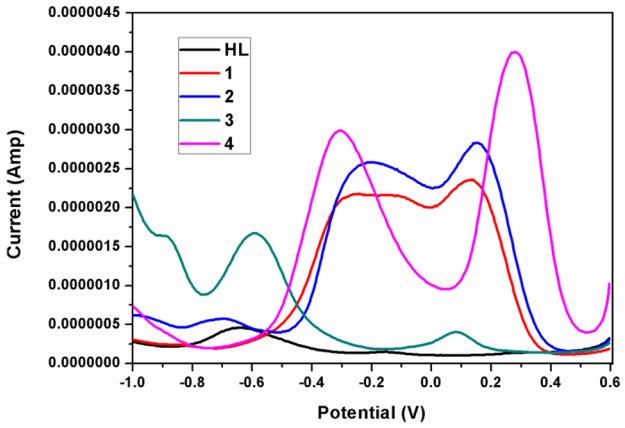

(b)

Fig. 7. (a) Cyclic voltammograms for **1–4** in DMSO at an Ag/AgCl electrode with a scan rate 100 mV $s^{-1}$and a temperature of 25 °C. (b) Differential pulse voltammogram (DPV) for **HL** and **1–4** at room temperature using a scan rate 20 mV s^{-1} in DMSO. The pulse amplitude is 50 mV.

3.9. Cytotoxicity assay

The anticancer activities of synthesized complexes toward human IMR 32 (neuroblastoma), MCF7 (breast cancer), HepG2 (hepatocellular carcinoma), L132 (lung cells) cell lines have been explored by MTT (3-(4, 5-dimethylthiazol-2-yl)-2,5-diphenyltetrazoliumbromide) assay. The MTT assay is a convenient method to examine the *in vitro* anticancer activity of compounds against cancer cells [57]. Percent inhibition of each concentration of the compounds was calculated using the formula, % inhibition concentration = 100 – (OD of treated/OD of Control)*100. A graph was plotted using Origin software and IC_{50}values for each compound were calculated (Table 5). On IMR 32 cells, the cytotoxicity of **3** was measured to be significant (0.0669 μM) amongst the other compounds. For cytotoxicity on IMR 32 cells, **1**(0.1373 μM) was found to be second on an effective synthesis. The IC_{50} value of cytotoxicity exposure, on MCF 7 cells, was highest with **3** (0.0745 μM) and that was followed by **1** (0.1096 μM). The same trend of inhibition by compounds **3** (0.0553) and **1**(0.1007 μM) was observed on cells of HepG2 (Fig. 11). It was evident that complex **3** exhibited higher cytotoxicity than the other compounds against all the cell lines.

3.10. Gene expression study

Derived cytotoxicity of different compounds represents a

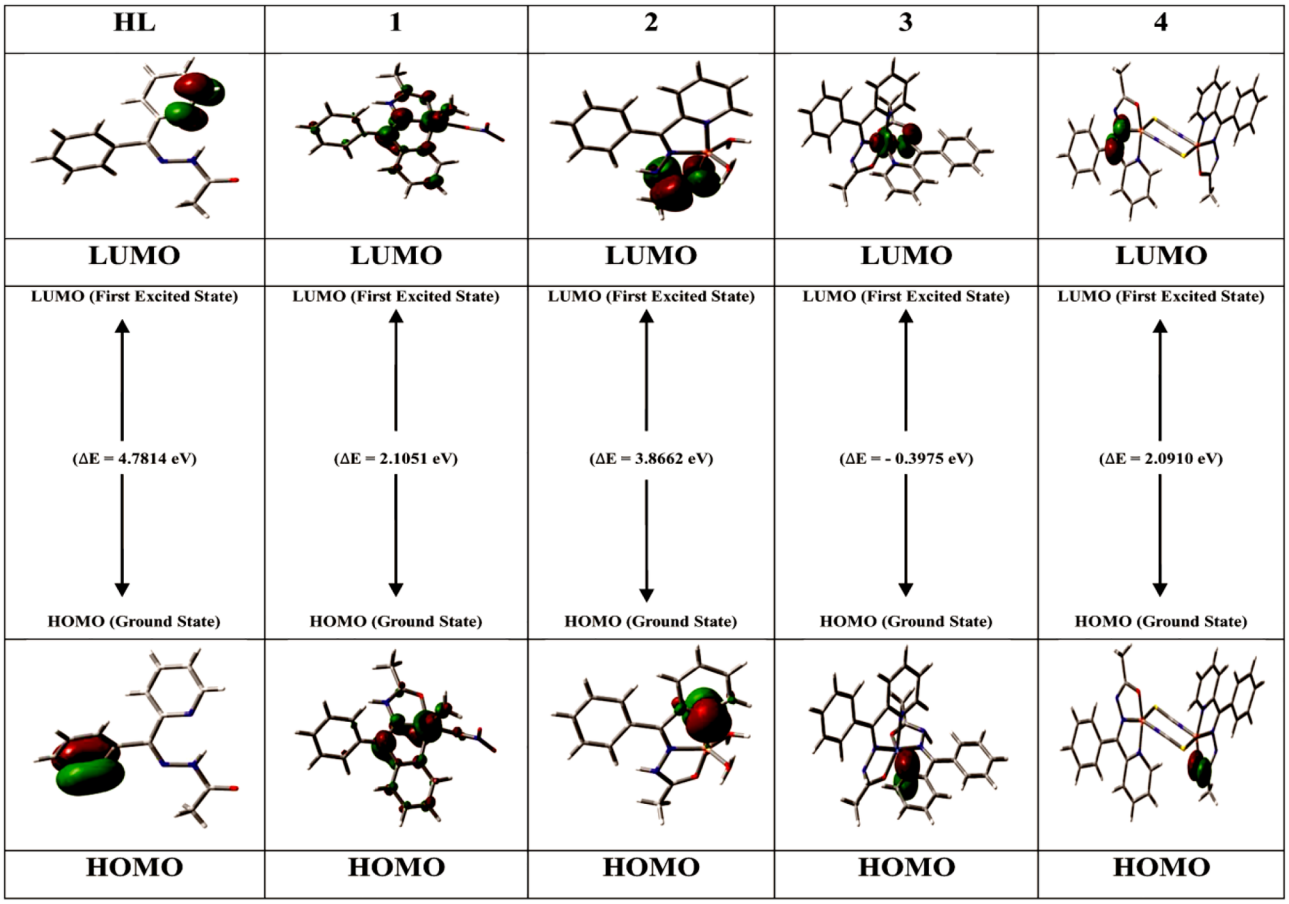

Fig. 8. HOMO-LUMO electron distribution plots and ΔE energy gap calculations (eV) for complexes **HL** and **1**–**4**.

mitochondrial metabolic state. These results were analysed in accordance with the earlier reported results [58]. Further, to prove that the compounds disturb mitochondrial homeostasis and escort cell death, we have performed mitochondrial specific gene expression analysis. Bax and Bcl-2 genes were selected for the study. Relative expression of these genes was observed using β actin as the housekeeping gene. Profound expression of Bcl-2 was observed in the cancerous cells and that is required for survival of cancerous cells. The phenomenon of a low level of Bax was also observed to support restless function of the mitochondria for cancer cell survival and proliferation. An altered phenomenon was observed during treatment given by **1** and **3** (selected based on the cytotoxicity result). The level of Bcl-2 was observed fold decreased due to 24 h of **1** and **2** treatments (Fig. 12). The fold expression for Bax was observed to be higher in the cancerous cells of IMR32. Compound **1** was observed to be more effective than **2**.

3.11. AO/EB staining

To observe cell death characteristics, acridine orange and ethidium bromide staining was performed. Dual staining provides information of necrotic and programmed cell death induced by the given treatment of any compound. Acridine orange gives a stain to viable cells whereas ethidium bromide gives a stain to necrotic cells. Cells undergone for programmed cell death were stained by both the stains. IMR 32 cells were incubated for 20 min in dual staining after 24 h of treatment. These cells showed characteristics of apoptosis (Fig. 13).The apoptotic feature was observed as a green and red dual fluorescence emitted by a single cell.

The a neoplastic activity of **3** can be attributed to a stronger DNA binding ability by deeper insertion between two DNA base pairs via an activating apoptotic inducing factor, consequently leading to cell death. The morphological examination of these cells along with the dual staining results showed apoptotic characteristics. This phenomenon is also supported by a lower expression of Bcl2 and a higher expression of Bax. Potential anti-cancerous activity of Cu complexes has also observed by Hussain et al. [59]. They proposed that the antiproliferative activity of a copper compound is due to its activity on Cox-2. In their studies, a Cu complex works as Cox-2 inhibitors and leads to cell death in MCF 7 cells. Our outcomes are also supported by the results of Scarpellini and co-workers [60]. According to their conclusions, copper complexes can promote phosphate diester hydrolysis and DNA damage that induce apoptosis in cancerous cells. Copper complexes catalytically cleave target DNA base pairs in the absence of a reductant at multiple positions of a nucleotide [61]. The apoptotic effect of a nickel compound was also observed by Bal-Demirci et al. [62]. They have suggested that caspase 3 activation is the key responsible factor to induce cell death in a cell.

3.12. Antioxidant SOD activity

All the synthesized mono and binuclear complexes (**1**–**4**) show catalytic activity towards the dismutation of superoxide anions. The antioxidant SOD activities of complexes (**1**–**4**) were determined by the NBT assay method using alkaline DMSO as the source of $O_2^{\bullet-}$. The concentration needed to yield 50% inhibition of the reduction of NBT known as IC_{50}, was calculated. [23b] In this method $O_2^{\bullet-}$ generated by alkaline DMSO reduces yellow nitro blue tetrazolium (NBT) to the blue formazan, which is measured spectrophotometrically at 560 nm. Therefore, compounds can compete with NBT for oxidation of the generated $O_2^{\bullet-}$. Scavengers (compounds) are able to inhibit the

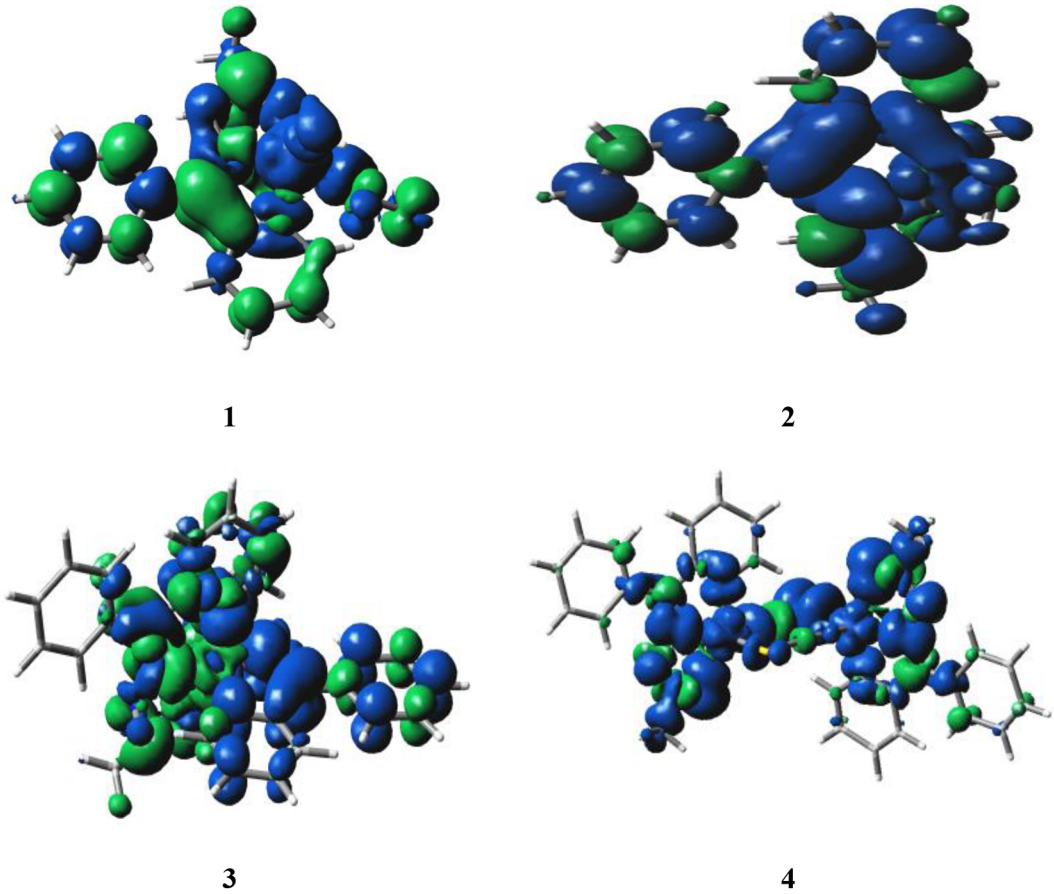

Fig. 9. Quantum chemical investigated spin density plots for complexes **1–4.**

Table 4
Structural and magnetic parameters for end-to-end bridged copper(II)complexes with NNO donor Schiff bases.

Complex	Cu–Cu Å	J (cm^{-1})	Reference
$[Cu(L)NCS]_2$ **2**	5.8629(6)	−1.71 (1)	60(a)
$[Cu_2(L)2(\mu\text{-}1,3\text{-}NCS)_2].H_2O.DMF$ **2**	5.6382(4)	−0.6 (1)	60(b)
$[Cu_2(\mu\text{-}SCN)_2(L)_2]$ **4**	5.503 4 (5)	0.08 (1)	This work

Fig. 10. EPR spectra of complex **2** in the polycrystalline state (RT) and in DMSO solution at liquid nitrogen temperature (LNT), inset half-field at RT and LNT.

formation of blue formazan. The catalytic rate constant (k_{McCF}) was also evaluated for these complexes. The kinetic catalytic constant k_{McCF} was calculated by the formula kMcCF = k_{NBT} ×[NBT] / IC_{50}, where $k_{NBT} = 5.94 \times 10^{-4}$ (mol L^{-1})$^{-1}$ s^{-1} is the second order rate constant for NBT [23b]. The kinetic catalytic constant (k_{McCF}) of **1–4** are 7.39×10^{-4} (mol L^{-1})$^{-1}$ s^{-1}, 20.79×10^{-4} (mol L^{-1})$^{-1}$ s^{-1}, 5.28×10^{-4} (mol L^{-1})$^{-1}$ s^{-1} and 13.86×10^{-4} (mol L^{-1})$^{-1}$ s^{-1}, respectively. The values of catalytic rate constants for the superoxide disproportiation constant (k_{McCF}) clearly indicate that the present complexes can be used as an antioxidant superoxide scavenger. The metal(II) mononuclear **(1–3)** and dinuclear **4** complexes in this study exhibit antioxidant catalytic activity towards the dismutation of antioxidant superoxide anions. The antioxidant SOD activity data, IC_{50} and SOD activity, are summarised in Table 6 along with recently collected values of similar complexes [63]. On the basis of antioxidant observations, it is clear that complexes **1–4** are more efficient antioxidant than vitamin c, which is the standard for antioxidant superoxide dismutase [63c].

The values of antioxidant activity data of other similar complexes are also shown in Table 6. The difference in activity data for these complexes could be ascribed due to the evident discrepancy in the structures among them. The observed term of activity was also justified

Table 5
Percent Inhibition concentration 50 (IC_{50}) of various synthesized compounds **HL** and **1–4.**

S.No	Compounds	IC_{50} value (μM)			
		IMR32	MCF7	L132	HepG2
1.	**HL**	0.221 ± 0.0237	0.275 ± 0.0397	0.274 ± 0.0397	0.185 ± 0.0265
2.	**1**	0.137 ± 0.0052	0.111 ± 0.0052	0.265 ± 0.0052	0.101 ± 0.0405
3.	**2**	0.144 ± 0.0057	0.121 ± 0.007	0.150 ± 0.007	0.129 ± 0.0437
4.	**3**	0.067 ± 0.0087	0.075 ± 0.0064	0.099 ± 0.0064	0.055 ± 0.0084
5.	**4**	0.634 ± 0.0309	0.843 ± 0.113	0.986 ± 0.113	0.693 ± 0.0968
6.	Cisplatin	35.87 ± 2.13	26.4 ± 1.67	29.5 ± 2.26	31.4 ± 2.5

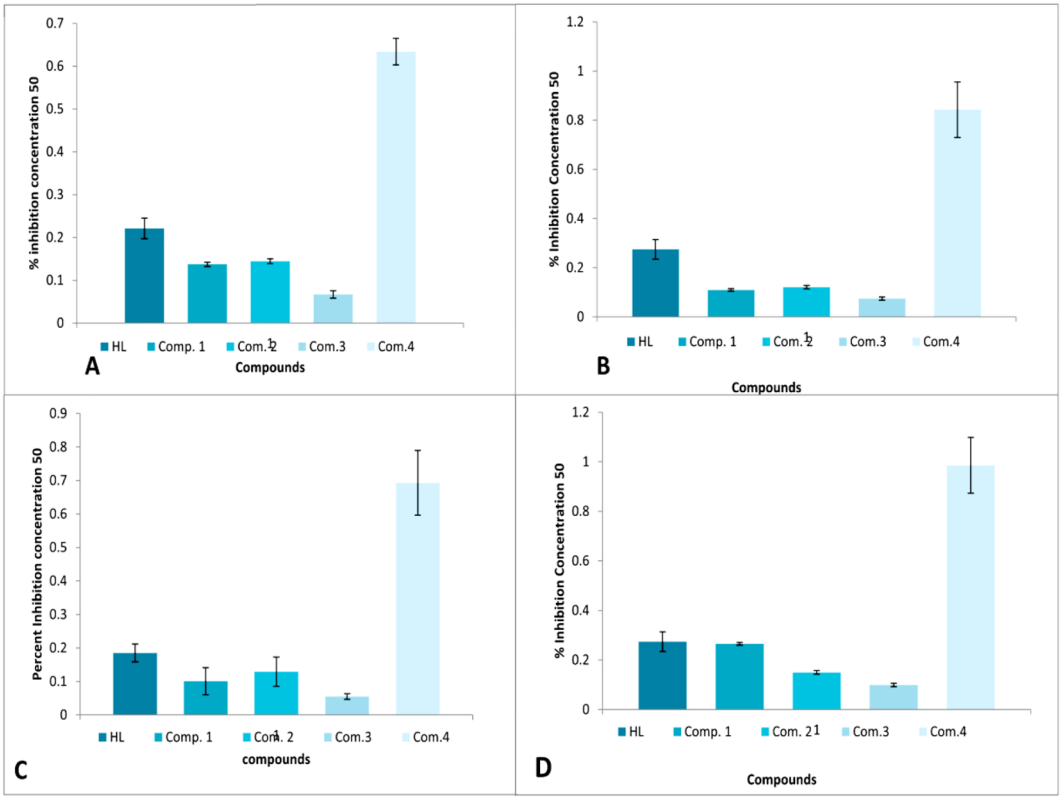

Fig. 11. Cytotoxicity represented as IC_{50} values on different cell lines after 24 h of compound exposure A. IMR32, B. MCF 7, C. HepG2, D. L132.

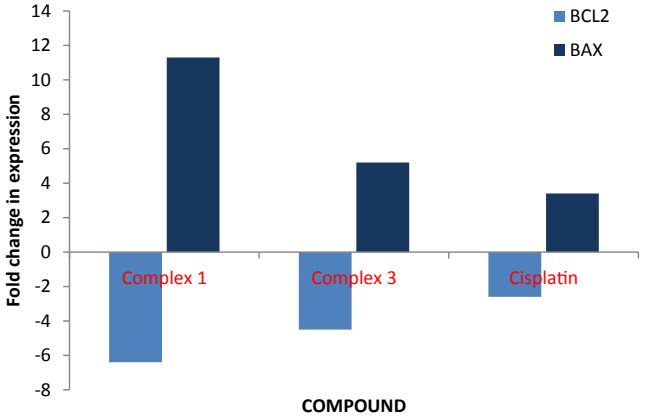

Fig. 12. Gene expression study after 24 h of treatment with compounds **1** and **3.**

from the values of the HOMO-LUMO energy gaps in the frontier molecular orbitals [46]. Complex **3** shows the lowest energy gap (Δ E = -0.3975 eV). The HOMO-LUMO energy gaps showing highest activity for complexes **2, 4** and **1** are also showed SOD data. Binuclear complex **4** dissociates in the solvent and therefore gives similar SOD data to that of the five-coordinated mononuclear complex. The lowest activity data is shown by complex **3,** with a minimum ΔE value, due to a lack of water or of any solvent in the coordination sphere of the metal. The catalytic mechanism is illustrated in Scheme 3. In step (i) the inner sphere electron transfer takes place in between the coordinated $O_2^{\bullet-}$ and the copper(II) centre of the complex. The concomitant cleavage of the copper-H_2O bond is assisted by protonation of the solvent and the oxygen molecule is subsequently released. Re-oxidation of Cu^{I} to Cu^{II} by the second $O_2^{\bullet-}$ molecule reforms the bond with H_2Oalong with transfer of a proton to the peroxide ion in step (ii).

4. Conclusion

The whole manuscript can be concluded in structural characterization, magnetic studies and biological studies of two new copper(II) complexes ([Cu(HL) $(H_2O)_2$]2NO_3 **2,** and [Cu_2- μ-$(SCN)_2(L)_2$] **4**), and two new nickel(II) complexes **(**[Ni(HL)$(NO_3)(H_2O)$]NO_3 **1,** and [Ni $(HL)_2$]2ClO_4 **3).** Complex **4** is an end-to-end equatorial–axial thiocynate bridged complex. The magnetic susceptibility data of **4** shows slightly negligible magnetic interactions. The equatorial–axial disposition of the thiocynate bridge minimizes the antiferromagnetic component *J* (J = 0.08 cm^{-1}). In this complex the dependence of the bond angles and bond lengths suggests, it to be a consistent model to explain sign and magnitude when the magnetic interaction is a weak antiferromagnetic effect for the thiocynate bridged system. Comparison of the structures and the results of magnetic properties with previously related reported dinuclear copper(II) complexes with NNO donor Schiff bases reveals that the magnetic exchange in systems is governed by combined effects of many parameters. The highest antioxidant activity is shown in complex **2.** This is well supported by quantum chemical theoretical data (HOMO-LUMO and energy gaps). The classical image of an O—H···π interaction is a T shape with interacting hydrogen atoms approximately directly over the centre of the aromatic ring π_c. Measurements of distances π_c···H (dπCH), and π_c···O (dπCH) and the horizontal distance (2.512 Å) were estimated. The crystal packing of the structures of these new complexes is stabilized by H-bonding, weak intermolecular interactions, CH···π and π···π interactions. The electrochemical data (CV and DPV) of these complexes show M^{II}→M^{I} reduction. Electronic structures and spectral features are explained and supported by quantum chemical studies. Finally, the antioxidant super oxide dismutase activity measurements show that the complexes behave as superoxide dismutase mimics. All the complexes are highly active and have potential to induce programmed cell death on treatment to cancerous cell.

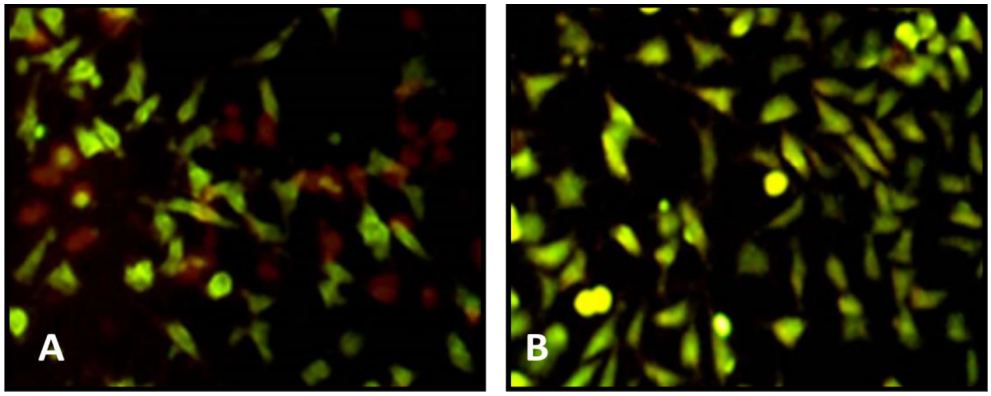

Fig. 13. Images of acridine orange and ethidium bromide staining to observed cell death patterns in IMR 32, A). **1**, B) **3.** (For interpretation of the references to colour in this figure legend, the reader is referred to the web version of this article.)

Table 6
The antioxidant SOD activity, IC_{50} values and first order kinetic catalytic constants for complexes **1–4**.

Complex	IC_{50} (μmol)	SOD activity (μmol^{-1})	$k_{McCF}(mol\ L)^{-1}s^{-1}) \times 10^4$	Reference
$[Ni(HL)(NO_3)\ (H_2O)]NO_3$ **1**	45	22.22	7.39	This work
$[Cu(HL)\ (H_2O)_2]2NO_3$ **2**	16	62.50	20.79	This work
$[Ni(HL)_2]2ClO_4$ **3**	63	15.87	5.28	This work
$[Cu_2\ \mu(SCN)_2(L)_2]$ **4**	24	41.66	13.86	This work
Vc	852	1.17	0.39	[63c]
$[Cu(idb)H_2O](NO_3)_2$	1.02	980.40	–	[63f]
$[Cu(idb)H_2O](ClO_4)_2{\cdot}H_2O$	0.84	1190.50	–	[63f]
$[Cu(L^1)(NO_3)_2(4,4\text{-bipy})]$	30	33.33	11.08	[63g]
$[Cu(L^1)(H\ L^1)]ClO_4.1/2H_2O$	25	40.00	13.30	[63g]
$[Cu(L^1)(H\ L^1)][Cu(L^1)(H\ L^1)](ClO_4)_2{\cdot}H_2O$	55	18.18	6.048	[63g]
$[Cu(L^1)(NO_3)\ (\mu\text{-2-aminopyrazine})Cu(L^1)(NO_3)_2].2H2O$	15	66.67	22.17	[63g]
$[(L^1)Cu(\mu\text{-}CH_3COO)_2Cu(L^1)]$	35	28.57	9.50	[63k]
$[(L^1)Cu(\mu\text{-}NO_3)2Cu(L^1)]$	26	38.46	12.79	[63k]

*HL^1/L^1 = N'-[(E)-phenyl(pyridin-2-yl)methylidene]benzohydrazide, idb = Bis-(benzimidazol-2-ylmethyl)amine.

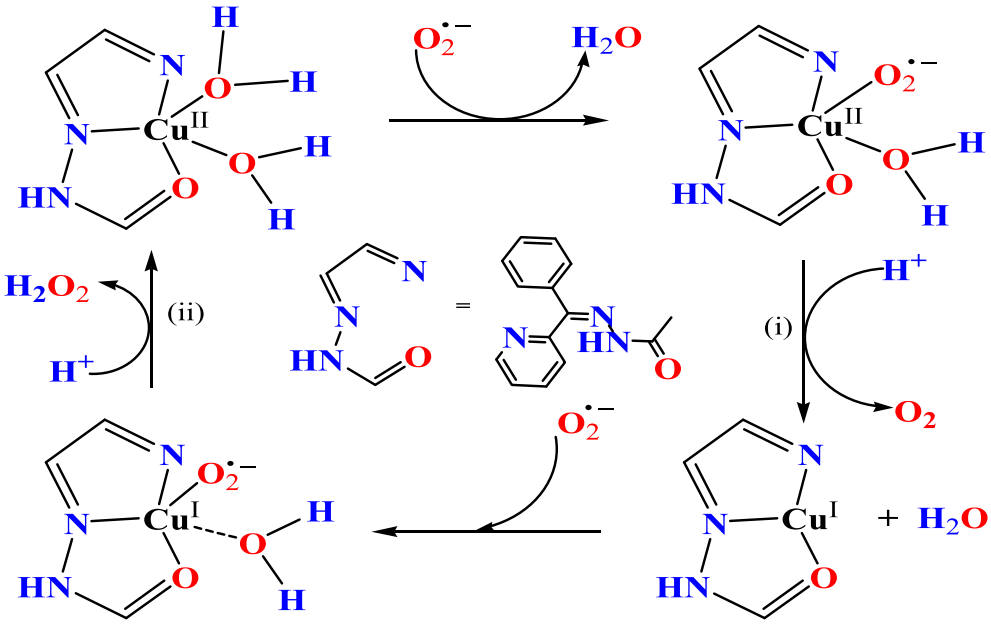

Scheme 3. The proposed catalytic mechanism ($O_2^{-\bullet}$ dismutation reaction by 2).

Declaration of Competing Interest

The authors declare that they have no known competing financial interests or personal relationships that could have appeared to influence the work reported in this paper.

Acknowledgements

RSIC (SAIF) IIT, Bombay for EPR measurements, SAIF, Central Drug Research Institute, Lucknow, are thankfully acknowledged for providing analytical, spectral facilities. Authors acknowledge Jerry P. Jasinski and the NSF-MRI program (Grant No. CHE-1039027) for funds

to purchase the X-ray diffractometer. This work was financially supported by the Spanish Ministerio de Economíay Competitividad (project CTQ2015-63858-P, MINECO/FEDER) and Comunidad de Madrid (project B2017/BMD-3770-CM).

Appendix A. Supplementary data

Supplementary data to this article can be found online at https://doi.org/10.1016/j.ica.2019.119371.

References

[1] (a) K.C. Mondal, A. Sundt, Y.H. Lan, G.E. Kostakis, O. Waldmann, L. Ungur, L.F. Chibotaru, C.E. Anson, A.K. Powell, Angew. Chem. Int. Ed. 51 (2012) 7550–7554;
(b) H.X. Li, W. Zhao, H.Y. Li, Z.L. Xu, W.X. Wang, J.P. Lang, Chem. Commun. 49 (2013) 4259–4261;
(c) L.Q. Mo, J.H. Jia, L.J. Sun, Q.M. Wang, Chem. Commun. 48 (2012) 8691–8693.

[2] (a) J.M. Lehn, Angew Chem. Int. Ed. Engl. 29 (1990) 1304–1319;
(b) M. Emami, N. Noshiranzadeh, R. Bikas, A. Gutierrez, A. Kozakiewicz, Polyhedron 122 (2017) 137–146;
(c) E. Kavlakoglu, A. Elmali, Y. Elerman, I. Svoboda, Polyhedron 21 (2002) 1539–1545.

[3] (a) M.M. Chowdhry, D.M.P. Mingos, A.J.P. White, D.J. Williams, Chem. Commun. (1996) 899–900;
(b) M. Tadokoro, H. Kanno, T. Kitajima, H. Shimada-Umemoto, N. Nakanishi, K. Isobe, K. Nakasuji, Proc. Natl. Acad. Sci. USA 99 (2002) 4950–4955;
(c) M. Tadokoro, T. Shiomi, K. Isobe, K. Nakasuji, Inorg. Chem. 40 (2001) 5476–5478;
(d) L. Ohrstrom, K. Larsson, S. Borg, S.T. Norberg, Chem. Eur. J. 7 (2001) 4805–4810.

[4] (a) X.-L. Zhao, W.-Y. Sun, Cryst. Eng. Comm. 16 (2014) 3247–3258;
(b) P. Lightfoot, A. Snedden, J. Chem. Soc., Dalton Trans. (1999) 3549–4355;
(c) X.-H. Chang, J.-H. Qin, M.-L. Han, L.-F. Ma, L.-Y. Wang, Cryst Eng Comm 16 (2014) 870–882;
(d) Z. Chen, S.C. Xiang, T. Liao, Y. Yang, Y.-S. Chen, Y. Zhou, D. Zhao, B. Chen, Cryst. Growth Des. 10 (2010) 2746–2751;
(e) M.-L. Han, Y.-P. Duan, D.-S. Li, G.-W. Xu, Y.-P. Wu, J. Zhao, Dalton Trans. 43 (2014) 17519–17527;
(f) H. Wang, W. Meng, J. Wu, J. Ding, H.W. Hou, Y. Fan, Coord. Chem. Rev. 307 (2016) 130–146.

[5] (a) C. Adhikary, S. Koner, Coord. Chem. Rev. 254 (2010) 2933–2958;
(b) S. Saha, D. Biswas, P.P. Chakrabarty, A.D. Jana, A.K. Boudalis, S.K. Seth, T. Kar, Polyhedron 29 (2010) 3342–3348;
(c) A.Y. Robin, K.M. Fromm, Coord. Chem. Rev. 250 (2006) 2127–2157;
(d) P.P. Chakrabarty, S. Giri, D. Schollmeyer, H. Sakiyama, M. Mikuriya, A. Sarkar, S. Saha, Polyhedron 89 (2015) 49–54.

[6] (a) A. Datta, N.T. Chuang, M.H. Sie, J.H. Huang, H.M. Lee, Acta crystalogr, E 66 m (2010) 359;
(b) A. Datta, K. Das, Y.M. Jhou, J.H. Huang, H.M. Lee, Acta crystalogr, E 66 m (2010) 1271;
(c) P. Singh, D.P. Singh, V.P. Singh, Polyhedron 81 (2014) 56–65;
(d) R.N. Patel, Y. Singh, Y.P. Singh, R.J. Butcher, A. Kamal, I.P. Tripathi, Polyhedron 117 (2016) 20–34.

[7] (a) E. Ainscough, A. Brodie, J. Ranford, M. Waters, Inorg. Chim. Acta 236 (1995) 83–88;
(b) E. Ainscough, A. Brodie, J. Ranford, M. Waters, Inorg. Chim. Acta 267 (1998) 27–38;
(c) S.K. Akgzel, S. Rollas, I.K. Akgzel, M. Kiraz, Eur. J. Med. Chem. 34 (1999) 1093–1100.

[8] D.X. West, A.E. Liberta, S.B. Padhye, R.C. Chikate, P.B. Sonawane, A.S. Kumbhar, R.G. Yerande, Coord. Chem. Rev. 123 (1993) 49–71.

[9] (a) L.-M. Wu, H.-B. Teng, X.-B. Ke, W.-J. Xu, J.-T. Su, S.-C. Liang, X.-M. Hu, Chem. Biodiversity 4 (2007) 2198–2209;
(b) S. Gupta, S. Pal, A.K. Barik, A. Hazra, S. Roy, T.N. Mandal, S.M. Peng, G.H. Lee, M.S.E. Fallah, J. Tercero, S.K. Kar, Polyhedron 27 (2008) 2519–2528;
(c) N.M.H. Salem, L.E. Sayed, M.F. Iskander, Polyhedron 27 (2008) 3215–3226;
(d) G.C. Xu, L. Zhang, L. Liu, G.F. Liu, D.Z. Jia, Polyhedron 27 (2008) 12–24;
(e) P. Talukder, A. Datta, S. Mitra, G. Rosair, M.S.E. Fallah, J. Ribas, DaltonTrans. (2004) 4161–4167.

[10] S.K. Dey, N. Mondal, M.S.E. Fallah, R. Vicente, A. Escuer, X. Solans, M.F. Bardia, T. Matsushita, V. Gramlich, S. Mitra, Inorg. Chem. 43 (2004) 2427–2434.

[11] (a) C. Santini, M. Pellei, V. Gandin, M. Porchia, F. Tisatoand, C. Marzano, Chem. Rev. 114 (2014) 815–862;
(b) C. Marzano, Anticancer Agents Med. Chem. 9 (2009) 185–211;
(c) S. Banerjee, A.R. Chakravarty, Acc. Chem. Res. 48 (2015) 2075–2083;
(d) C.H. Ng, S.M. Kong, Y.L. Tiong, M.J. Maah, N. Sukram, M. Ahmed, A.S.B. Khoo, Metallomics 6 (2014) 892–906;
(e) D. Mahendiran, R.S. Kumar, V. Viswanathan, D. Velmurugan, A.K. Rahiman, Dalton Trans. 45 (2016) 7794–7814.

[12] P.J. Hart, M.M. Balbirnie, N.L. Ogihara, A.M. Nersissian, M.S. Weiss, J.S. Valentine, D. Eisenberg, Biochem. 38 (1999) 2167–2178.

[13] (a) H. Furukawa, K.E. Cordova, M.O. Keeffe, O.M. Yaghi, Science 341 (974) (2013) 1230444–1230512;
(b) J.A. Mason, M. Veenstra, J.R. Long, Chem. Sci. 5 (2014) 32–51;
(c) X. Zhu, Q. Chen, Z. Yang, B.-L. Li, H.-Y. Li, Cryst Eng. Comm. 15 (2013) 471–481;
(d) L. Hou, Y.-Y. Lin, X.-M. Chen, Inorg. Chem. 47 (2008) 1346–1351;
(e) W.G. Lu, C.Y. Su, T.B. Lu, L. Jiang, J.M. Chen, J. Am. Chem. Soc. 128 (2006) 34–35;
(f) D.-S. Li, J. Zhao, Y.-P. Wu, B. Liu, L. Bai, Z. Kun, M. Du, Inorg. Chem. 51 (2013) 8091–8098;
(g) S.K. Ghosh, R. Joan, P.K. Bharadwaj, Cryst. Growth Des. 5 (2005) 623–629;
(h) X. Zhou, H. Li, H. Xiao, L. Li, Q. Zhao, T. Yang, J. Zuo, W. Huang, Dalton Trans. 42 (2013) 5718–5723;
(i) Y. Zhao, D.-S. Deng, L.-F. Ma, B.-M. Ji, L.-Y. Wang, Chem. Commun. 49 (2013) 10299–10301;
(j) K. Sumida, D.L. Rogow, J.A. Mason, T.M. Mcdonald, E.D. Bloch, Z.R. Herm, T.-H. Bae, J.R. Long, Chem. Rev. 112 (2012) 724–781.

[14] (a) S. Zhou, Y.-G. Chen, B. Liu, X.-M. Li, D.-X. Wang, Eur. J. Inorg. Chem. (2013) 6097;
(b) Y.-L. Wei, X.-Y. Li, T.-T. Kang, S.-N. Wang, S.-Q. Zang, Cryst. Eng. Comm. 16 (2014) 223;
(c) F.-Y. Yi, S. Dang, W. Yang, Z.-M. Sun, Cryst. Eng. Comm 15 (2013) 8320–8323;
(d) J. Fan, C. Slebodnick, R. Angel, B.E. Hanson, Inorg. Chem. 44 (2005) 552–558;
(e) E.-Q. Gao, Y.-X. Xu, C.-H. Yan, Cryst. Eng. Comm. 6 (2004) 298–302;
(f) L.-L. Wen, Y.-Z. Li, Z.-D. Lu, J.-G. Lin, C.-Y. Duan, Q.-J. Meng, Cryst. Growth Des. 6 (2006) 530–537;
(g) P.C.M. Ducan, D.M.L. Goodgame, S. Menzer, D.J. Williams, Chem. Commun. (1996) 2127–2128;
(h) X. Li, R. Cao, W. Bi, Y. Wang, Y. Wang, X. Li, Z. Guo, Cryst. Growth Des. 5 (2005) 1651–1656.

[15] D.D. Perrin, W.L.F. Armarigo, D.R. Perrin, Purification of laboratory Chemicals, 2nd ed., Pergamon, Oxford, England, 1980.

[16] G.M. Sheldrick, SHELXS-97, Program for the Solution for Crystal Structures, University of Gottingen, Gottingen, Germany (1997), Acta Crystallogr. Sect. A 64 (2008) 112–122.

[17] G.M. Sheldrick, SHELXL-97, University of Gottingen, Gottingen, Germany, Program for the Refinement of Crystal Structures, 1997.

[18] M.J. Frisch, G.W. Trucks, H.B. Schlegel, G.E. Scuseria, M.A. Robb, J.R. Cheeseman, G. Scalmani, V. Barone, B. Mennucci, G.A. Petersson, H. Nakatsuji, M. Caricato, X. Li, H.P. Hratchian, A.F. Izmaylov, J. Bloino, G. Zheng, J.L. Sonnenberg, M. Hada, M. Ehara, K. Toyota, R. Fukuda, J. Hasegawa, M. Ishida, T. Nakajima, Y. Honda, O. Kitao, H. Nakai, T. Vreven, J.A. Montgomery Jr., J.E. Peralta, F. Ogliaro, M. Bearpark, J.J. Heyd, E. Brothers, K.N. Kudin, V.N. Staroverov, T. Keith, R. Kobayashi, J. Normand, K. Raghavachari, A. Rendell, J.C. Burant, S.S. Iyengar, J. Tomasi, M. Cossi, N. Rega, J.M. Millam, M. Klene, J.E. Knox, J.B. Cross, V. Bakken, C. Adamo, J. Jaramillo, R. Gomperts, R.E. Stratmann, O. Yazyev, A.J. Austin, R. Cammi, C. Pomelli, J.W. Ochterski, R.L. Martin, K. Morokuma, V.G. Zakrzewski, G.A. Voth, P. Salvador, J.J. Dannenberg, S. Dapprich, A.D. Daniels, O. Farkas, J.B. Foresman, J.V. Ortiz, J. Cioslowski, D.J. Fox, Gaussian 09, Revision D.01, Gaussian, Inc., Wallingford, CT, 2013.

[19] Gauss View 5.0.9 (Gaussion Inc., Wallingford, CT, USA) (2009).

[20] A.E. Reed, R.B. Weinstock, F. Weinhold, J. Phys. Chem. 83 (1985) 735–746.

[21] (a) R. Bauernschmitt, R. Ahlrichs, Chem. Phys. Lett. 256 (1996) 454–464;
(b) R.E. Stratmann, G.E. Scuseria, M.J. Frisch, J. Chem. Phys. 109 (1998) 8218–8224;
(c) M.E. Casida, C. Jamorski, K.C. Casida, D.R. Salahub, J. Chem. Phys. 108 (1998) 4439–4449.

[22] (a) V. Barone, M. Cossi, J. Phys. Chem. 102 (1998) 1995–2001;
(b) M. Cossi, V. Barone, J. Chem. Phys. 115 (2001) 4708–4717.

[23] (a) A.M. Whyte, B. Roach, D.K. Henderson, P.A. Tasker, M.M. Matsushita, K. Awaga, F.J. White, P. Richardson, N. Robertson, Inorg. Chem. 50 (24) (2011) 2867–12876;
(b) Y. Singh, R.N. Patel, Y.P. Singh, A.K. Patel, N. Patel, R. Singh, R.J. Butcher, J.P. Jasinski, E. Colacio, M.A. Palacios, Dalton Trans. 46 (2017) (1874) 11860–11861.

[24] (a) R.N. Patel, S. Kumar, K.B. Pandeya, J. Inorg. Biochem. 89 (2002) 61–68;
(b) R.N. Patel, N. Singh, K.K. Shukla, V.L.N. Gundla, U.K. Chauhan, J. Inorg. Biochem. 992 (2005) 651–663.

[25] (a) T.E. Khalil, L. Labib, M.F. Iskander, Polyhedron 13 (1994) 2569–2578;
(b) R.N. Patel, Y. Singh, Y.P. Singh, R.J. Butcher, J. Coord. Chem. 69 (2016) 2377–2390.

[26] M.A. Ali, A.H. Mirza, R.J. Butcher, M.T.H. Tarafder, M.A. Ali, Inorg. Chim. Acta 320 (2001) 1–6.

[27] D.P. Singh, D.S. Raghuvanshi, K.N. Singh, V.P. Singh, J. Mol. Catal. A: Chem. 379 (2013) 21–29.

[28] (a) A.W. Addison, T.N. Rao, J. Reedjik, J. van Rijn, C.G. Verschoor, J. Chem. Soc., Dalton Trans. (1984) 1349–1356;
(b) G. Murphy, P. Nagle, B. Murphy, B. Hathway, Dalton Trans. (1997) 2645–2652.

[29] (a) G. Murphy, C. Murphy, B. Murphy, B. Hathway, Dalton Trans. (1997) 2653–2660;
(b) P. Nagle, E.O. Sullivan, B. Hathway, Dalton Trans. (1990) 3399–3406;
(c) P.T. Selvi, M. Murali, M. Palaniandavar, M. Kockerling, G. Henkel, Inorg. Chim. Acta, B 340 (2002) 139–146.

[30] (a) S.V. Kryatov, B.S. Mohanraj, V.V. Tarasov, O.P. Kryatova, E.V.R. Akimova, Inorg. Chem. 41 (2002) 923–930;
(b) B.F. Hoskins, F.D. Whiilans, J. Chem. Soc. Dalton Trans. (1975) 657–661.

[31] D.N. Sredojević, Z.D. Tomić, S.D. Zaric, Crystal growth Des. 10 (2010) 3901–3908.
[32] (a) T. Korenaga, H. Tanaka, T. Ema, T. Sakai, J. Fluorine Chem. 122 (2003) 201–205;
(b) M. Egli, S. Sarkhel, Acc. Chem. Res. 40 (2007) 197–205.
[33] J. Cao, J.C. Liu, W.T. Deng, N.Z. Jin, Cryst. Eng. Comm. 15 (2013) 6359–6367.
[34] M. Murphy, B. Hathway, Coord. Chem. Rev. 343 (2003) 237–262.
[35] J.F. Malone, C.M. Murray, M.H. Charlton, R. Docherty, A.J. Lavery, J. Chem. Soc. Faraday Trans. 93 (1997) 3429–3436.
[36] (a) L.R. Hanton, C.A. Hunter, D.H. Purvis, J. Chem. Soc. Chem. Commun. (1992) 1134–1136;
(b) R. Gould, A.M. Gray, P. Taylor, M.D. Walkinshaw, J. Am. Chem. Soc. 107 (1985) 5921–5927.
[37] (a) A.R. Jorge, M. Navarro, R. Angustias, M.J. Salas, Q. Migue, R.T.T. Edward, Inorg. Chem. 36 (1997) 4988–4991;
(b) A.W. Christopher, P.A.Y. Glenn, N.P. Raju, J.E. Greedan, J.C. Robert, Inorg. Chem. 38 (1999) 2548–2549;
(c) J. Miguel, V. Micbel, C.D. Munn, J.A. Real, Inorg. Chem. 32 (1993) 795–802.
[38] P.K. Bhaumik, K. Harms, S. Chattopadhyay, Polyhedron 67 (2014) 181–190.
[39] (a) L.S. Coni, F. Mani, A. Bencini, In comprehensive Coordination Chemistry, G. Wilkinson, R.D. Gillard, J.A. Mcleverty, Eds, Pergamon Press, New York, 5 (1987) 86.
(b) R.N. Patel, N. Singh, K.K. Shukla, U.K. Chauhan, S. Chakraborty, J.N. Gutiérrez, A. Castineiras, J. Inorg. Biochem. 98 (2004) 231–237
[40] R. Morassi, I. Bertini, L. Sacconi, Coord. Chem. Rev. 11 (1973) 343–402.
[41] A.B.P. Lever, Inorganic electronic Spectroscopy, Elsevier, Amsterdam, 1986.
[42] S.V. Kryatov, B.S. Mohanraj, V.V. Tarasov, O.P. Kryatova, E.V.R. Akimova, Inorg. Chem. 41 (2002) 923–930.
[43] (a) E.A. Ambundo, M.V. Deydier, A.J. Grall, N.A. Vega, L.T. Dressel, T.H. Cooper, M.J. Heeg, L.A. Ochrymowycz, D.B. Rorabacher, Inorg. Chem. 38 (1999) 4233–4242;
(b) E.V.R. Akimova, Y.A. Nazarenko, S.S. Silchenko, Inorg. Chem. 38 (1999) 2974–2980.
[44] C.P. Zhang, H. Wang, A. Klein, C. Biewer, K. Stirnat, Y. Yamaguchi, L. Xu, V.G. Benitez, A.D. Vicic, J. Am. Chem. Soc. 135 (2013) 8141–8144.
[45] D. Shoba, S. Periandy, M. Karabacak, S. Ramalingam, Spectrochim. Acta A 83 (2011) 540–552.
[46] K. Fukui, Science 218 (1982) 747–754.
[47] H.J. Jiao, Y.W. Li, B. Delmon, J.F. Halet, J. Am. Chem. Soc. 123 (2001) 7334–7339.
[48] (a) Q.L. Wang, D.Z. Chen, X.W. Liu, L.F. Zhang, Comput, Theor. Chem. 966 (2011) 357–363;
(b) Z. Ru, X.H. Liu, Y.X. Yin, J.J. Yue, S. Yun, M. Yan, X.L. Liu, Chinese, J. Org. Chem. 23 (2003) 1001–1003.
[49] (a) S.K. Silverman, D.A. Dougherty, J. Phys. Chem. 97 (1993) 13273–13283.
[50] (a) J.G. Haasnoot, W.L. Driessen, J. Reedijk, J. Inorg. Chem. 23 (1984) 2803–2807;
(b) R. Vicente, A. Escuer, E. Peñalba, X. Solans, M.F. Bardía, Inorg. Chim. Acta 255 (1997) 7–12;
(c) J.A.R. Navarro, M.A. Romero, J.M. Salas, M. Quirós, E.R.T. Tiekink, Inorg. Chem. 36 (1997) 4988–4991;
(d) S. Hazra, A. Karmakar, M.F.C.G. da Silva, L. Dlháň, R. Bočac, A.J.L. Pombeiro, New J. Chem. 39 (2015) 3424–3434;
(e) S. Khan, S. Sproules, L.S. Natrajan, K. Harms, S. Chattopadhyay, New J. Chem. 42 (2018) 1634–1641.
[51] (a) S. Banerjee, M.G.B. Drew, C.-Z. Lu, J. Tercero, C. Diaz, A. Ghosh, Eur. J. Inorg. Chem. (2005) 2376–2383;
(b) S. Khan, S. Sproules, L.S. Natrajan, K. Harms, S. Chattopadhyay, New J. Chem. 41 (2017) 8885–8898.
[52] B.J. Hathaway, D.E. Billing, Coord. Chem. Rev. 5 (1970) 143–207.
[53] J.L. Pierre, P. Chautemps, S. Refaif, C. Beguin, A. Marzouki, G. Serratrice, E.S. Aman, P. Rey, J. Am. Chem. Soc. 117 (1995) 1965–1973.
[54] Y.P. Singh, R.N. Patel, Y. Singh, D.C. Lazarteb, R.J. Butcher, Dalton Trans. 46 (2017) 2803–2820.
[55] (a) M.A. Ali, A.H. Mirza, R.J. Fereday, R.J. Butcher, J.M. Fuller, S.C. Drew, L.R. Gahan, G.R. Hanson, B. Moubaraki, K.S. Murray, Inorg. Chim. Acta 358 (2005) 3937–3948;
(b) M.H.S.A. Hamid, M.A. Ali, A.H. Mirza, P.V. Bernhardt, B. Moubaraki, K.S. Murray, Inorg. Chim. Acta 362 (2009) 3648–3656;
(c) K. Das, A. Datta, C. Sinha, J.-H. Huang, E. Garribba, C.-S. Hsiao, C.-L. Hsu, Chemistry open 1 (2012) 80–89.
[56] E. Garribba, G. Micera, J. Chem. Educ. 83 (2006) 1229–1232.
[57] T. Mosmann, J. Immunol. Methods 65 (1983) 55–63.
[58] (a) R.N. Jadeja, K.M. Vyas, K.K. Upadhyay, R.V. Devkar, RSC Adv. 7 (2017) 17107–17116;
(b) K.M. Vyas, R.N. Jadeja, D. Patel, R.V. Devkar, V.K. Gupta, Polyhedron 65 (2013) 262–274;
(c) S.K. Patel, R.N. Patel, Y. Singh, Y.P. Singh, D. Kumhar, R.N. Jadeja, H. Roy, A.K. Patel, N. Patel, N. Patel, A. Banerjee, D.C. Lazarte, A. Gutierrez, Polyhedron 161 (2019) 198–212.
[59] A. Hussain, M.F. Alajmi, M.T. Rehman, S. Amir, F.M. Husain, A. Alsalme, M.A. Siddiqui, A.A.A. Khedhairy, R. Khan, Sci. Rep. 9 (2019) 5237.
[60] M. Scarpellini, A. Neves, R. Horner, A.J. Bortoluzzi, B. Szpoganicz, C. Zucco, R.A.N. Silva, V. Drago, A.S. Mangrich, W.A. Ortiz, A.C.W. Passos, M.C.B. Oliveira, H. Terenzi, Inorg. Chem. 42 (2003) 8353–8365.
[61] (a) S. Ramakrishnan, V. Rajendiran, M. Palaniandavar, V.S. Periasamy, B.S. Srinag, H. Krishnamurthy, M.A. Akbarsha, Inorg. Chem. 48 (2009) 1309–1322;
(b) V. Rajendiran, R. Karthik, M. Palaniandavar, H.S. Evans, V.S. Periasamay, M.A. Akbarsha, B.S. Srinag, H. Krishnamurthy, Inorg. Chem. 46 (2007) 8208–8822.
[62] T.B. Demirci, C. Gulsah, A. Erdem, S.E. Kuruca, N.O. Zdemir, K.A. Dar, B. Varolf, B.U. Sevena, New J. Chem. 39 (2015) 5643–5653.
[63] (a) D.F. Li, S. Li, D.X. Yang, J.H. Yu, J. Huang, Y.Z. Li, W.X. Tang, Inorg. Chem. 42 (2003) 6071–6080;
(b) H. Ohtsu, Y. Shimazaki, A. Odani, O. Yamauchi, W. Mori, S. Itoh, S. Fukuzumi, J. Am. Chem. Soc. 122 (2000) 5733–5741;
(c) Y. Li, Z.Y. Yang, J.C. Wu, Eur. J. Med. Chem. 45 (2010) 5692–5701;
(d) H. Fu, Y.H. Zhou, W.L. Chen, Z.G. Deqing, M.L. Ji, L.N. Tong, Z.W. Mao, J. Am. Chem. Soc. 128 (2006) 4924–4925;
(e) Y.H. Zhou, H. Fu, W.X. Zhao, W.L. Chen, C.Y. Su, H.Z. Sun, L.N. Ji, Z.W. Mao, Inorg. Chem. 46 (2007) 734–739;
(f) X. Meng, M. Wang, N. Jiang, D. Zhang, L. Wang, C. Liu, J. Agric. Food Chem. 60 (2012) 11211–11221;
(g) R.N. Patel, Y. Singh, Y.P. Singh, A.K. Patel, N. Patel, R. Singh, R.J. Butcher, J.P. Jasinski, E. Colacio, M.A. Palacios, New J. Chem. 42 (2018) 3112–3136;
(h) Y.C. Fang, H.C. Lin, I.J. Hsu, T.S. Lin, C.-Y. Mou, J. Phys. Chem. 115 (2011) 20639–20652;
(i) R.N. Patel, S. Rawat, M. Choudhary, V.P. Sondhiya, D.K. Patel, K.K. Shukla, D.K. Patel, Y. Singh, R. Pandey, Inorg. Chim. Acta 392 (2012) 283–291;
(j) R.N. Patel, D.K. Patel, K.K. Shukla, Y. Singh, J. Coord. Chem. 66 (2013) 4131–4143;
(k) R.N. Patel, D.K. Patel, V.P. Sondhiya, K.K. Shukla, Y. Singh, A. Kumar, Inorg. Chim. Acta 405 (2013) 209–217;
(l) Y. Singh, R.N. Patel, S.K. Patel, A.K. Patel, N. Patel, R. Singh, R.J. Butcher, J.P. Jasinski, A. Gutierrez, Polyhedron 171 (2017) 155–171.